

DEVELOPING REALISTIC MODELS OF THE ATRIUM AND THE P-WAVE ECG

A THESIS SUBMITTED TO THE UNIVERSITY OF MANCHESTER
FOR THE DEGREE OF DOCTOR OF PHILOSOPHY
IN THE FACULTY OF ENGINEERING AND PHYSICAL SCIENCES

2009

By
Jonathan D. Stott
School of Physics and Astronomy

Contents

Abstract	9
Declaration	10
Copyright	11
Acknowledgements	12
The Author	13
1 Introduction	14
1.1 The Heart	15
1.1.1 Location of the Heart	15
1.1.2 Gross Structure of the Heart	15
1.1.3 The Atria	16
1.1.4 Cardiac Myocytes	19
1.2 Mathematical Models of the Heart	23
1.2.1 Categorising Myocyte Models	23
1.2.2 A Brief History of Cardiac Myocyte Modeling	24
1.2.3 Mathematical Models of Myocytes	24
1.2.4 Selected Myocyte Models	28
1.2.5 Models of Action Potential Propagation	31
1.2.6 Numerical Techniques	32
1.3 The Electrocardiograph	35
1.3.1 Lead Theory	36
1.3.2 The Twelve Lead Electrocardiogram	37
1.3.3 The ECG Waves	40
1.3.4 The Vectorcardiogram	42

1.3.5	Body Surface Potential Mapping Arrays	43
1.4	The Forward Problem	44
1.4.1	Uses of the Forward Problem	44
1.4.2	A Brief History of the Forward Problem	45
1.4.3	Numerical Approaches	46
1.5	Cardiac Simulation Toolkit	47
1.5.1	Advantages of Cardiac Simulation Toolkits	47
1.5.2	Disadvantages of Cardiac Simulation Toolkits	48
1.5.3	Available Toolkits	49
2	Constructing a Cardiac Simulation Toolkit	51
2.1	Simulation Environment	51
2.1.1	Implementation	51
2.1.2	Parallelization	53
2.1.3	Performance Optimisation	54
2.2	Experimental Protocols	60
2.2.1	Action Potential	60
2.2.2	Action Potential Duration Restitution	61
2.2.3	Effective Refractory Period Restitution	61
2.2.4	Vulnerable Window	62
2.2.5	Threshold of Excitation	63
2.2.6	Conduction Velocity Restitution	64
2.2.7	Spiral Wave Dynamics	65
2.2.8	Spatial Vulnerability of Cardiac Tissue	65
2.3	Results From Simulation Studies	66
2.3.1	Anion Currents In The Human Atrium	66
2.3.2	Atrial Fibrillation Induced Remodelling And Heterogeneity	75
2.4	Discussion and Conclusions	82
3	Modelling the Whole Atrium	84
3.1	Anatomical Atrial Geometry	84
3.2	Simulation Methods	86
3.2.1	Atrial Model	86
3.2.2	Monodomain Equation	87
3.2.3	Tissue Anisotropy	88
3.2.4	Computational Implementation	89

3.3	Validation of the Model	91
3.3.1	Activation Maps	91
3.3.2	Comparisons with Experimental Studies	94
3.3.3	Comparisons with Existing Models	94
3.4	Mutation in KCNQ1: A Simulation Study	95
3.5	Modelling the Whole Atrium: Conclusion	108
4	The Body Surface Potential	109
4.1	The Forward Problem	109
4.2	The Atrial Dipole	115
4.3	Torso Geometry	116
4.4	Computational Implementation	117
4.5	Simulating Sinus Rhythm	119
4.5.1	Simulated Body Surface Potential Maps	119
4.5.2	Simulated Electrocardiograms	126
4.5.3	Comparisons with Clinical Studies and Information	131
4.5.4	Comparisons with other Modelling Studies	132
4.6	Limitations of the Model	135
4.7	Conclusions	136
5	Applications Of The Forward Problem	137
5.1	Focal Atrial Tachycardia	138
5.1.1	Model of Focal Atrial Tachycardia	138
5.1.2	Results	138
5.1.3	Discussion and Conclusion of Focal Atrial Tachycardia Study	143
5.2	Inverted P-Waves at Night	145
5.2.1	Methods	146
5.2.2	Results	147
5.2.3	Discussion and Conclusions of Inverted P-wave Study . . .	155
5.3	Discussion and Conclusion	157
6	Discussion and Conclusions	159
6.1	Cardiac Simulation Toolkit	159
6.2	Whole Atrial Model	160
6.3	Body Surface Potential Model	162
6.4	Applications of the Body Surface Potential Model	163

6.5 Future Work	164
Bibliography	166

Word Count: 44224

List of Tables

1.1	Inverse Dower Factors after Edenbrandt and Pahlm	44
2.1	Parameter sets for the anion carrying current	67
2.2	Calculated parameters for anion and control cells	69
2.3	Parameter modifications for AFER	76
3.1	Tissue Heterogeneity Parameters	87
4.1	Conductances of torso compartments	118
4.2	Maximum and minimum potentials observed in ECG leads	130
5.1	Pacing Sites Around The Atria	139
5.2	Lead classification from pacing sites through the atria	140
5.3	Classification of focal point tachycardia	143
5.4	Inverse Dower Factors after Guillem et al.	147
5.5	Lead classification from pacing sites along the CT	151

List of Figures

1.1	Time-Dependent Ion Channel	21
1.2	Ion Pump	21
1.3	Schematic AP Profile	22
1.4	Electrical Circuit Model Of The Cell	25
1.5	5-node Stencil for the Finite Difference Method	34
1.6	Diagram of the Reciprocity Principle and the Lead Field	37
1.7	Lead placements for the 12 Lead ECG	38
1.8	Hexaxial Reference System	40
1.9	Schematic ECG	41
1.10	ECG Morphology	42
1.11	Schematic Vector Loops	43
2.1	Illustration of AP properties	60
2.2	Illustration of VW cases	63
2.3	Anion Current AP Profiles and $I_{Ca,L}$ gating parameters	69
2.4	Anion Current APD Restitution	70
2.5	Anion Current ERPr and CVr	71
2.6	Anion Sensitive Threshold Of Excitation and I_{Na} activation	72
2.7	Anion Sensitive Tissue Sheets and Spiral Lifespans	73
2.8	AFER AP Plots And APD differences	78
2.9	AFER APDr and ERPr curves	78
2.10	AFER CVr curves and VWs	79
2.11	AFER 2D re-entry plots	80
3.1	Atrial Geometry	85
3.2	Atrial Fibre Structure	86
3.3	Relationship of θ , ϕ and \mathbf{f}	90
3.4	Snapshots of Electrical Activation under Sinus Rhythm (frontal) .	92

3.5	Snapshots of Electrical Activation under Sinus Rhythm (from ventricular openings)	93
3.6	Activation Times Under Sinus Rhythm	93
3.7	KCNQ1 mutation in IKs, experimental data	98
3.8	Initiating a Scroll Wave	100
3.9	AP and current profiles with S140G mutation	101
3.10	Restitution properties with S140G mutation	102
3.11	2D Re-entry under S140G conditions	103
3.12	Frequency of extracted APs from 2D sheets with S140G mutation	104
3.13	Spatial Vulnerability Window with S140G mutation	105
3.14	Snapshots of membrane potential over the whole atrium with S140G mutation	106
4.1	Diagram of the vectors and surfaces involved in the BEM	110
4.2	Torso showing embedded atrium and lead locations	117
4.3	Body Surface Potential snapshots, homogeneous torso	121
4.4	Body Surface Potential snapshots, with lungs	122
4.5	Body Surface Potential snapshots, with blood masses	124
4.6	Body Surface Potential snapshots, with all inhomogeneities	125
4.7	12 lead P-wave ECG during sinus rhythm with homogeneous torso	126
4.8	12 lead ECG during sinus rhythm, lungs present.	127
4.9	12 lead ECG during sinus rhythm, bloodmasses present.	128
4.10	12 lead ECG during sinus rhythm, all internal inhomogeneities present.	129
4.11	Comparative BSPM from the fully inhomogeneous model and Mirvis	133
5.1	Pacing Sites Around The Atria	139
5.2	P-wave ECGs For Ectopic Focal Sites	141
5.3	Pacing Sites Along The CT	146
5.4	Activation sequences from pacing sites along the CT	148
5.5	12 Lead ECG traces from pacing sites along the CT	150
5.6	Frontal plane vector loops from pacing sites along the CT	153
5.7	Transverse plane vector loops from pacing sites along the CT	154

Abstract

The University of Manchester

Jonathan David Stott

Doctor of Philosophy

Developing Realistic Models of the Human Atrium and the P-Wave ECG

23rd September 2009

Cardiac disease, including atrial fibrillation (AF), is one of the biggest causes of morbidity and mortality in the UK, accounting for one third of all deaths. Cardiac modelling is now a well established field. Mathematical models offer a valuable way of gaining insight into the dynamic behaviours of the heart, in normal and pathological conditions. Great efforts have been put into modelling the ventricles, whilst the atria have received less focus. This thesis therefore concentrates on developing models of the atria.

In the first part of the thesis, I developed a simulation toolkit for modelling myocyte electrophysiology and excitation waves in 1D & 2D tissues. It includes optimisations such as adaptive stimulus protocols. As examples of application, it is used to investigate effects of a novel anion bearing current on atrial excitation and the effect of AF remodelling on atrial myocyte electrical heterogeneity.

In the second part, a computationally efficient and anatomically based model of the atria is constructed. The 3D model includes heterogeneous, biophysically detailed electrophysiology and conduction anisotropy. The full model activates in 121 ms in sinus rhythm, in close agreement with clinical data. The model is used, with the toolkit, to investigate the function effects of S140G mutation in KCNQ1 which is associated with familial AF.

In the last half of the thesis, the 3D model forms the core of a boundary element model of the P-wave Body Surface Potential (BSP). The BSP model incorporates representations of the lungs and the heart blood masses. Generated ECGs show qualitative agreement with clinical data. Their morphology is as expected for a healthy person, with a lead II duration of 103 ms. The BSP model is used to verify an existing algorithm for focal atrial tachycardia location and in providing explanation for a novel clinical phenomena, inverted P-waves at night.

Models of the human atria and body surface potential are constructed. The models are validated against both experimental and clinical data. These models are suitable to use as the platform for further research.

Declaration

No portion of the work referred to in this thesis has been submitted in support of an application for another degree or qualification of this or any other university or other institute of learning.

Copyright

- i. The author of this thesis (including any appendices and/or schedules to this thesis) owns any copyright in it (the “Copyright”) and s/he has given The University of Manchester the right to use such Copyright for any administrative, promotional, educational and/or teaching purposes.
- ii. Copies of this thesis, either in full or in extracts, may be made only in accordance with the regulations of the John Rylands University Library of Manchester. Details of these regulations may be obtained from the Librarian. This page must form part of any such copies made.
- iii. The ownership of any patents, designs, trade marks and any and all other intellectual property rights except for the Copyright (the “Intellectual Property Rights”) and any reproductions of copyright works, for example graphs and tables (“Reproductions”), which may be described in this thesis, may not be owned by the author and may be owned by third parties. Such Intellectual Property Rights and Reproductions cannot and must not be made available for use without the prior written permission of the owner(s) of the relevant Intellectual Property Rights and/or Reproductions.
- iv. Further information on the conditions under which disclosure, publication and exploitation of this thesis, the Copyright and any Intellectual Property Rights and/or Reproductions described in it may take place is available from the Head of School of Physics and Astronomy (or the Vice-President).

Acknowledgements

I would like to thank my supervisor, Prof. Henggui Zhang of the Biological Physics group at Manchester, for his support and guidance throughout my thesis. Without his help, this work would not have been completed.

I would also like to thank all of the members of the Biological Physics group, past and present, for their conversations on the thesis and on the topics around it (and everything else). Through them I have learned of papers I might have missed and considered avenues of investigation that otherwise I might not have done. This gratitude is extended to the members of the Cardiovascular Physiology group at Manchester, especially Prof. Mark Boyett who leads the group and who has been a source of valuable discussion on topics all around the field of cardiac electrophysiology.

Another debt of gratitude is owed to Doctors Clifford Garret, Derek Rowlands and Gwilym Morris. Their discussions about the ECG in general and the ones produced in this thesis in specific were helpful as I refined the model.

My parents, David and Judith Stott and my sister, Joanna. I'm not sure how to thank them for all their love and support as I have worked on this thesis.

My friends, both local and remote. For occasional discussions about programming, my work and anything else that was on my mind. They've helped me, probably in more ways than they know.

I would like to thank EPSRC for providing the funding which enabled me to complete my studies.

Finally, I would like to thank all those who saw drafts of this thesis. Without them, the final text would have had more errors. Though, of course, any errors which remain are my own.

The Author

Jonathan Stott graduated with an Master of Physics (2:1) degree from the University Of Manchester in 2005. This thesis represents his first major research project. A smaller research project in the field was completed as part of his Master's course, which was presented at the Physiological Society meeting in Bristol (2005).

Chapter 1

Introduction

Cardiac disease is one of the biggest causes of death in the UK, causing over one third of all deaths. In addition to the deaths, many more people suffer the after effects of a heart attack or live with the difficulties caused by heart failure [1]. These figures are duplicated across much of the developed world.

Mathematical modelling of the heart offers a way of gaining insight into the cardiac processes and the mechanisms of cardiac disease. It is a well established field of research with numerous international journals and conferences discussing the findings. Mathematical models allow physiological effects to be dissected and quantified in ways that can be difficult for *in vivo* and *in vitro* experiments. This can be used to inform both further experiments and clinical diagnosis and treatment.

Mathematical models exist for many different types of cardiac cells and cardiac tissue. Many studies of cardiac tissue focus on the ventricles, with atrial studies less common. This is in part because failure of the ventricles can have a much more serious impact, but in spite of this, the atria represent an interesting target to study. They have a complex electrophysiology and topology.

This study therefore aims to construct a series of models and tools for studying the atria of the heart. This involves modelling the atria and their processes on a wide variety of scales, from the single cell to the whole atrium. To enhance the clinical relevance of the study, a model of the atrium sitting within the human torso will also be constructed. This will allow the P-wave ECG to be calculated, the first view many cardiac physicians will have of a failing atrium. The tools will then be used to study a variety of factors that influence atrial behaviour.

1.1 The Heart

The heart's role is to pump blood around the body, driving the circulation of the blood and everything contained within it. It is one of the most important organs in the body and any malfunction in its behaviour could be fatal in very short order. It begins beating in the early stages of pregnancy and continues until death, hopefully many decades later. It beats at an average rate of around 70 beats per minute (bpm) for the adult male and 75 bpm for the adult female.

The heart is not, as popular belief would have it, the seat of human emotion. The functioning of the heart is modulated by such emotion however, slowing when we are calm and increasing in rate quite dramatically when we are excited or afraid. Despite being influenced by the brain and our emotional states, the heart drives itself, rather than having the pace-making initiated outside the organ.

1.1.1 Location of the Heart

The human heart sits in the centre of the chest, the bulk of it extending into the left-hand side of the chest cavity, inside a fibrous sac called the pericardium. The actual location, orientation and size can vary quite significantly from individual to individual [2].

1.1.2 Gross Structure of the Heart

The heart is mostly muscle. This muscle is anchored to a collagenous 'skeleton', known as the annulus fibrosus located at the atrio-ventricular junction. The muscle is different from the 'smooth' skeletal muscle, in both structure and behaviour [3].

The human heart has four chambers; two atria and two ventricles. The atria receive the blood from the circulatory system and force it into the two ventricles, which then contract and force this blood out and around the lungs and body. These chambers are known as the left and right atria and the left and right ventricles. The left hand side of the heart in humans is much more developed than the right. This is due to their differing roles in circulating the blood.

The right and left atria are smaller than their respective ventricles and have much thinner walls, because they need to develop much less pressure. The right atrium receives the blood from the circulatory system which is de-oxygenated, and

passes it on to the right ventricle. The left atrium receives the highly oxygenated blood from the lungs, and passes it onto the left ventricle. The two atria are separated by a thin muscle wall known as the intra-atrial septum. This prevents the mixing of blood between the two atrial chambers.

The differences between the right and left ventricles are much more pronounced than those between the right and left atria. The right ventricle must merely pump blood around the lungs and developing too high a pressure there could actually damage the delicate structures. By contrast the left ventricle must develop enough pressure to drive blood around the whole body and as such it is much more muscular. The two ventricles are divided by the ventricular septum.

As noted earlier, separating the atria and ventricles is the annulus fibrosus or central fibrous body. This is a dense layer of fibrous tissue. In addition to providing an anchor for the muscle of the heart, it electrically isolates the atria from the ventricles. In the normal heart, the only electrical connection between the atria and the ventricles is at the atrio-ventricular node. This connects the right atrium to the specialist conduction system of the ventricles.

1.1.3 The Atria

Examination of the human atria (or auricles, in older literature) is as old as studies of the heart. However, in recent years there has been a renewed interest in the atria and their structures. This has followed an increasing appreciation that the atria are not merely reservoirs of venous blood, but have an active role to play in the function of the heart [4–8].

Descriptions of the location of features use the ‘altitudinal’ description, where this is possible. Altitudinal descriptions use the coordinates of the body, such that ‘right’ is the body’s right hand side, not the right of the observer. In this description, the atria are located to the right of the ventricles. They can be slightly superior, too. The right atrium is anterior and to the right, the left atrium more posterior and to the left of the body.

The atria have a number of common features. Both have a valve on the base, which is part of the central fibrous body. In the right atrium, this is the tricuspid valve, in the left, the mitral valve. These valves feed into the respective ventricles.

Both atria also have appendages, although the appendages differ in form. The right atrial appendage is large, with a triangular shape and a wide base. It is located anteriorly and superiorly on the right atrium. By contrast, the left atrial

appendage is smaller and more tubular in nature. It is located posteriorly and superiorly compared to the left atrium.

The Right Atrium

The right atrium gathers in blood from the body, after it has cycled around the organs. The right atrium has a simpler topology than the left atrium. At the top is an opening for the superior vena cava, and at the base there are openings for the inferior vena cava and the tricuspid valve.

The right atrium is the location of many of the important sites of the conduction system of the heart. The sinus node, or sino-atrial node (SAN), is located on the right atrial wall, close to the superior vena cava. The SAN is the primary pacemaker for the heart in normal function. It achieves this through specialised cells, known as nodal cells. These cells are what are termed ‘auto-active’ and are capable of spontaneously exciting.

Running down the lateral wall is a muscle ridge, known as the crista terminalis, or terminal crest. The crista terminalis delineates the smooth and rough parts of the right atrial wall. This muscle ridge consists mostly of myocytes—cardiac muscle cells—arranged longitudinally along the main axis of the ridge, and so forms a path of preferential conduction. In addition, these cells have a specialised electrophysiology [9].

At the inferior end of the crista terminalis there is the atrio-ventricular node (AVN). This is another area of specialised nodal cells. These cells are also auto-active, although with a slower natural frequency than the SAN. They therefore only take over in the case of SAN failure. The AVN is the only point of electrical contact between the atrium and ventricles in the normal heart. As well as providing a link between the atria and ventricles this region acts to limit the rate of stimulus which is passed on to the ventricles, protecting them from excessive atrial pacing rates.

Branching from the crista terminalis and spreading around the muscle wall of the right atrium are the pectinate muscles. Like the crista terminalis, these bundles consist mostly of cells lying end to end, forming pathways of preferential conduction. The conformation of the pectinate muscles varies between individuals; some have complex branching and interwoven patterns, whilst others have simpler and relatively parallel bundles.

The Atrial Septum

The atrial septum divides the two atria. Much of the septum is actually an infolding of the right atrium. The true septum is limited to the fossa ovalis and the muscle ring immediately surrounding it. The fossa ovalis is a valve which is important in fetal circulation, but is closed in the normal adult. The fossa ovalis is mostly fibrous in nature. The muscle fibres run in a predominately circular direction around the fossa.

The Left Atrium

The left atrium gathers blood from the lungs. The pulmonary veins tend to give the left atrium a more complex topology than the right. This complex topology can make the pulmonary veins a source of arrhythmic activity.

Unlike the right atrium, the left atrium is not dominated by the appendage. In the left atrium, the appendage is small and largely separate from the main body of the atrium. The endocardial surface of the appendage is covered in many fine muscle ridges. Between these ridges, the walls of the atrium can be paper thin.

Conventionally the left atrium is depicted as having four openings for the pulmonary veins. Recent studies, reviewed in [6], suggest considerably more variation with approximately one third of hearts having merged veins on one or both sides. In some cases, the single vein can actually link all the way to the lungs. The pulmonary veins are surrounded by a sheath of tissue. There is evidence that cells in the sheaths can have different electrophysiology to normal atrial cells [10].

The left atrial wall is relatively smooth. However, it is not uniform in thickness or muscle architecture. It instead has a complex and overlapping muscle structure. This can look like layers, but there are no insulating fibrous sheets between bundles.

Inter-atrial Connections

The atria are linked by muscle bundles. These muscle bundles have cells mainly oriented end to end, which gives preferential conduction along their axis. The most well known of these is the Bachmann's bundle, which is located anteriorly and superiorly between the two atria.

Common thought has it that the Bachmann's bundle is the principle electrical connection between the atria in sinus rhythm. However, recent studies (summarised in [7,8]) have found that in a significant fraction of the population, a secondary pathway which is inferior and/or posterior is used instead. In some subjects, a Bachmann's bundle cannot even be located. There are a lack of studies performed on healthy subjects, however, so it is unclear what occurs in the normal case.

1.1.4 Cardiac Myocytes

Myocytes, or muscle cells, comprise the vast bulk of cardiac tissue. They both conduct electrical signals and contract to provide the force needed to pump the blood around the body. This is accomplished by a complex interplay of ionic currents [3].

Myocyte Structure

A typical human myocyte is from 50 to 150 μm long, and has a radius between 10 and 20 μm . They have a roughly cylindrical shape. The cell is wrapped in an impermeable membrane, called the sarcolemma or plasma membrane. The membrane in many myocytes is invaginated at various points by series of fine transverse tubules (T tubules) that carry action potentials deep into the myocytes.

The cellular membrane contains a large number of specialised structures responsible for allowing a regulated flow of ions into and out of the cell. These structures include passive channels, active pumps and gated channels. They are used to modulate the ionic composition of the intracellular space and play a vital role in modulating the electrical activity of the cell. Because it is impermeable a potential difference can build across the membrane between the inside and outside of a cell. This is the membrane potential.

Within the cells, much of the space is filled with what are called myofibril-like units, long branching fibres about 1 μm in diameter. These fibres are divided up into sarcomeres, approximately 2 μm long in the resting myocyte, which is considered the basic contractile unit. Mitochondria, which provide the ATP needed to provide energy for the contractions, also occupy a significant fraction of the intracellular space. Mitochondria are not actually a part of the body in the strictest sense and have their own DNA – they are symbiotic organisms that entered our

own cells at some unknown time in the past. One other structure within the cells that is important to the electrical and mechanical behaviour of the cells is a second tubule network, known as the sarcoplasmic reticulum (SR) and the sarcotubular network. The SR stores calcium in subsarcolemmal cisternae, which is released during the membrane depolarisation. The cisternae form structures known as dyads (or diads) with the T tubules.

Ion Channels and Pumps

The structures in the cellular membrane which permit ions to cross can be roughly divided into channels and pumps. Most channels and pumps are specific to one specific ion type. Channels passively allow ions to flow with the concentration gradient, whilst pumps actively move ions, regardless of the gradient [11].

Channels and pumps are classified by the ion(s) they transport and how they are controlled. They are also classified on the direction of charge flow. An inward current is one that would have the effect of a positive ion entering the cell and could therefore also be caused by negatively charged ions exiting the cell. Inward currents act to increase the potential in the cell. Conversely, outward currents are those that would have the effect of a positive ion leaving the cell. They are repolarizing currents as they act to decrease the membrane potential.

Inter-cardiac current flows through the gap junctions, which allow for large current flows. These are formed at the centre of membrane structures known as intercalated disks. The intercalated disks are concentrated at the ends of cells, although there are some transverse connections.

Channels rely on an ionic gradient to drive flow through them. Some channels have a constant conductance. These are typically called background currents. Channels with a conductance which depend on the instantaneous membrane potential are known as voltage-gated channels. Other channels can have their conductance modulated by the presence of a hormone or chemical, such as the ATP sensitive potassium channel. Many gated channels are what are known as time-dependent channels. These channels have structures over one or both ends which modulate the total conductance to open (activate) or close (inactivate) the channel. This is illustrated in figure 1.1. The time course of this activation or inactivation is normally modulated by the voltage, but can also be modulated by ion concentration or other mechanisms. Pumps use energy to actively move ions against the gradient. Complex molecules latch onto the ions on one side of the

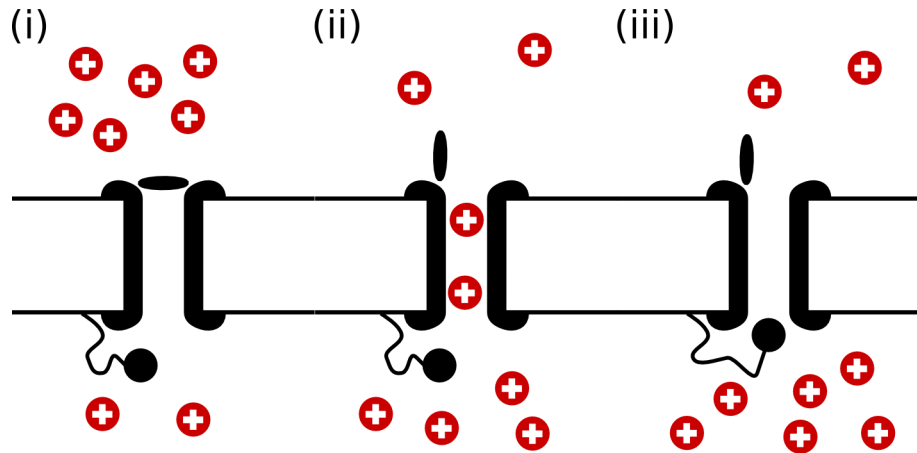


Figure 1.1: A time dependant ion channel, represented by the black structure which bisects the membrane (horizontal lines) for positive ions, shown as red circles. The channel has an activation gate, the black lozenge on the top of the membrane and an inactivation gate, the ball and chain on the underside of the membrane. In panel (i) the gate is not activated and shows a large concentration of ions on the upper side. In panel (ii), the gate activates and ions flow down the channel to the region of lower concentration. In panel (iii), the inactivation gate has moved to close the channel and no more ions flow.

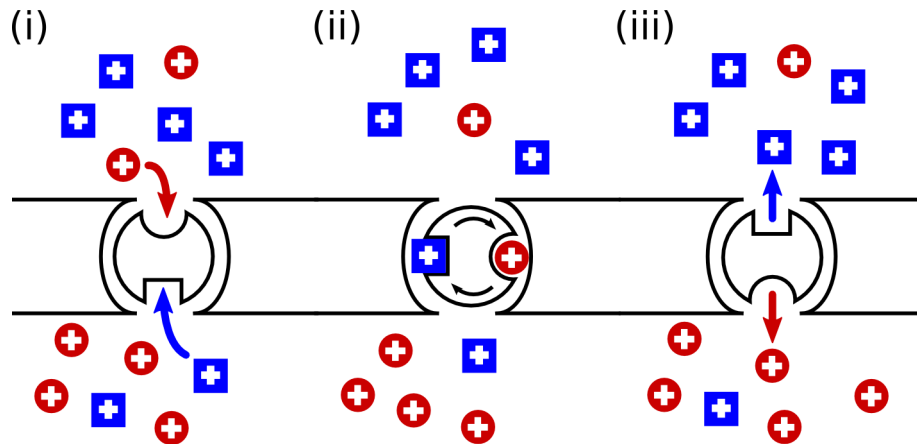


Figure 1.2: An ion pump (or more accurately, an ion exchanger), represented by the black structure which bisects the membrane (horizontal lines) for two species of positive ion, represented by red circles and blue squares. The pump works against the concentration gradient. In panel (i), the two ions bind to their respective sites on the pump. In panel (ii), the pump changes its structure, drawing each ion through the membrane. In panel (iii), the pump releases the binding of the ions, letting them rejoin the free ion populations.

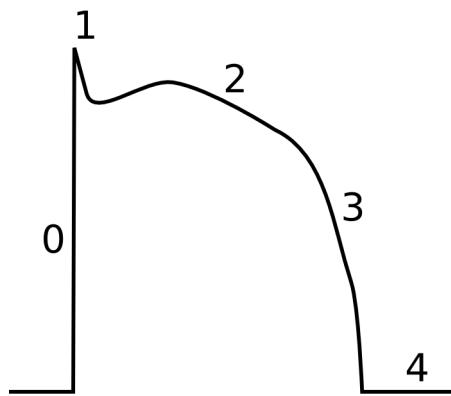


Figure 1.3: A schematic AP profile. Labelled are the five phases of the action potential. Phase 0, the upstroke. Phase 1, the end of the upstroke. Phase 2, the plateau. Phase 3, the repolarization. Phase 4, the resting period.

membrane and move them through to the other side. Many pumps are actually exchangers, which take in ions of one sort on one side whilst transporting another type of ion the other way.

Myocyte Electrical Action Potentials

The evolution of the electrical state of the cell, from polarised to depolarised and back again is termed the action potential (AP). The shape and duration of the action potential is mostly determined by the channels, carriers and pumps across the cellular membrane, though the internal and external concentrations of several ions and molecules can also have a significant effect. There are three principle ion species involved in the development of the action potential; sodium (Na^+), potassium (K^+) and calcium (Ca^{2+}). The third, calcium, is also important for contractile function. Chlorine (Cl^-) is also of importance in some cells.

The action potential has 5 phases (figure 1.3). It begins with depolarization, phase 0. During depolarisation, the current is carried principally by the fast inward sodium current. Phase 0 is also known as the upstroke of the action potential, and its slope is important to the propagation of the action potential through cardiac tissue and also the excitability of the myocyte as in individual cell. Phase 0 is over almost instantaneously in healthy myocytes.

Phase 1 signifies the end of the upstroke, and is caused by the inactivation of the sodium channels. The small notch present in some cellular action potentials

is caused by a transient net outward current, carried principally by potassium.

Phase 2 is the plateau phase. This relatively long phase ($>100\text{ms}$ in some myocytes) is due to the balance of slowly activating inward calcium currents and the outward potassium currents. The inward calcium current is principally carried by the L-type calcium channels and the outward potassium current by a plethora of channels, classified by the speed of activation or the substance which modulates them.

Phase 3 is the repolarization period. The calcium channels have inactivated. The potassium currents are still open, and the net efflux of positive charge repolarizes the cell.

The final phase 4 is the period during which the cell is at the resting potential. In addition, for a short period of phase 4, the cell is in fact impossible to excite above this resting potential due to the inactivations of numerous channels. This is called the refractory period.

Both the shape and the length of the action potential have physiological importance. Many pathological conditions have a significant impact upon both. The action potential duration (APD) is often given as an APD₉₀ or APD₅₀, denoting the duration of the AP at 90% or 50% repolarization, respectively.

1.2 Mathematical Models of the Heart

Cardiac tissue has been modelled mathematically for about fifty years. While initial models were simple, there are now models of high sophistication available. These models are capable of reproducing both healthy and pathological behaviour with some accuracy.

1.2.1 Categorising Myocyte Models

Cellular models tend to be classified in two ways. The first differentiator is the level of detail employed. The second is which cellular processes are modelled.

Biophysically detailed models are complex. They consider the interactions of several different currents, and potentially intra- and extracellular ion concentrations, reservoirs as well as other details. The second type are simplified, phenomenological, models. These do not consider individual ion concentrations but instead just reproduce one desired factor, typically the action potential profile.

Models, whether biophysically detailed or not, can concern themselves with the cellular electrophysiology, the mechanical contractions or both. This thesis concerns itself just with electrophysiological models. Models of the mechanics are not considered and are not treated in this description of mathematical modelling.

1.2.2 A Brief History of Cardiac Myocyte Modeling

The first model of cardiac electrophysiology was published by Noble [12], and modelled Purkinje fibre (A specialised part of the ventricular conduction system) action potentials. Shortly thereafter, various refinements were published, as further experimental data became available. This was eventually followed by the Beeler–Reuter [13] model of the guinea pig ventricular myocyte.

The Luo–Rudy guinea pig ventricular myocyte model was first published in 1991 [14] and was then sub-sequentially majorly revised and republished in 1994 [15]. The first Luo-Rudy model was based on the Beeler–Reuter model, though with updated channel behaviours and more complex potassium channels. The second Luo-Rudy model was the first of the ‘second generation’ models, with fluctuations in all ion concentrations, and a much more detailed series of equations for calcium handling.

In 1998, the Courtemanche–Ramirez–Natel [16] (CRN) model and the Nygren [17] model were published. These were both models of the human atrium. They were also both second generation models, with detailed calcium handling. Also in 1998 Fenton and Karma published their phenomenological Fenton–Karma [18] model, which used just three channels to reproduce the shape of the ventricular action potential.

1.2.3 Mathematical Models of Myocytes

Mathematical models of cardiac myocytes are built from a few simple assumptions and considerations. These concern the behaviour of the cellular membrane and ion channels. The important ones are detailed here.

The Nernst Equilibrium Potential

The Nernst equation is an important equation in electrophysiology [19]. It describes how the difference in ion concentrations on two sides of a semi-permeable

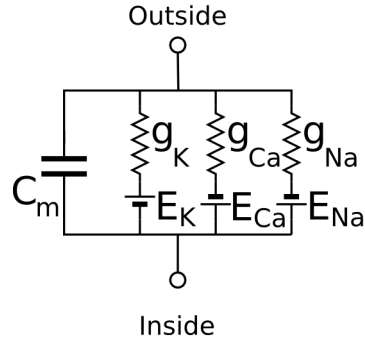


Figure 1.4: Electrical circuit representation of the cell. The cell membrane is represented by a capacitance, C_m . There are three currents, represented by the resistances g_K , g_{Ca} and g_{Na} . The current through the resistances is driven by the three Nernst potentials, E_K , E_{Ca} and E_{Na} .

barrier can result in a potential difference across the barrier. Any voltage dependent factor of a current of an ion, S , includes a reversal potential, V_S , equal to the Nernst potential. At the reversal potential, the current falls to 0. When equilibrium is reached the potential difference, V_S , across the membrane is given by

$$V_S = \frac{RT}{zF} \ln \left(\frac{[S]_e}{[S]_i} \right) \quad (1.1)$$

where subscripts i and e denote internal and external concentrations of S , R is the universal gas constant, T is the absolute temperature, F is Faraday's constant and z the charge of the ion S .

The Nernst Potential applies only to a single ion concentration. Since many ion channels are ion channel specific, the Nernst potential can still be used to calculate the driving potential.

Electric Circuit Model

The electrical circuit model of the cell membrane underpins much of the work in modelling the behaviour of cardiac myocytes. It is however a very simple concept. Since the membrane separates charges, it may be considered as a capacitor, as shown in figure 1.4. Since there is no net buildup of charge on either side of the membrane, any ionic current, I_{ion} , must be countered by a capacitive current,

and so

$$C_m \frac{dV_m}{dt} + I_{\text{ion}} = 0 \quad (1.2)$$

where V_m is the membrane voltage, and is defined as the difference between the internal potential, u_i and the external potential, u_e or

$$V_m = u_i - u_e \quad (1.3)$$

When multiple currents are considered, the total inward and outward currents are summed. The difficulty comes in determining the form of I_{ion} , which varies widely depending on the nature of the channel or pump in question.

The Hodgkin-Huxley Equations

Many mathematical models of cardiac myocytes feature one or more ‘Hodgkin–Huxley’ channels. Hodgkin and Huxley developed them in a now classic series of papers concerning the current flow through the membrane of the squid giant axon [20, 21]. They characterise the current flow with elegance and surprising accuracy. It is important to note that the Hodgkin–Huxley equations consider the bulk behaviour of the many thousands of individual channel structures distributed across the membrane, not the behaviour of one single channel.

Hodgkin and Huxley started with a very simple assumption. The current flow through a channel on the membrane, I_S is given by

$$I_S = g_S (V - V_S) \quad (1.4)$$

where g_S is the channel conductance, V the membrane potential and V_S the Nernst potential for the ion S . Equation (1.4) assumes that the channel is selective for one ion species S , and that the current is a simple linear function of the voltage across the membrane.

With this underlying assumption, Hodgkin and Huxley set out to accurately map the behaviour of the current with regards time and voltage. The following section explains the description for the sodium current, I_{Na} . From the form of the sodium channel under voltage clamp conditions, it is reasonable to expect g_{Na} obeys a differential equation of the form

$$\frac{dg_{Na}}{dt} = f(v, t) \quad (1.5)$$

where $v = V - V_{Na}$. However, the form of g_{Na} is complex. While remaining at the same voltage, the conductance at first increases and then tails off. It appeared that there were two processes at work, one that turned the current on, and one that turned it off. Hodgkin and Huxley realised that it would be easier to write g_{Na} as a function of two different variables. One which corresponded to the turning on and one to the turning off of the channel. This leads to there being an activation variable, called m , an inactivation variable, called h and that the current would be some linear combination of the two, multiplied by a constant conductance factor \bar{g}_{Na} . The two variables m and h would both satisfy a differential equation such as

$$\frac{dm}{dt} = \alpha_m(v)(1-m) - \beta_m(v)m \quad (1.6)$$

where α_m and β_m are functions of v ($= V - V_{Na}$). As m is an activation, α_m and β_m are such that m is initially small but increases with the potential allowing current to flow within the channel. As h is an inactivation, α_h and β_h give an initially high value of h that then decays, inactivating the channel.

The form proposed for g_{Na} by Hodgkin and Huxley was

$$g_{Na} = \bar{g}_{Na}m^3h \quad (1.7)$$

where all symbols are as defined previously. The decision to raise m to the third power was based on the rate of increase observed in voltage clamp experiments. It is interesting to note that when the structure of I_{Na} was examined in detail, it was discovered that the channel has three structures which open to allow current to flow. A second type of structure, the ‘ball and chain’, then acts to close the channel.

Many different channels are modelled as Hodgkin–Huxley channels. Different channels have different activation and inactivation variables. These variables are modulated by different α and β equations.

Markov Chain Descriptions Of Ion Channels

Markov chain models of ion channels [22–24] emerged when more detailed information on ion channels became available. This included single channel recordings rather than whole cell recordings. In such conditions, as well as in certain pathological states, the Hodgkin–Huxley descriptions of the cells broke down.

In a markov chain model, instead of having one or more activations or inactivations, the channel has a number of states. Common states can include open, inactive and closed. A channel can have more than one state of each sort. Transitions are only allowed between certain states and each transition has a, usually time or voltage dependent, probability. Channels only allow current to flow whilst in an open state.

Markov chain models can be highly complex and contain many states. They can be utilised in a variety of ways. One markov chain can represent the behaviour of all the individual channels on the cell. In this case, the total current flowing in the channel will be proportional to the fraction of open states. Cells can also have multiple markov chains to represent the flow through a channel, each with its own proportions of state occupancy. They also open the possibility of using stochastic simulation techniques where the transition between states is controlled by random chance.

1.2.4 Selected Myocyte Models

There are many myocyte models of varying complexity and accuracy. There are relatively few models of atrial myocytes for human tissue. A brief description of the foremost two are given here, as well as a description of one of the most adaptable phenomenological models.

The Courtemanche–Rameriz–Nattel Model

The Courtemanche–Rameriz–Nattel (CRN) model [16] is a biophysically detailed second generation model of the human atrial myocyte. It was based on the Luo–Rudy [15] model of the guinea pig ventricular myocyte. The currents were then modified based on data from human and animal atrial myocytes.

The CRN model tracks 21 state variables. Most of these are gating parameters for the many ion channels, but the model also tracks the internal concentration of potassium, sodium and calcium ions. The external concentrations of ions are assumed constant. There are also state parameters representing the calcium stored in internal structures, such as the sarcoplasmic reticulum.

$$\begin{aligned} I_{\text{ion}} = & I_{\text{Na}} + I_{\text{K1}} + I_{\text{to}} + I_{\text{Kur}} + I_{\text{Kr}} + I_{\text{Ks}} + I_{\text{Ca,L}} \\ & + I_{\text{b,Na}} + I_{\text{b,Ca}} + I_{\text{NaK}} + I_{\text{NaCa}} + I_{\text{p,Ca}} \end{aligned} \quad (1.8)$$

The CRN has 12 transmembrane currents and pumps which contribute to I_{ion} , equation (1.8), and 4 currents and pumps which just interact with the internal calcium stores. The external currents are I_{Na} , the fast sodium current, $I_{\text{K}1}$, the inward rectifier potassium current, I_{to} , the transient outward current, I_{Kur} , the ultra-rapid delayed rectifier current, I_{Kr} , the rapid delayed rectifier current, I_{Ks} , the slow delayed rectifier current, $I_{\text{Ca,L}}$, the L-type calcium current, $I_{\text{b,Na}}$, the sodium background current and $I_{\text{b,Ca}}$, the calcium background current. All the currents are time-dependent and voltage, except for the background currents which have constant conductance and $I_{\text{K}1}$, which is just voltage-dependent. There are also three pumps; I_{NaK} , the sodium–potassium exchanger, I_{NaCa} , the sodium–calcium exchanger and $I_{\text{p,Ca}}$, the calcium pump.

As a biophysically detailed model, the CRN model is suitable for a variety of modelling tasks. The number of currents make it an attractive option for modelling drugs or genetic mutations. It can be expensive to solve for large numbers of cells, however.

The Nygren Model

The Nygren model [17] is a biophysically detailed second generation model of the human atrial myocyte. It was based on the Linblad [25] model of the rabbit atrium. The equations were then modified using human data, mostly gathered from the atrial appendages.

The Nygren model tracks 29 state variables. Most of these are gating parameters. They model also tracks concentrations of ions, both internally and in extracellular cleft spaces, to represent local ion fluctuations. Like the CRN model, there are also variables to represent internal calcium handling.

$$\begin{aligned} I_{\text{ion}} = & I_{\text{Na}} + I_{\text{K}1} + I_{\text{to}} + I_{\text{Kur}} + I_{\text{Kr}} + I_{\text{Ks}} + I_{\text{Ca,L}} + \\ & I_{\text{b,Na}} + I_{\text{b,Ca}} + I_{\text{NaK}} + I_{\text{NaCa}} + I_{\text{p,Ca}} \end{aligned} \quad (1.9)$$

The Nygren model has 12 transmembrane currents and pumps which contribute to I_{ion} , equation (1.9), and 4 currents and pumps which just interact with the internal calcium stores. The external currents are: I_{Na} , the fast sodium current, $I_{\text{K}1}$, the inward rectifier potassium current, I_{to} , the transient outward current, I_{Kur} , the ultra-rapid delayed rectifier current, I_{Kr} , the rapid delayed rectifier current, I_{Ks} , the slow delayed rectifier current, $I_{\text{Ca,L}}$, the L-type calcium current,

$I_{b,\text{Na}}$, the sodium background current and $I_{b,\text{Ca}}$, the calcium background current. All the currents are time- and voltage-dependent, except for the background currents which have constant conductance and I_{K1} , which is voltage-dependent. There are also three pumps; I_{NaK} , the sodium–potassium exchanger, I_{NaCa} , the sodium–calcium exchanger and $I_{p,\text{Ca}}$, the calcium pump.

The Nygren model has more involved mathematics and requires more storage than the CRN model, making it less attractive for large-scale simulation. It is also interesting to note that the two models have very different AP morphologies, the reasons for which have been the subject of some research [26–28].

The Fenton–Karma Model

The Fenton–Karma (FK) model is a phenomenological, minimal variable, model of the ventricular action potential. The goal of the FK model is to accurately reproduce the AP profile and restitution properties of myocytes as well as short-term memory effects. The original FK model has 3 variables, a fourth was added recently [18, 29].

The FK model tracks 4 state variables. These have no true physiological analogues, but certain correlations can be drawn.

$$I_{\text{ion}} = I_{\text{fi}} + I_{\text{si}} + I_{\text{so}} \quad (1.10)$$

The FK model has 3 transmembrane currents which contribute to I_{ion} , equation (1.10). The fast inward current, I_{fi} , is roughly analogous to the fast sodium current in more detailed models, the slow inward current, I_{si} , fulfils a similar role to the L-type calcium current and the slow outward current, I_{so} , is analogous to the potassium rectifier currents. The behaviour of the currents is generally controlled by step functions based on the state variables.

The FK model is not biophysically detailed. This makes it very fast to solve, making it attractive for large tissue simulations. The drawback of this is that incorporating complex hormonal or drug interactions is difficult. The model is highly modifiable, with parameter sets that can reproduce a variety of AP morphologies and restitution behaviours, including one for atrial myocyte APs [30].

1.2.5 Models of Action Potential Propagation

Single myocyte models are important, and can tell us much about the heart in disease and health. The heart is not made up of isolated myocytes however. Whilst current computational power does not allow myocytes to be modelled on an individual cellular basis for the whole heart, continuum models of propagation have been developed. These are summed up in the bidomain equations, and their simplification, the monodomain equations.

The Bidomain Equation

The bidomain equation comes out of basic electromagnetic theory and several assumptions about the nature of cardiac tissue [31, 32].

1. The cardiac tissue contains two continuous, simply connected domains, the intracellular and extracellular domains. There is no detailed consideration of the fine points of geometry.
2. The intra- and extracellular domains overlap and fill all of the cardiac muscle. Each point lies in both domains.
3. Charge does not accumulate.

The derivation, starting from Maxwell's Equations, is not that difficult to work through and it results in the bidomain equations:

$$\underline{\nabla} \cdot ((M_i + M_e)) \underline{\nabla} u_e + \underline{\nabla} \cdot (M_i \underline{\nabla} V_m) = 0 \quad (1.11a)$$

$$\underline{\nabla} \cdot (M_i \underline{\nabla} V_m) + \underline{\nabla} \cdot (M_i \underline{\nabla} u_e) = \chi C_m \frac{dV_m}{dt} + \chi I_{ion} \quad (1.11b)$$

where the subscript i and e refer to the intra- and extracellular quantities, M is a matrix of conductivities, χ represents the surface-to-volume ratio of the cells and all other quantities are as defined previously. The bidomain equations are a coupled set of a parabolic and elliptic differential equation.

Boundary conditions for the bidomain equations vary, though the most common ones are described here. First, no intracellular fluxes leave the heart. Second, the body is assumed to be a passive conductor that is isolated at the outer surface. The body potential at the surface of the heart is the extra-cellular potential at the surface of the heart.

The Monodomain Equation

While the bidomain equations represent a good tool for modelling some of the complexities of cardiac conduction, they are very demanding to solve, necessitating finding the solution to coupled parabolic and elliptic differential equation sets. The monodomain equation is the result of one simplifying assumption made to the bidomain equations. For the monodomain equation, we assume that the anisotropy ratio, λ , is the same for the intra- and extra-cellular fluids at all points.

$$M_i = \lambda M_e \quad (1.12)$$

This assumption is not a very physiological one, but the simplification it allows is significant and so it is quite commonly used.

Substituting (1.12) into (1.11a) and (1.11b) and rearranging reduces the pair of equations to one single equation for the membrane potential

$$\frac{\lambda}{1 + \lambda} \nabla \cdot (M_i \nabla V_m) = \chi C_m \frac{dV_m}{dt} + \chi I_{ion} \quad (1.13)$$

Typically, the factor of $\lambda / (1 + \lambda)$ is folded into M_i , along with χ and the membrane capacitance C_m to give the diffusion tensor D . In 1D, this is the cable equation. The values of the components of the tensors M_i or D may be determined experimentally, or from a comparison of conduction in real and virtual tissue samples.

1.2.6 Numerical Techniques

There exist a wealth of techniques for solving the ordinary differential equations (ODEs) and partial differential equations (PDEs) involved in mathematical models [33]. These techniques vary in complexity and accuracy. The correct choice of technique depends on a number of factors including the ‘stiffness’ of the equations, the desired accuracy and others.

The Forward Euler Method

The forward Euler method [34] is perhaps the simplest numerical integration technique. It requires a relatively small (time) step between integration points. It is never-the-less quite suitable to use in simulations of the electrical activity of

the heart. A typical set of ODEs representing the electrical activity of a myocyte are very ‘stiff’, which is to say they can be numerically unstable if the step size is too large, and so more sophisticated methods can also require a very small timestep.

The forward Euler method works as follows. If we have a function, $f(t, u)$, for which we know the initial values, (t_0, u_0) , then by assuming the rate of change of f remains constant over some small interval, h , we can integrate the equation as follows

$$t_{n+1} = t_n + h \quad (1.14a)$$

$$u_{n+1} = u_n + h f(t_n, u_n) \quad (1.14b)$$

As long as the interval is small enough the sequence u_1, u_2, \dots, u_n should be a good approximation of the time evolution of u . If we have more than one value on the right hand side of the equation ($u = u^{(1)}, u^{(2)}, \dots, u^{(n)}$) then all values of the right hand side are assumed constant for each step of the integration. In cardiac systems, h is typically 0.02 ms or smaller.

The Finite Difference Method

The finite difference method [35] is a way of calculating the solution to a spatially extended problem. Such problems include PDEs such as the bidomain (1.11) and monodomain (1.13) equations. The general form of such equations in the variable $u(t, u)$ is

$$\frac{\partial u}{\partial t} = \frac{\partial}{\partial x} \left(b(t, x) \frac{\partial u}{\partial x} \right) + c(t, x)u + d(t, x) + e(t, u) \quad (1.15)$$

Where t is the time, x is the spatial variable and b, c, d and e are known functions. The function e will quite often be I_{ion} for a particular cell.

In the finite difference method, the problem space—the cardiac tissue, in this thesis—is divided up into a number of nodes. The spacing between each node is Δx in the x direction (and in higher dimensions, Δy in the y direction and so on). To advance the solution in time, the forward Euler method (1.14) can be used. To approximate the differential in space, the centred second difference can be used. For the node at x_i at time t_n it is:

$$\frac{\partial^2 u}{\partial x^2}(x_i, t_n) \approx \frac{u(x_{i+1}, t_n) - 2u(x_i, t_n) + u(x_{i-1}, t_n)}{(\Delta x)^2} \quad (1.16)$$

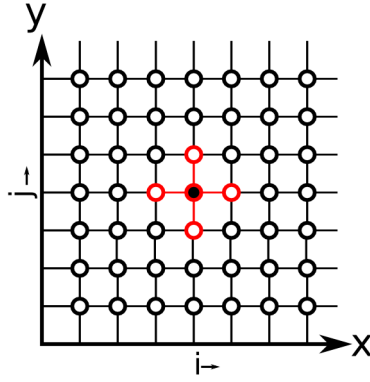


Figure 1.5: Representation of the finite difference method in two dimensions. The stencil of the central node (solid black) is indicated in red.

where i is the index of the node, and n the index of the instant of time. The space centered first difference (needed when conductional anisotropy is to be taken into account) is:

$$\frac{\partial u}{\partial x}(x_i, t_n) \approx \frac{u(x_{i+1}, t_n) - u(x_{i-1}, t_n)}{2(\Delta x)} \quad (1.17)$$

The most common boundary conditions we want to apply are Neumann, ‘no flux’, boundary conditions where the differential of u with respect to x is set to zero at the edges of the tissue. At the edge of the tissue, the approximation for the space differential (1.16) becomes:

$$\frac{\partial^2 u}{\partial x^2}(x_i, t_n) \approx \frac{2((u(x_{i-1}, t_n) - u(x_i, t_n))}{(\Delta x)^2} \quad (1.18)$$

if the node at x_{i+1} would be ‘outside’ the tissue. The approximation if the converse is true (x_{i-1} is outside) replaces x_{i-1} with x_{i+1} . The one dimensional approximation becomes:

$$\frac{\partial u}{\partial x}(x_i, t_n) \approx \frac{u(x_i, t_n) - u(x_{i-1}, t_n)}{(\Delta x)} \quad (1.19)$$

again, for if the node x_{i+1} is outside. In higher orders, (1.16) and (1.17) are applied along each direction. The nodes used in the calculation of the value u_x are known as the stencil. The typical 5-node stencil used for solving (1.15) and hence (1.11) or (1.13) is illustrated in figure 1.5. Other schemes can use different stencils.

The Rush–Larsen Technique

The Rush–Larsen technique [36] is a specialised way of solving equations such as (1.6) for the gating parameters. Since α_m and β_m are dependent only on the voltage, not on time, a solution to (1.6) [20] is:

$$m = m_{\text{inf}} - (m_{\text{inf}} - m_0) \exp\left(-\frac{t}{\tau_m}\right) \quad (1.20)$$

where

$$m_{\text{inf}} = \frac{\alpha_m}{\alpha_m + \beta_m} \quad (1.21)$$

and

$$\tau_m = \frac{1}{\alpha_m + \beta_m} \quad (1.22)$$

where m_0 is the initial value of m .

Rush and Larsen realised that over a sufficiently small time interval, Δt , the parameters α_m and β_m could be considered constant. Taking m_0 to be the value of $m(t)$ at time t , (1.20) could be used to calculate the next value of m , $m(t + \Delta t)$ as:

$$m(t + \Delta t) = m_{\text{inf}} - (m_{\text{inf}} - m(t)) \exp\left(-\frac{\Delta t}{\tau_m}\right) \quad (1.23)$$

Using (1.23) is more accurate than the forward Euler method (1.14), since it depends only on the value of the membrane potential, not the derivative of m .

1.3 The Electrocardiograph

The electrocardiograph, or ECG, was developed by Einthoven and colleagues at the turn of the 20th century. The Einthoven ECG used the string galvanometer, developed by Einthoven himself, to record the potential differences between three sets of electrodes, or leads. These electrodes were placed on each arm and on the left leg. These three electrodes form the basis of many ECGs recorded to this day. The string galvanometer was highly sensitive electrical recording device for its time. For the development of the ECG and the string galvanometer, Einthoven was awarded the Nobel prize in 1924 [37, 38].

Since Einthoven's day, the ECG has been continually refined. This refinement has included both improvements in the way that individual leads are measured, and new leads that are recorded. In addition, there have been a number of

specialised lead sets developed for particular purposes, such as exercise recording and 24 hour measurement. Research into new lead sets, to better understand the functioning of the heart, continues to this day [39–42].

1.3.1 Lead Theory

In Einthoven’s original conception of the heart and the electrical field it produced, he proposed the ‘Einthoven Triangle’. The Einthoven triangle is an equilateral triangle. At its corners sit the three electrodes and the sides of the triangles are the leads themselves. At the centroid of the triangle sits the heart, which is represented by a single, stationary, time varying dipole. The potentials measured at the three electrodes are the potentials assuming the system is two dimensional, homogeneous and infinite in extent. This is not entirely incorrect.

Modern lead theory was developed in the 1950s. In a series of three papers McFee and Johnston [43–45] set out their concept of the ‘lead field’ which is still considered applicable today. This theory, which was a further generalisation of work by Burger and van Milaan [46], allows for a heart which consisted of distributed dipole sources sitting in a three dimensional, finite and inhomogeneous medium.

First, it is useful to define what a lead is. A lead is defined as a pair of terminals, each connected to any number of electrodes on the body, either directly or through any number of resistors or amplifiers. One of the terminals is designated (arbitrarily) as the ‘positive’ terminal. The terminals are connected such that a positive measurement is taken if the ‘positive’ terminal has a higher potential than the ‘negative’ one.

The lead field theory is based on the fundamental principles of linear volume conductors set out by Helmholtz in the middle of the nineteenth century. These principles only hold if the body can be treated as a linear volume conductor. This is a good approximation [47].

The first principle, that of superposition, states that the electric field resulting from several sources in the medium is equal to the sum of the fields which would be produced by each source considered alone. The second principle, that of reciprocity, concerns current flow in the medium. It states that the current flow between two electrodes evoked by a field source in the medium is the same as the current flow through the source evoked by placing a potential difference across the two electrodes equal to the potential difference that would have been created

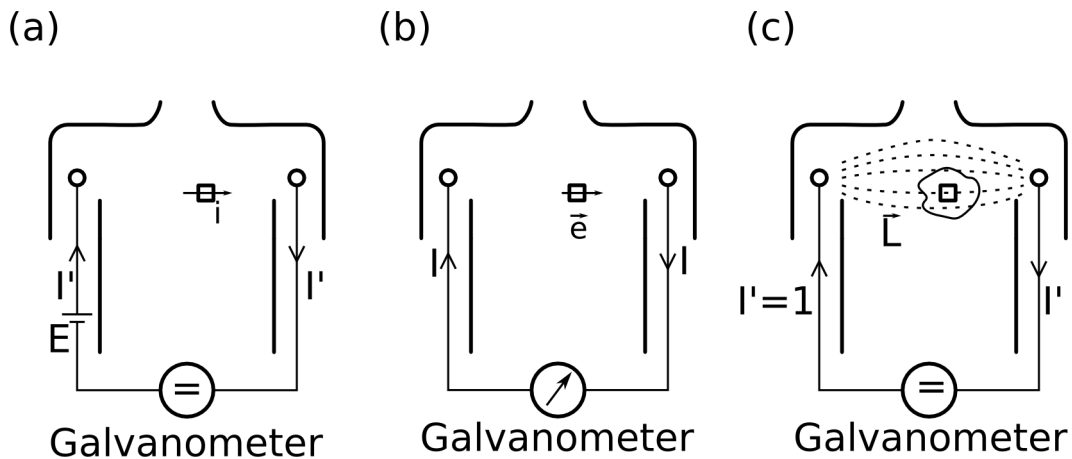


Figure 1.6: Diagram of the Reciprocity Principle and the Lead Field. (a) Inducing a current in the lead l , between the terminals of the galvanometer causes an electric field which causes a current i to flow through the small element (square) in the heart. (b) An electric field, \vec{e} , generated by the small element causes a current I to flow in l causing the galvanometer to read the potential difference E' . If E' equals E then I equals i . (c) The lead field, \vec{L} , is defined from the current which flows in each small unit of the heart when the current introduced is the unit current.

by the field source. That is to say that the current flow is independent of the direction of energisation, from within or outside the medium.

To derive the lead field, we consider a unit current flowing in a lead, l (figure 1.6). The resulting flow of current through the body will have a certain magnitude and direction at every point; it is a vector field. This vector field is called \vec{L} , the lead field. If one considers a small volume in the heart region of the torso then the presence of the lead field, \vec{L} , will set up an electric field in the volume, \vec{e} . The principle of reciprocity means that if instead the electrical activity of the heart creates an electric field, \vec{e} , in the heart region then a unit current will flow through the lead l . The principle of superposition allows the contributions of many such small volumes, each containing their own field, $\vec{e}_1, \dots, \vec{e}_n$, to create a current, and thus a potential difference in l .

1.3.2 The Twelve Lead Electrocardiogram

The twelve lead electrocardiograph is the initial basis of almost all cardiac diagnosis. It started out as the three Einthoven leads. The electrodes are located

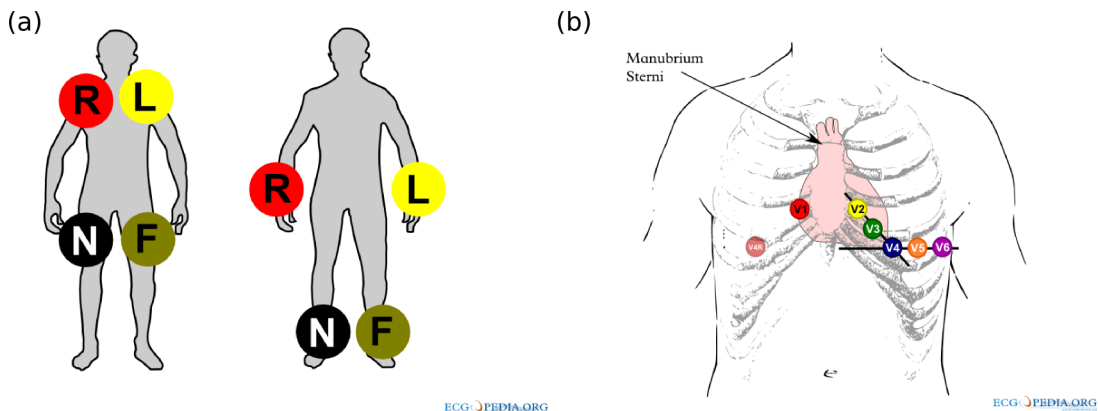


Figure 1.7: Lead placements for the 12 lead ECG. (a) Placement of the three limb leads, L, R and F, as well as the ground electrode N. (b) Placement of the six precordial electrodes, V_{1–6}.

Images are reproduced from the ECGpedia [48]. Both are kindly released under a Creative Commons Attribution-Noncommercial-Share Alike 3.0 Netherlands License.

(figure 1.7)(a)) on the left shoulder, L, the right shoulder, R, and the feet (typically the left leg), F. Lead I (1.24a) uses R as the negative terminal and L as the positive terminal. Lead II (1.24b) is formed between R as the negative terminal and F as the positive terminal. Lead III (1.24c) is formed between L as the negative terminal and F as the positive terminal.

Wilson [49], in the 1930s, introduced an indifferent electrode, constructed by averaging the potentials at the three limb electrodes (1.24d). This is the Wilson's central terminal (WCT). They introduced three new 'unipolar' leads, all of which use the WCT as the negative terminal. For the positive terminal, VL uses the L electrode, VR the R electrode and VF the F electrode. Later Goldberger [50] noted that by removing the electrode used as the positive terminal from the calculation of the central terminal for the negative electrode, the amplitude of the lead would be 50 per cent larger than that of the normal unipolar leads. These leads were termed the augmented unipolar leads, denoted by the prefix of an 'a'. The aVL (1.24e) leads uses L for the positive terminal and the average of R and F for the negative terminal. The aVR (1.24f) leads uses R for the positive terminal and the average of L and F for the negative terminal. The aVF (1.24g) leads uses F for the positive terminal and the average of R and L for the negative terminal. The set of leads consisting of I, II, III, aVL, aVR and aVF are known

as the limb leads. The superior limb leads are I, aVL, aVR and the inferior are II, III, aVF.

The precordial leads were introduced by Wilson [51] to provide a better view of the electrical activity of the heart from the chest. They are all unipolar leads which use the WCT for the negative terminal. For the positive terminal they use one of the six precordial electrodes (figure 1.7)(b), the locations of which are described in many textbooks (e.g. [52]). The first precordial electrode, which is the positive terminal of V_1 (1.24h) is located to the right of the sternum, in the fourth intercostal–between the ribs–space. The second precordial electrode, which is the positive terminal of V_2 (1.24i) is located to the left of the sternum, in the fourth intercostal space. The third, the positive terminal of V_3 (1.24j) is located between the second and fourth precordial electrodes. The fourth (V_4 , 1.24k) is located on the left midclavicular line, in the fifth intercostal space. The fifth (V_5 , 1.24l) is located on the left anterior axillary line, in the fifth intercostal space. The sixth (V_6 , 1.24m) is located on the left posterior axillary line, in the fifth intercostal space.

The voltage, V , across each lead can be written as

$$V_I = \phi_L - \phi_R \quad (1.24a)$$

$$V_{II} = \phi_R - \phi_F \quad (1.24b)$$

$$V_{III} = \phi_L - \phi_F \quad (1.24c)$$

$$V_{WCT} = \frac{\phi_L + \phi_R + \phi_F}{3} \quad (1.24d)$$

$$V_{aVL} = \phi_L - \left(\frac{\phi_R + \phi_F}{2} \right) \quad (1.24e)$$

$$V_{aVR} = \phi_R - \left(\frac{\phi_L + \phi_F}{2} \right) \quad (1.24f)$$

$$V_{aVF} = \phi_F - \left(\frac{\phi_R + \phi_L}{2} \right) \quad (1.24g)$$

$$V_1 = \phi_1 - V_{WCT} \quad (1.24h)$$

$$V_2 = \phi_2 - V_{WCT} \quad (1.24i)$$

$$V_3 = \phi_3 - V_{WCT} \quad (1.24j)$$

$$V_4 = \phi_4 - V_{WCT} \quad (1.24k)$$

$$V_5 = \phi_5 - V_{WCT} \quad (1.24l)$$

$$V_6 = \phi_6 - V_{WCT} \quad (1.24m)$$

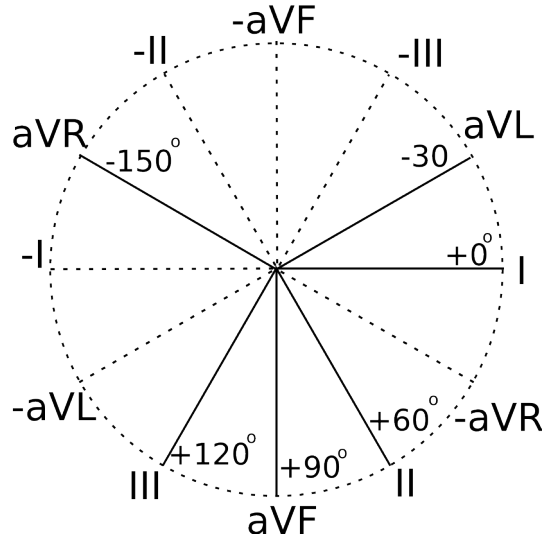


Figure 1.8: Diagram of the hexaxial reference reference system, showing the nominal directions of the 6 limb leads. The positive senses of the leads are in bold, the negative are dashed. $+0^\circ$ is horizontal and to the left, in the reference frame of the body.

where ϕ_x is the potential measured at electrode x .

As there are only 9 electrodes in the twelve lead ECG, there are only 8 potential differences which can be uniquely determined. These are, by convention, leads I, II and V₁₋₆. The value of the other limb leads is that they provide a view of the activity of the heart from different angles, thus what might be unclear on one lead can be obvious on another. This concept of lead angles creates what is known as the hexaxial reference system ([53], pp 94., amongst others), illustrated in figure 1.8. The angle at which each lead points is the direction of the positive terminal. Lead I, which is nominally horizontal, is at $+0^\circ$. Under the hexaxial system, Lead II has an angle of $+60^\circ$ and lead III, $+120^\circ$. The unipolar limb leads (both augmented and not) have angles of -30° for aVL, $+90^\circ$ for aVF and -150° for aVR.

1.3.3 The ECG Waves

In terms of the ECG, a ‘wave’ is a deflection from the baseline observed in the lead. There are five standard waves in the ECG; P, Q, R, S and T. The origin of the names of these waves is a matter of some controversy [54], but whatever their origin, they are now enshrined in the literature. A schematic representation

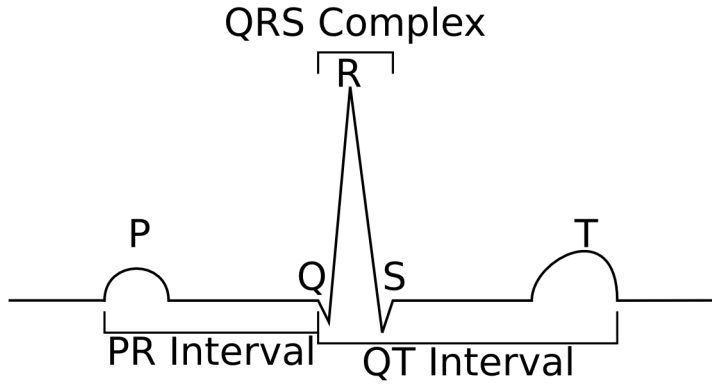


Figure 1.9: A schematic representation of the ECG in lead II. Shown are the P-wave, the QRS complex and the T-wave. Also indicated are two important time periods; the PR interval and the QT interval.

of the ECG waves is shown in figure 1.9. Each of the waves is the result of the electrical activity in a particular part of the heart. Positive deflections are those which are above the baseline and negative ones below.

The P-wave is caused by the depolarisation of the atria. It has a relatively low amplitude because the atria are small and thin walled compared to the ventricles, so there are not that many cells which can generate the wave. It tends to last from 100 ms to 120 ms.

The QRS complex is associated with the ventricular depolarisation. It is a collection of up to three waves. Any negative deflection which precedes the R wave is the Q wave. The R wave is the first positive deflection. The S wave is the first negative deflection after the R wave. A QRS complex does not need to have all three of the QRS waves present. The QRS complex tends to have the largest magnitude in the ECG and lasts approximately 100 ms.

The T wave is associated with the ventricular repolarization. It occurs some time after the QRS complex. The T_P , caused by the atrial repolarization is not normally visible on the ECG for a number of reasons. It is very small in magnitude, it is also often masked either by the QRS complex or by so called ‘baseline correction’ algorithms which use the PR interval to determine a ‘zero’ for the ECG.

The axis of a wave is the direction in which it has maximum amplitude according to the hexaxial reference system. A normal QRS complex ([3,53]) has an axis between -30° and $+110^\circ$. A normal P wave axis is between $+0^\circ$ and $+90^\circ$.

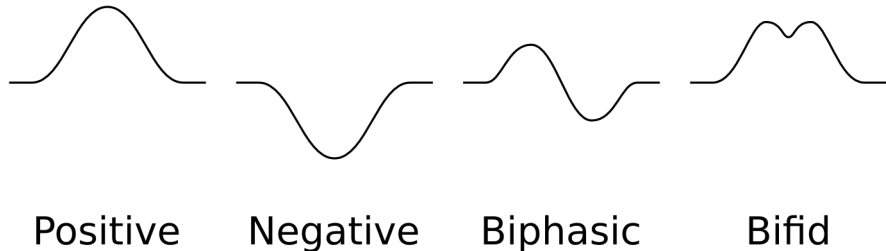


Figure 1.10: A schematic representation of P- and T-wave morphology. From left to right, a positive, negative, a positive–negative biphasic and a positive bifid wave are shown.

Describing an ECG Wave

The terminology used to describe ECG waves is illustrated in figure 1.10. Positive waves, those with a deflection above the baseline, and negative waves, with a deflection below the baseline have already been explained. The P- and T-waves can have more complex morphology however. A P- or T- wave which shows both positive and negative deflections is termed biphasic. A positive–negative biphasic deflection is one which is first positive and then negative. A wave for which the converse is true is called negative–positive. A wave which is entirely positive, or negative, but that has a notch in the middle is described as bifid.

1.3.4 The Vectorcardiogram

Orthogonal lead systems, intended to measure the three independent components of the heart’s dipole, were first proposed in the middle of the 20th century. Frank [55], after experiments on physical models of the torso, proposed his ‘corrected’ orthogonal system. This was corrected in the sense that the three lead vectors measured were truly orthogonal and of equal magnitude in each of the three directions. This included the influence of internal conductive regions and variability in heart location. The system uses 7 electrodes. The three vectors chosen are X, a horizontal vector, positive to the left. The Y vector is vertical and is positive towards the feet. The Z vector is horizontal and positive towards the back.

The vectorcardiographic leads can be combined to visualize the electrical activity of the heart in three planes. These are the frontal plane, which combines

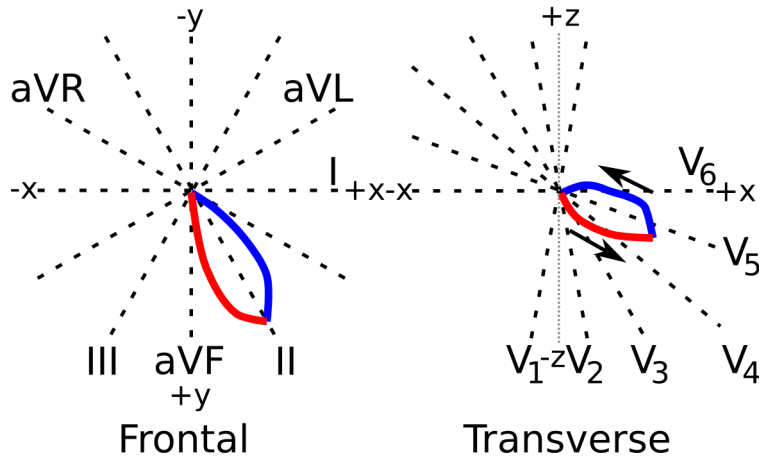


Figure 1.11: Schematic vector loops showing the relationships of the leads to the frontal and transverse plane. The lines of the leads are indicated in heavy-set black lines, the axes in grey dots when they do not coincide with a lead. The schematic loops are shown in red and blue, with arrows to indicate the direction of inscription. The afferent, or outgoing, limb of the loop is shown in red. The efferent, or incoming, limb of the loop is shown in blue.

Y and X, the transverse plane, which combines X and Z, and the sagittal plane, which combines Y and Z. The frontal plane is the one in which the limb leads measure, whilst the transverse plane can be related to the precordial leads, as illustrated in figure 1.11.

Dower [56] proposed a series of coefficients for the three Frank leads that would convert the Frank leads into the standard 12 lead ECG. However, the Frank leads are not recorded in common clinical practice. To remedy this fact, Edenbrandt and Pahlm [57] (and others, for example [58]), proposed an ‘inverse dower’ transformation. The inverse dower transform is a set of 8×3 coefficients (table 1.1) which are used to multiply the eight independent components of the twelve lead ECG (I, II, V₁₋₆) to form the three Frank leads.

1.3.5 Body Surface Potential Mapping Arrays

Body surface potential mapping arrays consist of many electrodes distributed over the body and recorded simultaneously. These allow the whole of the body surface potential to be examined and to be used to establish diagnostic criteria (for example, [59, 60]). Mapping systems are also important for so called ‘inverse solutions’, where the cardiac sources are estimated from the external potentials

Table 1.1: Factors to construct the Frank VECCG from the standard 12 lead ECG set [57]. Each of the 8 leads are multiplied by the given parameters to provide the orthogonal Frank lead.

	V ₁	V ₂	V ₃	V ₄	V ₅	V ₆	I	II
X	-0.172	-0.073	0.122	0.231	0.239	0.193	0.156	-0.010
Y	0.057	-0.019	-0.106	-0.022	0.040	0.048	-0.227	0.886
Z	-0.228	-0.310	-0.245	-0.063	0.054	0.108	0.021	0.102

(for example, [61]). They are also used for the construction of new lead sets (for example, [40]). Arrays of anywhere from 16 to over 200 electrodes have been used in such studies.

1.4 The Forward Problem

The so-called ‘forward problem’ seeks to find a relationship between the electrical activity in heart and the potentials observed outside the heart, most usefully on the surface of the body. When looked at another way, it is a method of finding the lead field, \vec{L} , for a given body. The problem has been approached in a number of ways; experimentally, clinically and numerically.

1.4.1 Uses of the Forward Problem

The original investigations into the forward problem very much concerned themselves with finding \vec{L} . They sought to refine the understanding of such concepts as the einthoven triangle and the precordial electrodes and to more closely relate the differing potentials observed with what was happening in the heart. The experiments in the forward problem led to the lead field theory of McFee and Johnson [43] and the Frank vectorcardiogram [55].

Modern investigators of the forward problem use the solutions to perform similar investigations, such as the development of new lead systems [62]. Forward solutions are also used for investigations into ischaemia, ventricular and atrial fibrillation, conduction defects, amongst many. Forward solutions also form the basis, or are used in the refinement, of inverse solutions.

1.4.2 A Brief History of the Forward Problem

As has been mentioned, the initial uses of the forward problem were to determine how the activity of the heart related to the leads. These initial models tended to be real and physical models. Towards this end, one of the first models constructed was by Burger and van Milaan [46], who constructed a one third life-size model of the torso, filled with electrolyte solution. The model had a cork spine and sandbags to represent the lungs. The measurements from this model formed the basis for their refinements to the lead theory.

Of the early mathematical models Brody [63] is one of the most significant. His was a model of the influence of the highly conductive blood masses of the heart on the measured electrical field. The ‘Brody Effect’ is still used in literature today.

In the 1960s, numerical models of the torso started to appear [64, 65]. These initial models generally had a handful of dipoles, or even just one, to represent the heart. These were used to investigate the influence of dipole position and heterogeneities on the body surface potential.

In 1971 Rush [66] published his torso model. This was probably the ultimate torso model, literally and figuratively. The model was twice lifesize and incorporated internal inhomogeneities representing lungs, heart, heart blood, great blood vessels, liver, fat, skeleton and anisotropic skeletal muscle—though the model could be used without them as well. The cardiac activity was represented by a number of dipole sources which were located in the heart region of the torso.

In the 1980s, models of the heart and the torso gained more sophistication [67, 68], though they were still generally ventricular models, not models of the whole heart. Models of this era routinely used 10s of dipole sources. These models still did not include even primitive electrophysiology models, although towards the end of the decade, propagation of the excitation wavefront was being modelled [69].

Moving to the nineties and the turn of the millennium, the availability of medical imaging tools such as CT and MRI scans allowed more accurate models to be constructed [70, 71]. This is also when the first models began to appear which incorporated the atrium [71, 72]. Many of the models published in this era use myocyte models to simulate the propagation, some even using biophysically detailed models.

1.4.3 Numerical Approaches

Numerical solutions to the forward problem involve solving Maxwell's equations within the torso. The same assumptions which were made for the lead field theory (§1.3.1) are valid here. To reiterate them briefly, they state that the body is a linear volume conductor. There are no inductive or capacitive effects. Furthermore, due to the finite (and small) size of the body, there are no propagation effects to consider. The field in the body, \vec{E} is therefore given by

$$\vec{E} = -\nabla\phi \quad (1.25)$$

where ϕ is a scalar potential field. Current flow in the torso under these conditions is given by Ohms law, which states the total current flow, \vec{J} , is

$$\vec{J} = \sigma\vec{E} + \vec{J}^i \quad (1.26)$$

where σ is the conductivity tensor and \vec{J}^i is an impressed, or applied, current density which is generated by active sources, i.e. the heart.

Since the total current flow is solenoidal, i.e. the net current flow into and out of a volume is zero, via (1.26) we have that

$$\nabla \cdot \vec{J} = 0 = \nabla \cdot (\sigma\vec{E} + \vec{J}^i) \quad (1.27)$$

This can alternatively be written as

$$\nabla \cdot \vec{J}^i = \sigma\nabla^2\phi \quad (1.28)$$

If the body is homogeneous and isotropic, it becomes

$$\nabla^2\phi = \frac{\nabla \cdot \vec{J}^i}{\sigma} \quad (1.29)$$

which is Poisson's equation.

Finding ϕ for a given \vec{J}^i can be achieved using a volume or boundary based approach. Volume based approaches [73–75] involve dividing the body up into volumes of different conductivity. There is also the recent ‘Meshless Finite Element Method’ [76], which uses the nodes of a typical finite element method, but

not the elements. The solution for ϕ is found using a finite element or finite difference method. Boundary element based approaches [64, 71, 77, 78] divide the torso into regions of isotropic and uniform conductivity. The potential, ϕ , is found on the surfaces of these regions.

Volume based methods allow for a more complex model. Interior volumes can have internally varying or even anisotropic conductivity. They tend to be much more computationally intensive to solve, however, because the problem space is still three dimensional. In addition, the required element size can be quite small, especially for finite difference approximations. Keller [75] used a model with more than ten million torso elements, for example, whilst the finite element model used by Klepfer [74] has approximately one million elements and 168,000 nodes.

Boundary element based methods by contrast tend to be much simpler to solve. Typical model sizes are of the order of a thousand to ten thousand elements, as they reduce the problem space to a series of two dimensional surfaces. This reduces the computational effort required. However, since the solution is only computed at the surfaces, regions can only be uniform and isotropic.

1.5 Cardiac Simulation Toolkit

Extracting results from cardiac modelling requires a computational implementation of a cardiac model and then to drive this model through an experimental protocol. A cardiac simulation toolkit provides an implementation of the model, or models, and a way of driving them to produce results. In this way, they can simplify research for the investigator, saving time and effort of programming oneself.

1.5.1 Advantages of Cardiac Simulation Toolkits

Toolkits can be an attractive option for cardiac investigators. The most obvious benefit is intrinsic in the nature of toolkits—the investigator need not implement a potentially complex model themselves. This saves effort both in the initial programming and also in the subsequent validation of the model which is essential for ensuring an accurate model has been created. This can also reduce the need for boring and repetitive programming. It can also open up the field of cardiac modelling to those without programming experience, such as physiologists and physicians, allowing them to contribute their experience and opinions to the field.

Because a toolkit is intended to be used many times, it can be more feasible to incorporate more advanced techniques. These can include advanced solvers for ODEs and PDEs. The pay off for optimisation can also be higher.

There are also benefits in consistency, both within and outside the research group. This allows for easier comparison of results between separate studies and quicker checking for errors. This can be especially significant in large-scale models.

1.5.2 Disadvantages of Cardiac Simulation Toolkits

Toolkits are not without problems, however. Some of these problems might be implementation specific, but many cannot be entirely avoided. They can roughly be divided into usage problems and extension problems. Usage problems concern the day-to-day usage of the toolkit, whilst extension problems deal with the issue of making the toolkit do more.

One problem can be the complexity of the toolkit itself. Complexity can make toolkits hard, even intimidating to use. This can be mitigated through good documentation and logical layout.

A second problem is one of platform dependency. A toolkit might rely on features only available on one platform or only be available in binary packages for that one platform. This can be especially important when the time comes to extend into a high performance computing environment, which can often be based on a different architecture and platform to local resources.

A third problem, which is mostly implementation dependent, is one of configuration and output. Toolkits, especially those with graphical interfaces, can often only be setup through such interfaces. This can make setting up experiments with small variations tedious. The output can also be in a format which is only easily read by the toolkit itself, tying a user to the toolkit.

Bugs can be present in both toolkit code and bespoke code. Whilst the nature of toolkits can result in such a bug being found sooner, the bug has a potential to influence many studies if the toolkit is widely used. This can obviously be mitigated through appropriate testing.

Another problem can be one of ‘design impedance’, which can also be expressed as ‘When all you have is a hammer, every problem looks like a nail’. Toolkits tend to present an easy or preferred path for modelling studies. This

can make deviations from this path, even when they might be advisable for physiological considerations, harder.

Moving on from usage considerations, extension problems can also be significant. Closely related to design impedance is the difficulty toolkits can present in extension. If the toolkit is closed source, this is impossible, or nearly so. In addition, the internal complexity of a toolkit can make additions in open source implementations difficult.

1.5.3 Available Toolkits

There are several available toolkits, of differing scales and intended uses. These represent the different intents of the authors and contributors.

CellML

Whilst not a toolkit in its own right, the CellML repository, curated by the University of Auckland [79], represents a potentially useful resource for all cardiac modelers. Using an XML based markup language, CellML, the CellML repository contains representations of many electrophysiology models. From these XML documents, programs can create code to solve the system of equations representing the cellular model. Once a translator has been implemented, any model in CellML format should be easy to simulate.

CellML is used as a model input format for several toolkits. CellML suffers from two problems. The first is that writing complex mathematics for ionic channel function can be difficult in the XML based format. The second is that the API itself for translating the CellML code into a form which is possible to compile is also complex, although this problem need only be solved once for any given toolkit. This makes certain refinements of model code very easy, for example [80] used CellML models to automatically tablize cardiac models.

Cardiac Arrhythmia Research Package

The Cardiac Arrhythmia Research Package [81–84] (CARP) is a sophisticated library for large scale cardiac modelling. It is developed by Dr. Edward Vigmond and Dr. Gernot Plank. It is mostly implemented in C++.

CARP is intended to be a powerful and flexible cardiac simulation library. It is organised into three layers. The application layer is very high level and is intended

to be mostly free of the complexities of the underlying model and parallelisation. The interface layer deals with the complexities of parallelization and distributing cellular models over the grid. The ionic layer has all the individual cell models, which again requires no knowledge of parallelization.

CARP can handle both structured and unstructured input grids and can also perform dynamic grid refinement. The API provided by the toolkit is quite clean and provides access to powerful techniques to solve large systems. CARP doesn't currently support CellML model input.

CMISS

CMISS is a toolkit for solving problems in Continuum Mechanics, Image analysis, Signal processing and System Identification. It is developed by a group at the University of Auckland [85]. The CMISS package is a collection of programs and libraries for solving a variety of problems, including electrophysiology. It is implemented principally in Fortran. A compiled version is freely available from the project website, for linux only.

CMISS supports importing models from CellML. It includes quite powerful visualization capabilities in addition to the modelling capabilities it offers. The modelling implementation includes a variety of solvers for both ODE and PDEs.

CMISS is complex enough that it has its own language for configuration files which define the problem to solve. In addition several configuration files are needed to define one problem. It also outputs results in its own format, which can make interoperability with different visualisation difficult.

Cellular Open Resource

The Cellular Open Resource (COR) [86] is intended for single cell modelling. It is freely available from the website, for windows only. It allows editing of CellML files and execution of the models using a variety of integrators. COR can provide tracings of all currents and state variables as the action potential evolves. It also supports exporting models to a variety of formats, including C and Fortran.

COR only works on windows. The source code is not publicly available meaning that extension other than modifying models is not possible. Modification of models and specification of stimulus protocols is via its own programming language or direct modification of XML files.

Chapter 2

Constructing a Cardiac Simulation Toolkit

2.1 Simulation Environment

The simulation environment provided by the cardiac toolkit is intended to be as portable as possible, so that numerical experiments may be run on whichever platforms are appropriate. To this end, all the data input structures are based on open standards, or simple binary formats. The output formats provided by the various driver programs are also in simple binary or ASCII formats, to allow them to be easily visualized with both commercial and open source visualisation tools. The results presented later in this chapter were performed on desktop computers with a Athlon X2 3600+ chip and 1 GB RAM and on Horace, the local HPC facility. Horace has 24 compute nodes, each one consisting of four Intel Itanium2 Montecito Dual Core 1.6GHz processors, 16GB RAM and up to 512GB of local scratch space. The nodes are connected by a high speed Quadrics QsNetII interconnect. Horace provides compilers for both Fortran and C, and for both the MPI and OpenMP parallelization libraries.

2.1.1 Implementation

The experimental protocol drivers and the cellular models were implemented in the C programming language. Much of the supporting code and supplementary tools were implemented in the ruby programming language [87]. The cellular

models currently implemented are based on the Hodgkin-Huxley formalism, although there is no fundamental reason why a Markov chain based model could not be included. Inter-cellular coupling for propagation of excitation over a strand or tissue was implemented using the monodomain equations.

Cellular Models

The cellular model used for much of the developmental process was the Courtemanche et al. human atrial myocyte model [16]. Also currently implemented is the four variable formulation of the Fenton-Karma minimal variable model [29]. These cellular models describe the behaviour of a cell using coupled systems of non-linear ordinary differential equations. The ODEs represent the concentrations of intra- and extra-cellular ion species and the flow of current through ionic channels in the cell membrane or between intra-cellular compartments, or their notional equivalents in the case of minimal variable models.

These equations were integrated using the simplest time-stepping method available, the forward Euler method. To improve performance and stability, gating variables were integrated using the Rush-Larsen method. Whilst this does require a small timestep, the resulting models are relatively simple, making expansion easy.

Monodomain Equation

The monodomain equation (§1.2.5) was used to couple multiple cells together to describe a tissue over which excitation could be conducted. The rate of change of membrane potential, V , is given by

$$\frac{\partial V}{\partial t} = D\nabla^2 V - \frac{I_{\text{ion}}}{C_m} \quad (2.1)$$

where D is a constant representing the diffusivity of transmembrane potential through space, I_{ion} represents the total trans-membrane of a cellular model, such as I_{tot} from (1.8) and C_m is the membrane capacitance of the cell. A finite differences approach is used to discretize the model in 1D or 2D with an explicit Euler scheme used to advance the timestep.

Strand Model

The 1D strand model is used for several experimental protocols, as a computationally cheaper alternative to a full tissue model. The 1D strand model consists of a number of nodes, typically 200 or 300, which are coupled electrically at the ends of the cells. The electrical activity at each node is modelled via a cellular electrophysiology model. Electrical conduction between the nodes is handled via a 1D formulation of the monodomain equations using a 3-node approximation of the Laplacian, with no flux boundary conditions.

Sheet Model

The 2D sheet model is used for several experimental protocols, as well as more general numerical experimentation. The 2D sheet model consists of a grid of nodes, coupled electrically along the cardinal directions of the grid. The electrical activity at each node is modelled via a cellular electrophysiology model. Conduction of the electrical excitation between the nodes uses the monodomain equations with no flux boundary conditions applied at all tissue boundaries and a 5-node approximation of the Laplacian. The square sheet model, used in several of the numerical experimental protocols described later, is typically 375×375 nodes, representing 140,625 cellular models. Two dimensional idealizations of physiological preparations can have many more nodes, to on the order of 10^6 cellular models. These idealizations can often be quite irregular and so to allow easy and effective partition of workload across multiple processors, the tissue map is decomposed into a 1D array which contains references to the neighbouring cells.

2.1.2 Parallelization

Some parts of the toolkit require the modelling of large numbers of cells, on the order of tens or even hundreds of thousands of cellular models in two dimensional sheets. Solving all the equations involved takes a significant amount of time and so it is desirable for such simulations to be parallelized so that the work involved can be split over several processors. This can have advantages beyond merely having eight rather than one cores worth of computational cycles working on solving the equations. Splitting the work over multiple cores can also increase the amount of cache available, allowing for more efficient operation of the solvers. There are two libraries widely available for parallelization, OpenMP [88] and the

Message Passing Interface [89] (MPI). They are based around different paradigms for parallelism.

The OpenMP library is based around the ‘shared memory’ paradigm. Under the shared memory paradigm, there is only one process and this has access to all of the memory used in the program. The parallelism is achieved through the use of threads which divide up the work between themselves. This makes the implementation quite simple, but also limits the maximum number of computer cores which can be assigned to work on any individual execution of the problem.

MPI is based around the ‘message passing’ paradigm. The message passing paradigm involves multiple separate processes which use communication via the messages they pass between themselves to work. Each process has its own memory, and the only way for information in one process to reach another process is by explicitly passing it through messages. Because the processes each have their own memory, there is no requirement that the processes are on the same computer. This allows (theoretically) any number of cores to be applied to solving the problem. However, the explicit nature of message passing can make implementing a program harder and in addition, there can be significant lag due to the physical separation of the computers which can reduce efficiency.

For the parallelism involved in the library, the OpenMP parallelism library was chosen. This choice was made for a number of reasons. Implementations of OpenMP can be found on many systems, with gcc [90], icc [91] and the Sun compiler all having an OpenMP implementation. This makes the library suitable for use on both HPC systems and on modern multiple core desktops. In addition, for those systems on which running in parallel is not desirable, the same code can be compiled serially. Whilst an MPI implementation would allow more processors to be used to execute a task, in general 8 cores of Horace were found to be sufficient for running most jobs and in compiling for MPI some of the flexibility would be lost from the library.

2.1.3 Performance Optimisation

Optimisation is the process of improving a given quantity. In the context of performance, this involves reducing the running time whilst preserving the accuracy of the solution. The benefits of this should be obvious. Code which runs faster lets results be gathered sooner or allows more cases to be considered. Optimisation can be of particular benefit to a library, which is intended to facilitate code

re-use; the benefit of a little work can be garnered many times.

In general, all performance optimisation techniques involve reducing the number of operations required to compute the final result. This can take a number of forms. The simplest one is the choice of the compiler and the compile flags used, both of which can have a significant influence on the total computation time. However, moving beyond the compiler, a choice of algorithm can also be important in reducing the time taken. Several of the techniques used are presented here.

The Compiler

The library has been compiled using the GNU C compiler (gcc) [90] and the Intel C compiler (icc) [91]. Both have OpenMP implementations available and all three are capable of performing a number of optimisations, controlled via flags. The most important aspect of the optimisations is that they should not alter the behaviour of the floating point handling, as this could have significant impact on the final result computed. Despite this caveat, the results of applying certain optimisation flags can be quite significant, speeding execution by several percent.

Caching of Computed Values

Moving beyond the compiler, one of the simplest forms of optimisation is to only calculate each value once, if at all possible. This can be done in a number of ways and the library developed here implements two such methods for saving computational time.

State saving is one of the most direct ways of caching computed values. At a particular point in the simulation, all of the state variables of the system are copied into an intermediate location. This might be a file on disk or to another location in memory. If the state is written out to a file, that file can be used as a ‘save point’, allowing the simulation to be continued from that point in the future, ensuring work is not wasted.

When copied to another memory location, this allows the program to return to that point in the future. This is useful in modelling many experimental protocols, which often call for a number of ‘conditioning’ pulses to allow the cell or model to settle. The state can be saved after the conditioning pulses and then the actual tests can be performed quickly, saving the execution of several seconds of simulated activity. This technique should obviously only be used for cells in

the Hodgkin-Huxley formalism which are deterministic and thus give identical results whether the state is saved or not. Using such a technique with a cell that has a number of stochastic components could potentially affect the quality of the results.

The second way in which caching can be employed is in the creation of ‘lookup tables’ [80,92]. A lookup table is a pre-computed table of the values an expression can take. When the expression would normally be evaluated, the table is used instead, replacing what might be a complicated expression with a single array lookup.

To efficiently pre-compute values for a lookup table, two things must be true. The tabulated expression must depend on only one variable. The tabulated expression must also be sufficiently ‘complex’ or time consuming to compute. The requirement for complexity is perhaps the most obvious one. The most time that a lookup table can save is the cost of the original computation, so for significant savings in computational time, expensive calculations should be preferred. Good candidates for this are expressions which involve the computation of mathematical logs and exponentials. The requirement for dependence on only one variable is due to the nature of the table. It must be indexed by the steps in the dependent variable or variables. If there are N steps in a dependent variable to be tabulated, adding dependence on a second variable requires pre-computing and storing $N \times N$ values. The value of N varies, but is typically at least 1000.

With these limitations in mind, there are still a number of expressions that can be tabulated in the typical electrophysiological cell model. If the Rush-Larsen method has been used to integrate gating variables then the expressions for both steady state and time constant of the gate can typically be tabulated. Currents with a complex, but wholly voltage dependent form, such as I_{K1} in the Courtemanche et al. human atrial cell model can have the current calculation tabulated. Other calculations in a cell model must be evaluated on a case-by-case basis.

The use of lookup tables can significantly speed up code execution. It can also influence the results, due to the discretisation involved in the computations. However even a small number of steps, sufficient to discretise with a resolution of 0.1 mV, typically introduces a $\leq 0.1\%$ error. Meanwhile, a 5x or greater speedup is not impossible.

Binary Searches

Several of the experimental protocols provided by the library are intended to determine the value of a parameter which causes a particular condition to be fulfilled, such as a successful excitation of the cellular model after progressively shortening stimulus intervals. This value we will call the critical value. In real experiments, ones involving actual cardiac tissue, the typical experimental protocol would involve stimulating the tissue at sequentially shorter intervals, until no stimulation was provoked. This might involve stimulating the cell thousands of times, which would be expensive computationally to model exactly. Instead, a binary search [93] for the critical value can be performed, using the pseudo-code shown in Algorithm 1

Algorithm 1 Binary search for the critical value of the function $f(x)$. The critical value is defined as the smallest x which still makes $f(x)$ produce a value, v , greater than the threshold, t . The initial guesses for x are *high* and *low*. The guessing continues until sufficiently close for the accuracy condition to be fulfilled.

```

 $x_{high} = high$ 
 $x_{low} = low$ 
repeat
     $x_{current} = (x_{high} - x_{low}) / 2$ 
     $v = f(x_{current})$  // Compute  $v$  using  $x_{current}$ 
    if  $v \geq t$  then
         $x_{high} = x_{current}$ 
    else
         $x_{low} = x_{current}$ 
    end if
until  $(x_{high} - x_{low}) \leq accuracy$ 
```

To explain in words, first two guesses are made; the high guess, which is the maximum value that the critical value can take, and the low guess, the minimum it is presumed to take. The simulation is then run with the parameter set at the average of the low and high guesses—the current guess. If the test is successful, the critical value evidently lies somewhere between the low guess and the average, and so the high guess is set to the current guess. Conversely, if the test is unsuccessful, the critical value is obviously above the current guess, and so the low guess is set to the current guess. The simulation is then repeated with the average of the new high and low guess. Using this algorithm, the search space is halved with each iteration, swiftly finding the critical value. For example, to find a parameter

to an accuracy of 1 ms in a range of 250 ms statistically requires 125 sequential iterations. To find that same parameter using binary iterations requires just 8.

An important limitation of the binary search method is that there must only be one critical value. If there are two such values within the range, the result of the algorithm is unpredictable. In practice, this constraint is quite easy to work within.

Adaptive Step for Restitution Tracking

Adaptive step mechanisms are employed in the library when there is a need to provide output over a wide range of times, when the slope of the graph is not constant over the range to be graphed. This is very common in the modelling of cardiac cells, which often show an exponential dependence of various parameters on the stimulus interval, and are graphed over a range of hundreds or thousands of milliseconds. A step sufficient to track the curve at the upper limits of the range will completely fail at the steeper slope of the lower limits, whilst a step that will track the curve for the lower limits will result in unnecessary work being done at the upper end of the range. To alleviate this problem, an adaptive stepping mechanism is used, as shown in the pseudo-code Algorithm 2.

First, the measurement is performed at the largest desired point. The interval is then reduced by the step, and the measurement is performed again. The difference in the measurements is calculated and compared to the desired maximum delta. If the difference is acceptable, the interval is once more reduced by the step, and the measurement taken once more. If the difference is too great, then instead the step size is halved and the measurement repeated. If the difference is now acceptable, then the interval is reduced by the new step and the experiment proceeds. If it is not, then the step size is once more halved. The step size used is therefore always appropriate to the slope of the curve and a smooth graph results. Additional logic, not shown in the pseudo-code, is used to ensure the step size does not become too small, and to terminate the graph at the lower end of the range.

Since curves can increase or decrease the absolute difference between the two values is compared.

Algorithm 2 Adaptive stepping algorithm for calculating a value, v , for decreasing values of time, t with the function $f(t)$. t starts at t_{max} and is computed until t_{min} . The initial step size used to reduce t is $step$.

```

step = stepstart
factor =  $\frac{step}{2}$ 
vlast = f(tmax)
tprev = t
t = tmax - step
while t ≥ tmin do
    v = f(t)
    if |v - vlast| ≤ threshold then
        print t, v
        vlast = v
        tprev = t
        t = t - step
    else
        step = step - factor
        factor =  $\frac{factor}{2}$ 
        t = tprev - step
    end if
end while

```

Parallel Input/Output

Input and output for simulations is obviously essential if they are to be of any use. This input and output can involve the reading or writing of many megabytes or gigabytes of information over the course of a simulation, often in a variety of different formats. This most significant for sheet simulations and it is those that we consider here.

Data input is typically not that significant a cost for simulations, as whilst various simulation maps and saved states be quite large, the cost is typically only paid once. Data output is often required at numerous points throughout the course of the simulation since almost all simulations are performed to examine the time evolution of the cardiac system. Many simulations will output the value of state parameters, most commonly the voltage, at all points in the tissue every few milliseconds of simulated time. Other state variables might also be desired and the toolkit also offers ‘live visualization’ of two dimensional sheets via output of images in the GIF format. In addition, the whole state is output regularly, to allow simulations to be resumed at a later point in time. This output usually stops all simulation whilst it is being written to disk, time during which the

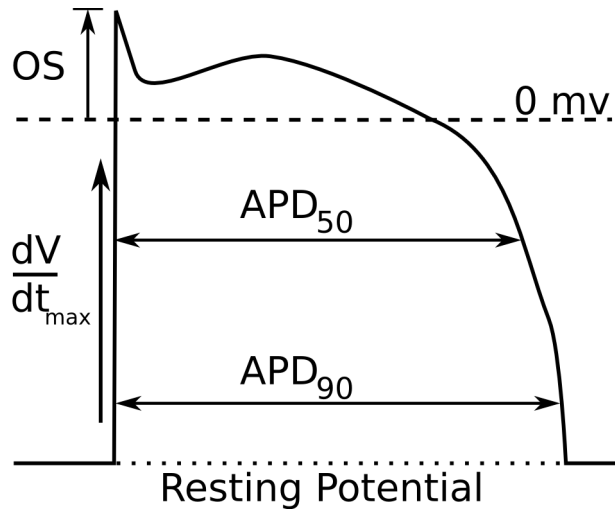


Figure 2.1: Schematic AP with various action potential properties noted. Shown are the overshoot (OS), APD₉₀, APD₅₀, $\frac{dV}{dt}_{\max}$ and the resting membrane potential.

processors are typically idle. By allowing multiple threads to output in parallel, the cost of outputting multiple files can be reduced to the cost of outputting one.

2.2 Experimental Protocols

The toolkit developed provides a number of experimental protocols to use with the cellular models to quantify the electrophysiological behaviour of the modelled cells. The provided protocols include the action potential duration at 90% repolarization (APD₉₀) and the action potential (AP) profile; the APDr,₉₀ and APDr,₅₀ restitution; the effective refractory period (ERP) restitution (ERPr); the conduction velocity (CV) restitution (CVr); the temporal vulnerability window to unidirectional conduction block (VW); the threshold of excitation and a flexible system for specifying two dimensional sheet experiments, including the initiation of re-entry via wavebreak protocols and computation of the spatial vulnerability window.

2.2.1 Action Potential

The action potential profile is one of the fundamentals of cellular modelling, with a number of associated properties, illustrated in figure 2.1. These include the action potential duration at 90% repolarization, APD₉₀; the action potential

duration at 50% repolarization, APD_{50} ; the maximal overshoot, OS; the upstroke velocity, $\frac{dV}{dt}_{\max}$ and the resting membrane potential.

To compute these quantities, the cell is paced N times at given S1 interval. After another S1 interval, a final AP is elicited from the cell and the properties are measured. In addition, it is common to want current and cellular model state traces over the course of an AP and these can be provided by the library alongside the membrane potential trace.

2.2.2 Action Potential Duration Restitution

The library calculates the APDr via a standard S1–S2 protocol used in both numerical simulations [94–99] and also in physiological experiments [100, 101]. The APDr is used as a measure of how the cell responds to stimulations at different rates.

A single cell protocol to evaluate the ADPr curve as results gained are similar to strand protocols [95, 99] with much less effort . The cellular model is paced $N - 1$ times with a stimulus close to the threshold value at a given stimulus interval, S1. At this point, the state is saved for the paced cells. The N th S1 stimulus is then given, followed by the S2 after a varying DI, which is reduced via an adaptive step to record the relationship between DI and the APD of the following AP. The toolkit also determines useful parameters such as the maximal slope of the restitution curve, which can be related to the stability of spiral waves within the tissue. Both the $\text{APDr},_{90}$ and the $\text{APDr},_{50}$ restitution can be calculated.

2.2.3 Effective Refractory Period Restitution

The ERPr is calculated by the library using standard experimental protocols [102, 103]. The ERP is defined as the shortest possible stimulus interval, S2, which still allows a successful AP to be elicited after pacing N times at a pacing interval S1. A successful AP is defined as an AP which has an amplitude of at least 80% of the magnitude of the preceding AP. The rate dependence of the ERP is evaluated at a decreasing S1 interval.

To find the ERP for a given S1 interval the cellular model is paced N times at that interval. The state is saved just before the $N - 1^{\text{th}}$ AP is initiated. The ERP is found via binary search. The low guess for S2 is typically chosen as zero, whilst

the high guess is the S1 interval being tested. The S2 interval for each attempt is the average of the high and low guesses. After the state has been saved, the N^{th} AP is initiated and its amplitude recorded. Then $S2$ ms after, the test AP is evoked. After the test AP has been allowed to run its course, the amplitude is tested and used to guide the next binary iteration. Details of the elicited APs, such as the S1 and S2 amplitudes and durations are stored. The binary iteration proceeds until the desired accuracy has been attained.

The reduction in S1 interval is stepped via an adaptive mechanism which is used to keep the reduction in ERP between successive S1 intervals to below 1 ms. The S1 interval is reduced until it is sufficiently short that the S2 interval would fall within the N^{th} AP.

2.2.4 Vulnerable Window

The VW measurement is based around a 1D ring model of cardiac tissue. It is used to quantify the vulnerability of cardiac tissue to the genesis of arrhythmia via re-entrant activity [104–106]. The VW is defined as the time period in the refractory tail of a propagating excitation wave that results in unidirectional conduction block. In the case of a ring model of the tissue this causes retrograde propagation, which forms a re-entrant excitation which cycles endlessly. If the stimulus is given too early, then the tissue will still be refractory in both directions and no propagation of excitation will ensue. If it is given too late, then propagation will occur in both directions, which in the ring case, results in the two excitation wavefronts annihilating each other. Normal pacing could then resume. These three cases are illustrated in figure 2.2.

The VW is found in a 1D strand model, set up as described previously. The use of an open-ended strand, not a connected ring, makes pacing the strand easier, but does not effect the results. The strand is 300 units long and with a space step of 0.1 mm. The strand is first given N S1 conditioning stimuli which are administered to a 3 node (0.3 mm) section at the start of the strand. Typically an S1 interval of 1000 ms is used with 10 S1 pulses. The test S2 stimulus is administered to a 4 node (0.4 mm) section, normally centred in the middle of the strand, $S2$ ms after the N^{th} conditioning excitation wave has passed the S2 stimulus site. To reduce the computation time, the state is saved at this point. The low guess for the binary iteration is chosen as 0 ms and the high guess as the S1 interval. To

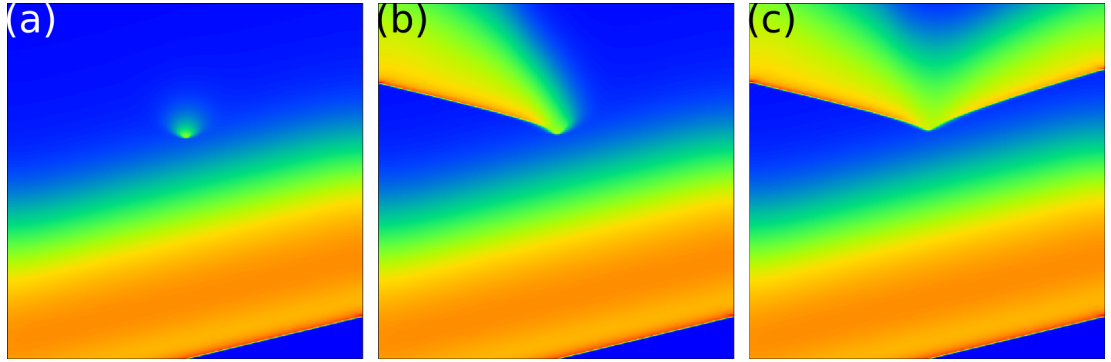


Figure 2.2: Illustrative space–time plots of the vulnerable window. In all plots, colour represents membrane potential from resting (blue) to depolarized (orange), position along the strand changes horizontally, whilst time advances upwards. Normal conduction is from left to right. In all plots, the latter half of the last S1 pulse can be seen in the lower right. (a) Complete Block. The stimulus is too early, and no excitation can be evoked. (b) Unidirectional Block. The stimulus has been delivered in the vulnerable window. The stimulus can propagate only back along the strand. In a ring, this would be re-entrant. (c) Bidirectional Conduction. The stimulus is delivered too late. The bidirectional waves will annihilate each other.

judge the success of the S2 stimulus, the ends of the strands are watched for successful excitation. If there are no excitation waves crossing the ends after the N^{th} excitation wave has passed, then it is in the region of total conduction block. If one excitation wave crosses the end, it is in region of unidirectional block. When two excitation waves cross the end, it is in the region of bidirectional conduction. The timing of the S2 stimulus is controlled via binary search, first to find the boundary of total conduction block and unidirectional block and then to find the boundary between unidirectional block and bidirectional conduction. A minor optimisation above the usual binary search algorithm is possible in this case, as a search for one boundary can be used to refine the range for the second boundary too.

2.2.5 Threshold of Excitation

The threshold of excitation is a theoretical measure, proposed by Zhang et al. [105] and used in modelling studies [103]. It is defined as the minimum stimulus current which, when delivered to a cell, will cause the cell to depolarize to a membrane potential of at least -20 mV . The threshold of excitation is calculated for a range of stimulus intervals, successively reducing the interval until it is impossible to

elicit a depolarization of sufficient magnitude. At each stimulus interval it is recorded if the test pulse elicits bidirectional, unidirectional or no propagation.

The threshold of excitation is found in a 1D strand model. The strand is 300 units long, with a space step of 0.1 mm. The strand is first given N S1 stimuli at a rate which allows the strand to recover between each excitation wave. Each S1 stimulus is delivered to the first 4 nodes (0.4 mm) and is chosen to be above the threshold of excitation. The threshold of excitation is calculated at the 100th node and so as this node depolarises, the state for the whole strand is cached.

The threshold of excitation is then found via binary search, with a lower bound of 0 nS and an upper bound chosen to be 5x the normal threshold. The test stimulus is delivered Δt seconds after the 100th node depolarises to a group of 4 nodes centred on the 100th node. After the test stimulus is delivered the 4 nodes are tested for the excitation condition, attaining a membrane potential of -20 mV. If it is successful, the current stimulus strength will be assigned to the high guess. If not, to the low guess. In addition, the simulation is continued to evaluate whether bidirectional, unidirectional or no conduction of the excitation wave is evoked by the stimulus. The strand is then reset to the cached state and the new stimulus strength is tested until a sufficient accuracy has been attained. Once the threshold of excitation has been determined for a given Δt the state of the strand is once more reset to the cached state and a shorter Δt tested.

2.2.6 Conduction Velocity Restitution

The CV is the rate of propagation of the excitation wave. It is determined by the difference in excitation times at two points divided by the distance between them. It is measured both in both experimental and numerical studies and is therefore useful in validating experimental results. A related measurement is the minimum conduction interval. The minimum conduction interval is the shortest interval between an S1 and S2 stimulus which still propagates successfully. It is similar to the ERP, but can also be influenced by inter-cellular coupling and heterogeneity in the strand. The CV_r is found via stimulating the strand at successively shorter intervals and noting the changes in the measured CV [28,105,107]. The minimum stimulus interval is found via noting when the curve ends.

The CV_r is found in a 1D strand model, set up as described previously. The strand is 300 units long with a space step of 0.1 mm. Stimuli above the stimulus threshold are delivered to a 4 unit (0.4 mm) length at one end of the strand. The

strand is first given N S1 stimuli. Typically an S1 interval of 1000 ms is used with 10 S1 pulses. The S2 stimulus is then delivered $S2$ ms seconds later. The CV is estimated from the difference in excitation times, defined as the instant at which the node is excited above -60 mV, at 2 nodes which are located 100 nodes apart. This minimizes any possible influence from boundary conditions. The S2 time is then stepped until a second excitation wave does not propagate the length of the strand.

2.2.7 Spiral Wave Dynamics

The dynamic behaviours of spiral waves are characterised by the stability, mobility and lifespan (LS). Spiral Wave LS is examined experimentally [108] and numerically [26, 98, 105, 109, 110]. The LS of the spiral wave and the meander pattern of the tip are both used to gain insight into the behaviour of the tissue under conditions of cardiac arrhythmia.

Spiral waves are initiated in a square sheet of tissue 375 x 375 nodes in dimension with a space step of 0.1 mm, as described previously. The tissue is first stimulated along one edge via a stimulus current applied to a row of nodes extending the length of the tissue and 3 nodes (0.3 mm) in width. The planar wave is then allowed to propagate over the tissue. Some time after the first wave is initiated, a second stimulus is applied. The second stimulus is applied to half the tissue, bisecting the propagation front of the first wave. The second stimulus is a voltage clamp, with all the included tissue clamped to a ‘high’ potential, typically +0 mV for a millisecond. The generated spiral is then allowed to evolve until it self-terminates, the spiral wave tip exits the tissue or until a sufficient amount of time has passed such that the spiral can be classified as ‘persistent’. The time allowed for a wave to be classified as persistent is typically 5 or 10 s.

The spiral wave tip traces are calculated via a standard contour based algorithm, comparing the -60 mV contour line on snapshots of the electrical activity 2.5 ms apart.

2.2.8 Spatial Vulnerability of Cardiac Tissue

The spatial vulnerability (SV) of cardiac tissue is defined as the smallest length of tissue which, when given a stimulus at the threshold level in the wake of a propagating wave, gives rise to at least one ‘figure of eight’ re-entry [111]. A

figure of eight re-entry occurs when the excitation waves from the ends of the test length propagate back through the centre of the length. This results in a pair of contra-rotating spiral waves, one at each end of the test length. The SV is useful for quantifying a mutation or condition's potential for arrhythmogenesis by giving an indication of the size of ectopic focus required to excite the tissue. A small SV indicates that the tissue could be very likely to have arrhythmic episodes.

The sheet model used for the determination of the SVW can vary in size, as the SVW can vary substantially, depending on the electrophysiology being simulated by the cellular models at the nodes, but the smallest used is typically 375 x 375 nodes, with a spatial resolution of 0.1 mm. The sheet is first given one conditioning excitation, initiated by injecting a strip of nodes 3 nodes (0.3 mm) in width with current along one edge of the sheet. The wave is then allowed to propagate through the tissue. When the VW of the tissue is positioned at the centre of the tissue, the test stimulus is delivered. The test stimulus is an area of tissue 20 nodes (2 mm) wide and of variable length. After the test stimulus is delivered, the sheet is observed until figure of eight re-entry is observed, or it is obvious that it will not occur. The protocol is then repeated with a test stimulus area of greater length.

2.3 Results From Simulation Studies

The cardiac simulation toolkit has been used in several simulation studies. Here I present two such studies, representing different aspects of the toolkit. The first is based on an experimental study which determined the existence of a novel ion channel in the human atrium which carries an anion current through the cellular membrane. The second is principally a 2D study, concerning the effects of Atrial Fibrillation induced Electrical Remodelling (AFER) and electrophysiological heterogeneity in a 2D idealization of the right atrium and the sino-atrial node.

2.3.1 Anion Currents In The Human Atrium

In a recent experimental study, Li et al. [112] determined the existence of a novel outwardly rectifying anion current in human atrial myocytes isolated from right atrial appendages taken from patients undergoing coronary bypass surgery. A

Table 2.1: Parameter sets for the anion sensitive current I_{ANION} when carrying NO_3^- and Cl^- ions.

	NO_3^-	Cl^-
g_{ANION}	0.37	0.19
E_{ANION}	-45.64	-45.64
c	0.87	0.94
d	8.4×10^{-4}	2.5×10^{-4}

preliminary computational study has been conducted [112] to investigate the effects of the anion sensitive current, I_{ANION} , on atrial action potentials. However it is still unclear on how this novel current affects intra-atrial excitation conduction. This section aims to investigate in detail the effects of I_{ANION} on atrial action potential, conduction behaviours and the dynamic behaviours of re-entrant spiral waves.

The Li et al. [112] study determined the current carried by this novel ion channel, I_{ANION} , could be modelled by

$$I_{ANION} = g_{ANION} \frac{V - E_{ANION}}{1 - (c \times e^{d \times (V - E_{ANION})})} \quad (2.2)$$

where g_{ANION} is the conductivity of the anion channel, E_{ANION} is the reversal potential of the channel and c and d are constants to describe the behaviour. All other symbols have their usual meanings. They presented two sets of parameters for (2.2) given in table 2.1, which described the current through the channel when carrying a majority of NO_3^- or Cl^- ions.

This simulation study used the parameter set for the anion current carrying Cl^- ions. The effects of the addition of this current to atrial myocyte cells was quantified. In the following paragraphs, ‘control’ is used to denote the original Courtemanche et al. [16] atrial myocyte model and ‘anion’ to denote the Courtemanche et al. model with the addition current described by (2.2) and using the Cl^- parameter set from table 2.1.

Methods

The effect on the behaviour of the cells caused by the anion current was quantified using the simulation library described previously in this chapter for control and

anion cases. As this simulation study was based on the CRN cell, the standard stimulus was 2 ms in duration and 2 nS in magnitude. Unless an alternative protocol is mentioned, all simulations directly followed those described in Section 2.2.

Simulating a single cell, the following measures were quantified: the AP profile, the restitution of APD at 50% repolarization, APDr_{50} , the restitution of APD at 90% of repolarization, APDr_{90} and the Effective Refractory Period restitution, ERPr . The maximal fast sodium activation was quantified at the same time as the APDr_{90} was computed and is the product of the three gates in I_{Na} , as m^3hj . In all the single cell cases, the cell was paced 10 times before the measurement was taken, to allow simulation parameters to settle and to adapt to any changes in pacing rate. Storage of the cellular state was used in all appropriate points in the simulation, to minimise computational time.

Using a 1D strand model the temporal Vulnerability Window to unidirectional conduction block, VW , the Conduction Velocity restitution, CVr and the threshold of excitation were computed. The strand model used was 300 nodes long and had a space step of 0.1 mm. The diffusion coefficient, D , was set to $0.03125 \text{ mm}^2 \text{ ms}^{-1}$ [113]. In all 1D simulations the strand was paced 10 times before measurement was taken. In all simulations this state was then cached and restored as appropriate, as described in the algorithms section of this chapter.

Using a 2D tissue model the lifetime of re-entrant spiral waves was estimated, following the wave-break protocol outlined earlier. The sheet had dimensions of 375×375 nodes and a space step of 0.1 mm. The clamp potential used to break the wave was 0 mV and it was applied for 1 ms.

Results

The AP generated by the control and anion simulations are shown in figure 2.3(a). The APD_{90} is slightly reduced from 299.6 ms to 297.3 ms, whereas the APD_{50} is more significantly reduced, from 180.1 ms to 158.1 ms. The AP profile shows a depressed plateau region (phase 2), reduced from -9.56 mV to -14.1 mV and a slightly elevated resting potential, -79.0 mV in the anion case cf. -80.9 mV in control. This is consistent with the Li et al. [112] study, and is included here only for completeness.

Transients of the d and f gate of the $I_{\text{Ca,L}}$ open fractions are shown in figure 2.3(b). The f gate in the I_{ANION} case has a higher fraction of open channels for longer than the control case. The d gate does not activate as much in the

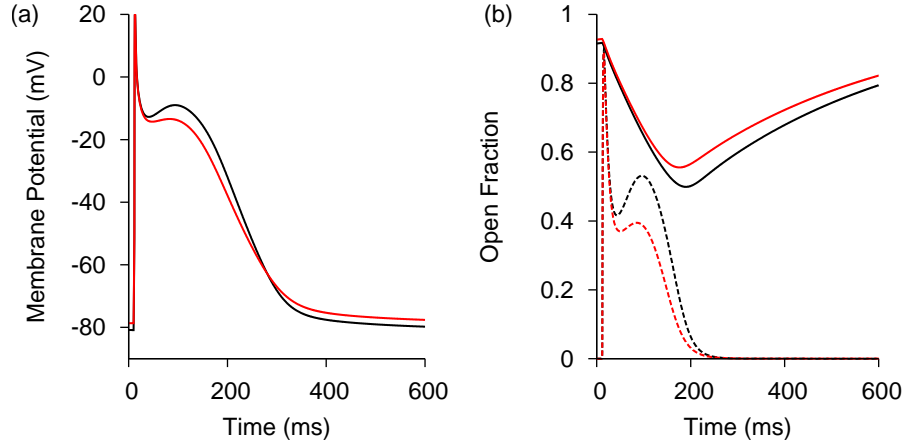


Figure 2.3: (a) AP profile for the CRN model in control (black) and anion (red) cases. The inclusion of the Cl^- carrying current results in a small change of AP morphology, with a depressed plateau potential and an elevated resting potential. (b) Fractional opening of the gates of $I_{\text{Ca,L}}$. The d (activation) gate is shown dashed, the f (inactivation) gate solid. Colours as in panel (a). The f gate takes longer to inactivate, whilst the d gate does not activate as much.

plateau region, contributing to the shorter plateau.

The computed APDr curves under the control and anion conditions are shown in figure 2.4(a) and 2.4(b), for the restitution curves of APD at 50% ($\text{APDr}_{,50}$) and 90% ($\text{APDr}_{,90}$) of repolarization, respectively. The $\text{APDr}_{,50}$ shows the most significant differences, with the anion curve depressed by 20 ms even at the largest DI, increasing to a maximum difference of over 40 ms at a DI of 380 ms. The two curves then cross over at a DI of 200 ms. The $\text{APDr}_{,90}$ curves, by contrast, are very similar for control and anion cases at large (over 600 ms) DI. Between

Table 2.2: Various calculated parameters for control (original CRN cell) and anion (CRN cell modified to include Cl^- -carrying current). The duration of the action potential at 50% and 90% repolarization, APD_{50} and APD_{90} respectively. The maximum observed upstroke velocity of the action potential, $\frac{dV}{dt}_{max}$. The temporal vulnerability window to unidirectional conduction block, VW.

Case	APD_{90} (ms)	APD_{50} (ms)	$\frac{dV}{dt}_{max}$ (mV ms $^{-1}$)	VW (ms)
Control	299.6	180.1	217.1	3.22
Anion	297.3	158.1	210.6	3.94

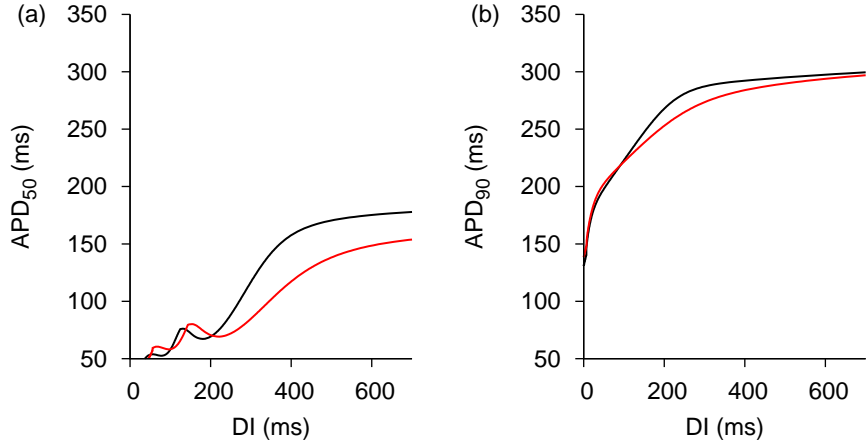


Figure 2.4: (a) $\text{APDr}_{,50}$ curves for the CRN model in control (black) and anion (red) cases. The two variants are different for all the DI in the simulation, with the anion case below the control case for much of the DIs. The slope is reduced by I_{ANION} , compared to the control case. The curves cross at DI 200 ms. (b) $\text{APDr}_{,90}$ curves for the CRN model in control and anion cases. The two variants behave the same at large DIs, but at decreasing DI the anion case shows a greater reduction in the APD_{90} . At short DI (below 100 ms) the two curves rejoin each other.

100–400 ms DI, the anion case is depressed compared to the control case, with a difference of up to 25 ms observed in the measured APDs. At 100 ms, the curves rejoin one another and show a rapidly increasing slope as the DI approaches 0 ms.

The ERP_r curves produced by the control and anion cases are shown in figure 2.5(a). In both cases the ERP_r curves are relatively flat, decreasing by approximately 60 ms over the 700 ms range of S1 intervals considered. The addition of the I_{ANION} current changes the behaviour of the ERP_r curve in a manner which is not simply a shift left or right. The control case shows a response which has a clear plateau region which continues until an S1 interval of 500 ms is reached and then a relatively steeper decline until eliciting an AP of the appropriate magnitude becomes impossible at an S1 interval of 330 ms. The anion case, by contrast, shows a decreasing ERP over the whole range of S1 intervals considered although it too shows its steepest slope just before eliciting a sufficiently large AP becomes impossible, also at approximately 330 ms. At long S1 intervals (above 700 ms) the ERP_r is longer for the anion case before the curves cross at 600 ms and then again at 450 ms with the ERP in anion at the point where further stimulation becomes impossible almost 20 ms higher than in the control case.

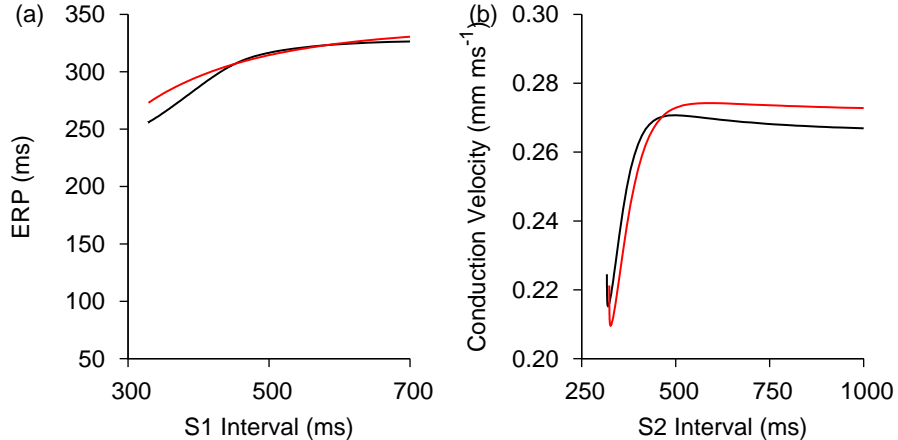


Figure 2.5: (a) ERP_r curves for the CRN model in control (black) and anion (red) cases. The addition of the I_{ANION} current changes the behaviour of the cell from a long and flat plateau region followed by a relatively sharp decrease into a more constant decline. (b) CV_r curves for the CRN model in control and anion cases. The CV_r curves are relatively flat for both cases over the range of 500–1000 ms, before they decrease rapidly in CV until the minimum S2 interval is reached at approximately 320 ms. The CV is higher for the anion case at longer S2 intervals, before it falls below control at an approximate S2 interval of 460 ms.

The temporal VW increased with the addition of the anion current from 3.22 ms in control to 3.94 ms in anion case, a 22% increase in the size of the region of unidirectional conduction block, shown in table 2.2. The CV_r curves, shown in figure 2.5(b), suggest that tissue with the anion sensitive current shows faster CV at normal physiological stimulus intervals (corresponding to 500–1000 ms). The average conduction velocity with I_{ANION} is 0.274 mm ms^{-1} in anion, compared with 0.268 mm ms^{-1} in control in this range of S2 intervals. As the conduction interval is reduced below 500 ms, the conduction velocity starts to decrease rapidly until conduction stops at 323.4 ms for anion and 317.1 ms for control. There is a brief recovery of conduction velocity visible in both cases, just before conduction block.

The threshold of excitation, shown in figure 2.6(a), shows that I_{ANION} reduces the minimum stimulus current by approximately 0.2 nS, a reduction of 10%, at almost all Δt intervals. It is also interesting to note that both control and anion tissue types show ‘supra-normal’ excitability, with the minimum stimulus current decreasing as Δt decreases. This occurs until a critical point is reached when the cell suddenly becomes significantly harder to excite, with the minimum stimulus

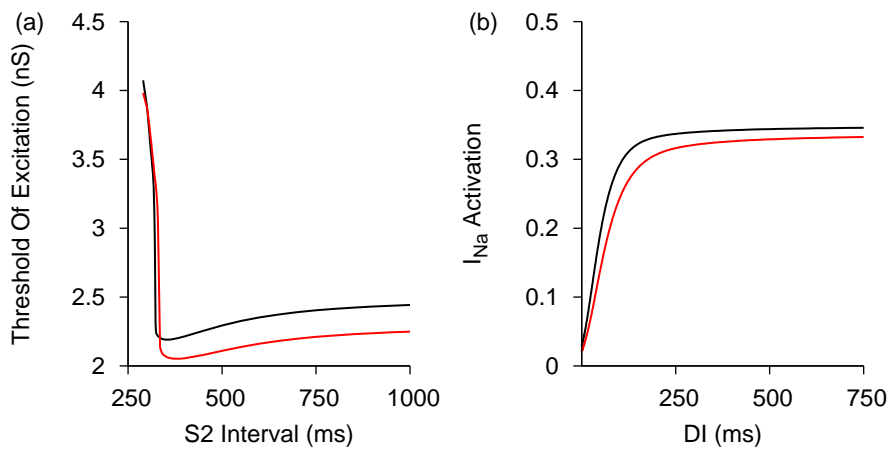


Figure 2.6: (a) Threshold of excitation curves in control (black) and anion (red) cases. As S2 decreases, so does the threshold of excitation until a critical point is reached and the current which must be injected to reach the threshold almost doubles. In the control this comes at a Δt of 321 ms and in anion at 330 ms. Until the critical point threshold of excitation is consistently lower for cells with I_{ANION} present. (b) Maximal activation of the fast sodium current, I_{Na} , as DI is decreased. The fast sodium current consistently activates to a greater degree in control cases. The effect is rate dependent with the greatest difference observed at DI 150–200 ms.

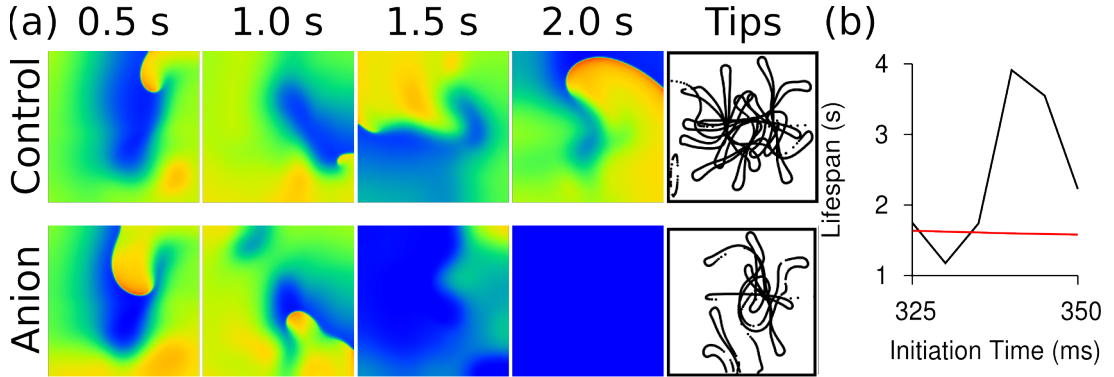


Figure 2.7: (a) Representative membrane potentials and tip trace for control (top row) and anion sensitive cases (bottom row). Times are from the initiation of spiral activity via cross-field protocol. Cross-field stimulus was delivered at 345 ms wall time. Colour represents membrane potential and is coloured from blue (depolarised, -80 mV) to orange (excited, $> 0\text{ mV}$). Both spiral waves are highly mobile, meandering over a very large area of tissue. (b) Lifespan as related to time of initiation. Lifespan in I_{ANION} is relatively constant at around 1600 ms whilst control lifespan fluctuates considerably.

current increasing almost 100%. This occurs 9 ms later in control tissue at 321 ms compared with 330 ms in control.

The maximal activation of the fast sodium current, I_{Na} , is shown in figure 2.6(b). The presence of I_{ANION} consistently reduces the maximal activation of I_{Na} . At long DI, greater than 400 ms, the reduction is 3%, increasing to almost twice that in the range of 150–200 ms. Both curves rapidly decrease to almost no I_{Na} activation at an DI of 0 ms but the anion case starts this descent first. Spiral waves were induced in a square sheet. Representative plots of the membrane potential over the whole sheet, produced as the simulation was ongoing, are shown in figure 2.7(a). The top row corresponds to control tissue, whilst the bottom row has an I_{ANION} sensitive current active. Times of the membrane potential snapshots are relative to initiation of reentry at $t = 345\text{ ms}$. Tip traces are in the 5th column. In both cases the spiral wave starts in the centre of the tissue and then follows a looping track around the tissue before finally it exits the tissue when it cannot turn fast enough around its own refractory tail. Lifespans of reentry from differing initiation times are shown in 2.7(b). Lifespan in I_{ANION} is relatively constant at around 1600 ms whilst control lifespan fluctuates considerably, from 1175 ms to 3910 ms.

Discussions and Conclusions

The effects of the inclusion of an anion sensitive current do not seem to be that large, at least when considered on the single cell level. However, despite the small influence of the current on the action potential duration, it does have significant effects on the restitution properties of the cell and on the behaviour of cells in a tissue. The general behaviours of the Courtemanche cell have been discussed elsewhere, for example in [16,114], I only discuss the differences the I_{ANION} current makes.

The most noticeable effect of the inclusion of I_{ANION} in a cellular model is the abbreviation of the APD_{50} and an accompanying reduction in the plateau potential. The abbreviation is due to I_{ANION} acting as a rectifying current when the membrane potential is above -45 mV . Conversely, at potentials below -45 mV I_{ANION} acts to depolarize the cell, leading to the slightly elevated resting membrane potential observed between action potentials. This difference in effect is what leads to the interesting behaviours observed in cells with I_{ANION} .

The $\text{APDr},50$ and $\text{APDr},90$ curves show that I_{ANION} has a rate dependent effect. Both curves are flattened in the cells which include I_{ANION} but this flattening is not uniform over the range of DIs considered. I_{ANION} has a simple exponential dependence on the membrane potential and no time-dependent gating variables however, so it is not I_{ANION} that causes this rate dependence directly. Instead, we must look to the currents active within the plateau region of the action potential. I_{CaL} is the principle current responsible for the plateau region of the action potential and unlike I_{ANION} it has both time and voltage dependant gating variables for activation, d , and inactivation, f . The d gate is not as interesting as the f gate, as its time-course is not affected by the presence of I_{ANION} , although its activation during the plateau region is reduced. However, the f gate in I_{ANION} cells never inactivates as completely as it does in the control simulations which lack the current.

For the 1D strand results, both the CVr and threshold of excitation data also show rate dependent influence. At a long stimulus interval, the increased excitability of the cell by the anion current leads to a higher conduction velocity [115]. The increased excitability at long stimulus interval is due to the inward nature of the anion current in the very first stages of the action potential. This increased excitability allows atrial cells with I_{ANION} to conduct the excitation wave faster until, when the stimulus interval reaches a critical value of 500 ms,

control cells start to conduct faster. At this stimulus interval, the threshold of excitation is still lower for the anion case, so another factor is responsible for the reduction in conduction velocity. The excitability of the cell is an important influence on the conduction velocity, but it is not the only factor. Another major factor is the upstroke velocity of the action potential which is principally determined by the fast sodium current, I_{Na} . This is partially inactivated by the elevated resting potential in the anion case, which also reduces the rate of recovery of the inactivation variables. When the test stimulus is delivered after a reduced conduction interval in the anion case I_{Na} does not open as fully, slowing the upstroke and thus leading to a reduced conduction velocity at short stimulus intervals, compared with the control case.

The increase in the vulnerability window appears to be quite significant, at over 20% larger than the vulnerability window in tissue without I_{ANION} . An increased vulnerability window has an obvious influence on the genesis of re-entrant excitation—A larger vulnerability window increases the chance of a premature excitation interrupting the normal function of the heart. Though in both cases, the vulnerability window is relatively small.

Dynamic behaviours of the 2D spiral wave are interesting. Both cells show a highly mobile spiral tip, due to their long APD_{90} and ERP relative to the size of the tissue. However in the I_{ANION} case, this does not translate into a widely varying spiral lifespan, as might be expected from such mobility. The restitution properties are generally slightly flattened by the inclusion of I_{ANION} , although perhaps importantly here, in the rapid pacing region, the ERP is higher for I_{ANION} bearing cells. Further investigation, perhaps using the phase field method [116] to start with a ‘stationary’ spiral would be of use to elucidate the effects.

2.3.2 Atrial Fibrillation Induced Remodelling And Heterogeneity

The human atria consists of several tissue types each with distinct electrophysiological properties. It has previously been shown that inhomogeneity in tissues can lead to re-entrant activity [108, 117, 118]. There is also experimental data available on the ion channel remodelling due to atrial fibrillation induced remodelling (AFER) during chronic atrial fibrillation (AF) on human atrial cells [102, 119].

Table 2.3: Parameter modifications to the unmodified CRN model to account for the electrophysiological remodelling of atrial myocytes. Two sets of parameter modifications are provided, to account for the experimental data collected by Bosch et al. [119] and Workman et al. [102]. When percentages are given, they are up or down regulations compared to the magnitude of the current in the unmodified CRN model. The data from Bosch et al. also included at -16 mV shift in the steady state activation of I_{to} and a $+1.6\text{ mV}$ shift in the steady state activation of I_{Na} .

Current	Bosch	Workman
I_{K1}	+235%	+90%
$I_{\text{Ca,L}}$	-74%	-64%
I_{to}	-85%	-65%
I_{Kur}	—	+12%
I_{NaK}	—	-12%
τ_{fCa}	+62%	—

In this study changes in electrophysiological behaviour in cell and 1D homogeneous models under AFER compared to control conditions were quantified. Further, re-entrant waves in 2D electrically homogeneous and electrically heterogeneous sheets were studied.

Methods

The human atrial action potential (AP) model by Courtemanche et al. [16] was used in this study. Modifications were incorporated to reproduce the differing APs of the different atrial cell types [120]. This produced distinct APs for the crista terminalis (CT), pectinate muscles (PM), atrio-ventricular ring bundle and the Bachmann bundle. Atrial myocyte (AM) cells were modelled by the original CRN model.

The data for AFER were taken from experiments by Bosch et al. [119] and Workman et al. [102], representing the changes in ion channels in patients after one month (Bosch) and up to six months (Workman) of chronic AF, respectively. The modifications to the cellular electrophysiology were described in Kharche et al. [121] and reproduced in table 2.3.

The effects of AFER were quantified through a variety of measures. The

APDr_{90} was calculated as described previously. There were 10 S1 stimuli at a frequency of 1 Hz, followed by a varying DI. The ERP_r was calculated as described previously, with 10 S1 delivered at the given pacing rate and then a final S2 stimulus was used to determine the ERP after Workman et al. [102]. The VW and the CV_r were determined for control, Bosch and Workman conditions, for each of the three atrial cell types considered. There were therefore nine 1D strand models tested. The strand models were each 200 nodes long, with a spatial resolution of 0.1 mm. The diffusion constant used for all simulations was set to $0.03125 \text{ mm}^2 \text{ ms}^{-1}$ [113], giving a solitary wave conduction velocity of 0.267 mm ms^{-1} in control atrial tissue. In all 1D strand simulations there was 1 S1 pulse and one S2 pulse. This pulse was applied over 4 nodes (0.4 mm), had duration 2 ms and magnitude 4 nS. The higher stimulus strength was necessary to excite the AFER remodelled tissue.

Further, a 2D electrically heterogeneous sheet model was developed based on a laboratory photograph of the right atrium. The photograph was digitized at a spatial resolution of 0.1 mm. The model developed by segmenting areas of the tissue into AM, PM and CT tissue types. The complete model had an approximate size of 130×100 mm and consisted of approximately 1 million active cell nodes. The simulations were performed with all cells under control, Bosch and Workman conditions, with the conditions applied uniformly to the tissue. All 2D sheet simulations were performed with the space step of 0.1 mm and a time step of 0.05 ms.

Results

Simulations were performed for all three cases: control, Bosch and Workman. However the results for Bosch and Workman were qualitatively similar, although Bosch showed a much more profound effect on APD_{90} reduction.

Incorporating the heterogeneity and AFER data causes significant differences in APD_{90} and AP morphology to manifest, as shown in figure 2.8(a). The effects of AFER are not uniform across the different cell types of the atrium in both cases (figure 2.8(b)). The difference in the AP between AM/PM myocytes and CT myocytes in the Workman remodelled case is almost double that seen in either the Bosch remodelled case or control case. Note that in all cases there is almost no difference between AM and PM types.

The APDr_{90} curves, shown in figure 2.9(a), are flatter over much of the range

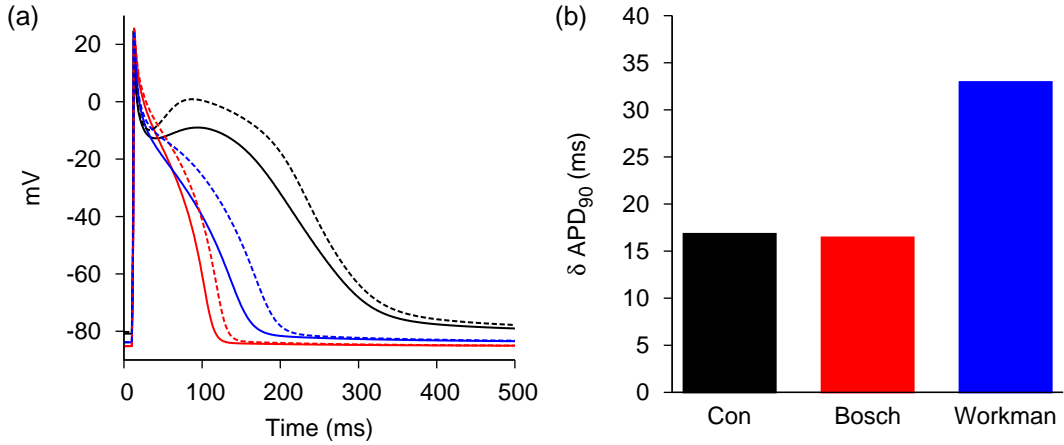


Figure 2.8: (a). Action potential profiles after pacing at 1 Hz. Results are shown for AM/PM cells (solid lines) and CT cells (dashed lines). Control parameter traces are black, Bosch are red and Workman traces blue. The CT cells have a longer APD in all cases and show an elevated plateau potential. (b). APD differences between AM/PM cells and CT cells after pacing at 1 Hz. Colour scheme as for panel (a). There is almost no difference in δAPD_{90} between control and Bosch CT cells, but δAPD_{90} increased markedly when Workman parameters are used.

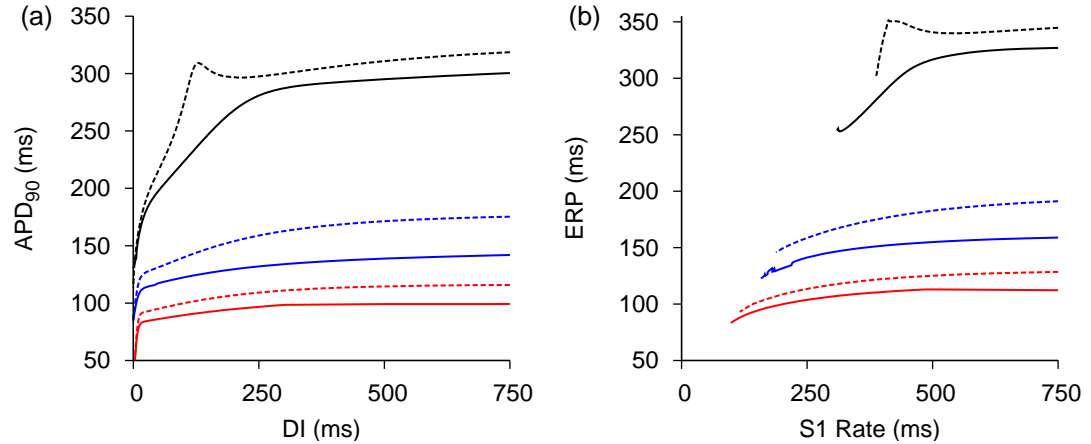


Figure 2.9: (a) APDr,90 curves showing APD₉₀ plotted against diastolic interval (DI) for control (black), Bosch (red) and Workman (blue) cases. AP/PM curves are shown as solid lines, CT curves are dashed. AFER acts to flatten the restitution curves. In all cases CT APD₉₀ is above AM/PM APD₉₀. (b) ERPr curves showing ERP plotted against S1 interval. Colour scheme is as for panel (a). In all cases CT ERP is above AM/PM ERP. Note that AFER enables successful excitation at much lower S1 intervals.

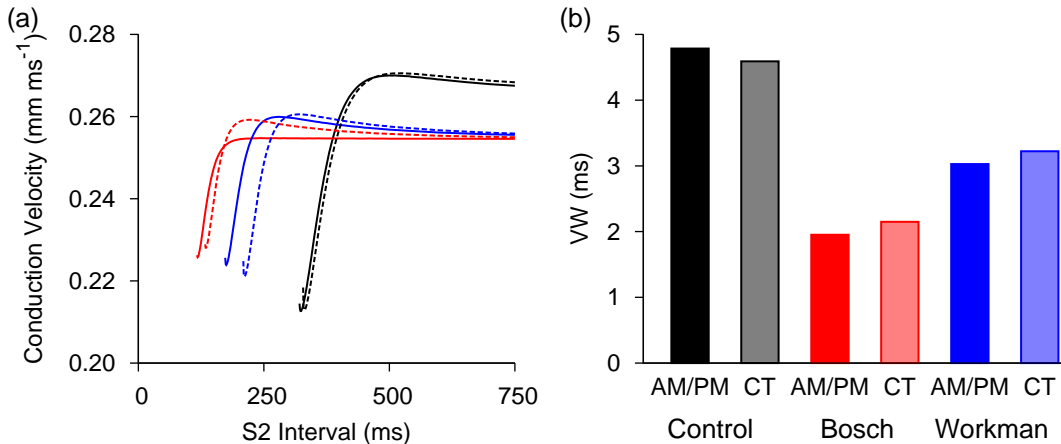


Figure 2.10: (a) CV_r curves for Control (black), Bosch (red) and Workman (blue) tissues. AM/PM cells are indicated by solid lines, CT cells by dashed. In all cases CT cells show a higher conduction velocity at long (>600 ms) S2 intervals, but AM/PM muscles allow faster conduction at lower S2 intervals. AF cases show a reduced CV in all instances and support higher pacing rates via reduced minimal interval. (b) Vulnerability Window for Control (black), Bosch (red) and Workman (blue). AM/PM cell types are shown solid, CT are partially shaded. The VW is reduced for the AF remodeled cases via reduced excitability. The presence of the remodelling also reverses the difference in VW between cell types.

of diastolic intervals for Bosch and Workman as compared to control. The curves have two clear phases in the AFER cases; a very steep initial rise and then slower, asymptotic rise in APD₉₀. In the control case the curves show an intermediate phase with a slope between the two extremes. In the control CT case, the curves include a prominent notch at a DI of approximately 130 ms which is caused by the up regulation of $I_{\text{Ca},L}$ in CT cells. The down regulation associated with the AFER removes this. In both of the AFER cases, the curves are almost flat at DI 750 ms, but in the control case, the APD₉₀ is still rising. The figure also emphasises the increased heterogeneity observed in the Workman case.

In AF tissue, the ERPr was flattened for all tissue types compared with the control cells, as shown in figure 2.9(b). The curves also extended to lower S1 intervals for AF tissue, indicating that it was possible to excite AF tissue successfully at a higher rate than was possible in control tissue. Heterogeneity in ERPr was largely unaffected by AF.

Conduction velocity, shown in figure 2.10(a), was slowed by AF, reducing the solitary wave velocity from 0.27 mm ms^{-1} in control to 0.25 mm ms^{-1} in Bosch and 0.26 mm ms^{-1} in Workman. Maximal pacing rate increased from the control

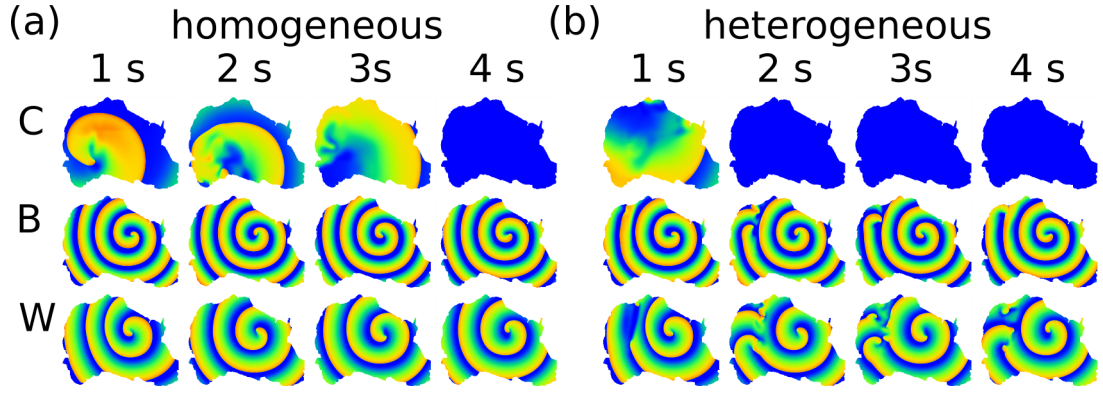


Figure 2.11: Simulation of re-entry in 2D sheets of electrically homogeneous (a) and electrically heterogeneous (b) sheets. Colour represents membrane potential from blue (resting) to orange (excited). Columns show representative frames after initiation of re-entry at $t = 0$. Rows C, B, W show data from control, Bosch and Workman cases, respectively. Re-entry self-terminated under control conditions in both homogeneous (a)(C) and heterogeneous (a)(C). Under AF conditions, re-entry becomes a sustained mother rotor in electrically homogeneous conditions ((a)(B), (a)(W)). However, under electrically heterogeneous conditions AF causes re-entry to degenerate into erratic propagations on the borders of the heterogeneity ((b)(B), (b)(W))

value of 187 bpm to 512 bpm in Bosch strands and 347 bpm in Workman strands of AM or PM cells. In CT strands, maximal pacing rates of 183 bpm, 451 bpm and 287 bpm were observed for Control, Bosch and Workman cases respectively. The heterogeneity of minimal pacing intervals is significantly increased by AFER, from 4 bpm to over 50 bpm in Bosch and Workman strands.

The VW was reduced by AF, figure 2.10(b). The control value of 4.8 ms was reduced to 2.0 ms in Bosch and 3.0 ms in Workman for AM and PM cell types. In CT cells under control conditions, the VW was reduced to ms The reduction in VW for CT cells was reduced, to 4.6 ms. In contrast, the VW increased for AF cases; 2.1 ms and 3.2 ms for Bosch and Workman cases respectively.

Simulations over the 2D geometry examined the lifetime and behaviour of spiral waves in the presence and absence of electrical heterogeneity. As can be seen in figure 2.11, panels (a)(C) and (b)(C), re-entrant activity self-terminated in both homogeneous and heterogeneous cases. Spiral wave meander over a large region of tissue eventually causes the tip to leave the tissue. Self-termination was much more rapid in the electrically heterogeneous case, taking 1.31 s, compared with 3.20 s in the homogeneous case.

Conversely, under AF conditions the re-entry persisted after it was induced for the whole period of the simulation, a lifespan of over 5 s. Under electrically homogeneous conditions, panels (a)(B) and (a)(W) show a stable mother rotor rotating anti-clockwise in the tissue. In heterogeneous conditions, as shown in panels (b)(B) and (b)(W), a similar mother rotor to the homogeneous cases is visible towards the right of each frame. On the left of the frames, the rotor breaks up into multiple fibrillatory wavelets on the border of the heterogeneous regions, forming a complex and chaotic pattern of excitation.

Discussion and conclusions

AFER induces significant changes in the cellular electrophysiology that appear to affect rate dependent electrical activities. It helps to sustain re-entry, providing evidence to substantiate the hypothesis of ‘AF begets AF’.

The single cell results show a striking reduction in the APD₉₀ and repolarization properties. AFER abbreviated APD₉₀ in AM cells by 66 % in Bosch and 53 % in Workman. Other work [95, 122–124] has already suggested why flattening of the ERP and APD restitution curves can be pro-arrhythmogenic. Our study suggested that reduction is not uniform across all cell types, which leads to an augmented heterogeneity.

From the 1D results, AFER tissue forms a much better substrate for arrhythmic activity. It supports a much higher pacing rate and has a reduced conduction wavelength (conduction velocity multiplied by APD₉₀), allowing a greater number of excitation waves to exist in the tissue. The increase in the heterogeneity of the maximal pacing rates suggests that remodelled tissues might be more vulnerable to localised regions of conduction block. This has been shown to lead to re-entry [125].

The 2D simulations in the realistic sheet show a marked difference in re-entrant behavior between homogeneous and heterogeneous simulations. The homogeneous sheets show self-termination of re-entry in control tissue, whilst the reduced ERP and conduction wavelength allow the rotor to remain stable and persist for the duration of the simulation in AFER conditions as is expected from the flattened restitution curves [95, 123]. The heterogeneous sheet simulations, show spiral wave breakup, as observed in real tissue [108], in both control and AF simulations, possibly due to elevated plateau potentials and increased refractory period of the CT cells [110], combined with the slower conduction velocity at high

pacing rates. Self-termination is still observed in control simulations and is more rapid than in homogeneous tissue.

It is still unclear about the pro- or anti-arrhythmogenic effects of electrical heterogeneity in the human atria. Self-termination is more rapid in the heterogeneous tissue for the control case, but despite AFER increasing the heterogeneity between tissue types, it doesn't lead to self termination of the re-entry. In fact, it leads to breakup of the spiral wave in the region of the heterogeneity, leading to a region of erratic propagations, as has been seen in experiment [108]. Further study, in both 3D geometries and physiological experiments, would be needed to elucidate the true effects of the heterogeneity.

2.4 Discussion and Conclusions

A cardiac simulation library has been constructed. This includes implementations of a wide range of experimental protocols used to classify and quantify the influence on electrophysiology of ion channel changes. The library of tools was then used in two electrophysiological studies of atrial tissue.

The cardiac simulation library developed includes experimental protocols used on lone myocyte models, as well as one- and two-dimensional idealisations of tissue. The library of tools is intended to be relatively simple to use and to extend, although it does require knowledge of programming to use to its full potential in its present form. The implementation is intended to be efficient, though without sacrificing biophysical detail in realistic cell models. This is accomplished through the use of adaptive stepping methods to track restitution curves of varying slope, decreasing the gap between data points as it starts to change more rapidly. In addition, state saving is performed to reduce the computation involved in repetitive pre-pacing. Lookup tables of voltage dependent properties can be employed to further cut computational time. The novel use of a very basic computer science algorithm, the binary search, is used to determine critical values in a number of protocols. The use of this algorithm allows parameter estimation to great accuracy from large initial range by successively halving the search space.

Whilst both the binary search and the adaptive step are generally very reliable, they do on occasion fail dramatically. This is often caused by incorrect choice of inputs, which don't allow the algorithm to correctly function, for example, selecting the high and low guesses for the vulnerable window period too late.

There is unfortunately little that can be done in such cases by the toolkit itself. Results might need to be rechecked with a smaller window, centered around the found time.

The toolkit compares well with many existing frameworks. COR has many more cells available for use through the CellML repository and offers an easy way to graph the internal properties of the cell. Like the library developed here, COR is limited to one OS, which is Microsoft Windows for COR. COR has no inbuilt experimental protocols however. CMISS lacks experimental protocols and is hard to script to use automatically. It does offer much more sophisticated visualisation than the toolkit here, and can be used for full 3D simulations too. CARP offers much more powerful interfaces for cardiac modelling, including 3D models. It includes no experimental protocols, although those could probably be implemented using its API. Like this toolkit, CARP does not integrate with CellML.

The computational studies reveal the power of the toolkit and the experimental protocols in assessing the effects of a subtle (I_{ANION}) and large (AFER) remodelling of cellular electrophysiological properties. In the I_{ANION} study, the influence of a novel anion bearing current in the human atrium was examined. Despite the small influence of the current on the APD_{90} and its time independent nature, there were significant alterations in the rate dependant and dynamic behaviours of the cell. This is due to the voltage at which the current act, and the corresponding alterations to the time courses of currents which do have time dependent properties. The AFER study, by contrast, involved remodelling where many currents were affected. In this study, the restitution curves were significantly flattened, leading to stable spiral waves. Regional differences in AP profiles, caused by the natural heterogeneity of the atrium, lead to breakup on the edges of such regions.

Chapter 3

Modelling the Whole Atrium

In the previous chapter a modelling library suitable for simulation of single cell, 1D and 2D cardiac tissue was developed. This library was used to investigate aspects of atrial electrical activity. These models provide valuable insight into the behaviours of cardiac tissue in health and disease. However, these simple models ignore the complex 3D structure of the atria. This complexity can be seen internally, in that the atrium is comprised of several distinctive tissue types with different cellular electrophysiological properties and inter-cellular electrical coupling. It can also be seen in the gross physical structure, the atrium has a complex topology with both holes for the venous and arterial openings, as well as openings for the valves. The simpler, often idealized, models constructed in the previous chapter ignore (and in many cases, are incapable of showing) many of these complexities. To provide insight into the atrium function on the whole organ level one must therefore simulate the atrium as an organ. A 3D model of the atrium requires a representation of the atrial geometry to provide the topology of the atrium. To model complexities with sufficient accuracy models of the electrophysiologically distinct tissue types are also required as are descriptions of the complex conductivities.

3.1 Anatomical Atrial Geometry

The anatomical atrial geometry used in the simulation studies presented here was based on the visible human project female dataset. The visible human dataset was created from a pair of cadavers, set into wax and sliced into 1 mm and 0.33 mm for the male and female bodies, respectively. The geometric model used

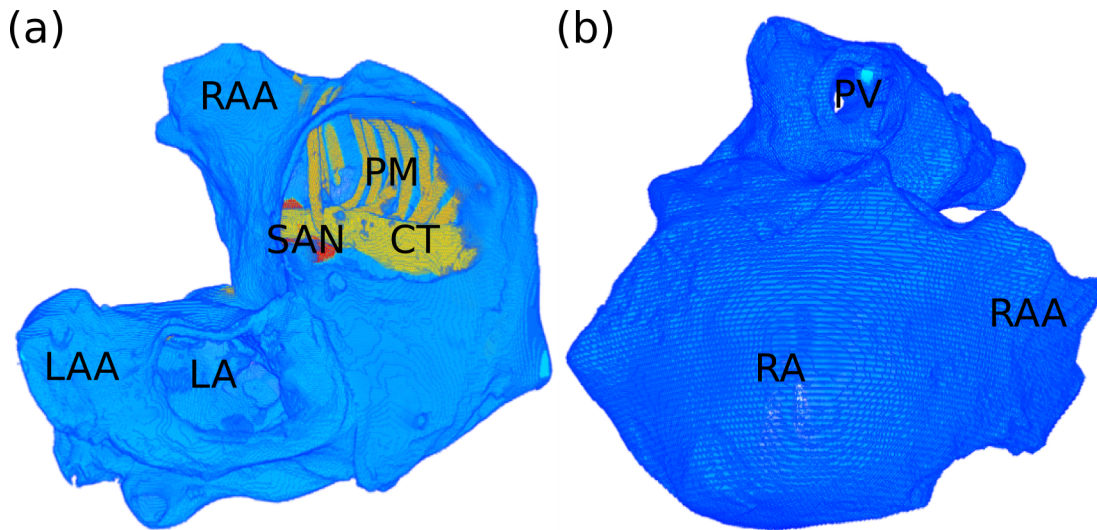


Figure 3.1: (a) View up into the right (RA) and left (LA) atria, showing the pectinate muscles (PM, orange), crista terminalis (CT, yellow) and sino-atrial node (SAN, red). The atrial muscle is shown in blue. Also labelled are the right (RAA) and left (LAA) appendages. (b) A view of the atrial geometry looking down onto the wall of the right atrium. Visible at the top of the panel is the opening for one of the pulmonary veins (PV).

here was extracted from the female dataset and so has a spatial resolution of 0.33 mm. The extracted anatomical geometry is segmented into different tissue types, with distinct classifications for left and right atrium, the pectinate muscles, the crista terminalis, the Bachmann bundle and the sino-atrial node, as shown in figure 3.1. The geometry has been used in numerous previous simulation studies. It was discretised via a finite differences approach, which allows the whole atrium to be embedded in a block of $298 \times 269 \times 235$ nodes. This gives it a size of approximately 19 million nodes, although only approximately 1.6 million of those nodes correspond to atrial cells. The anatomical model also considers fibre orientation in the pectinate muscles, crista terminalis and Bachmann bundle, which always run parallel to the local axis of the tissue bundle, as determined by principle component analysis [120]. Representations of the fibre structure are shown in figure 3.2.

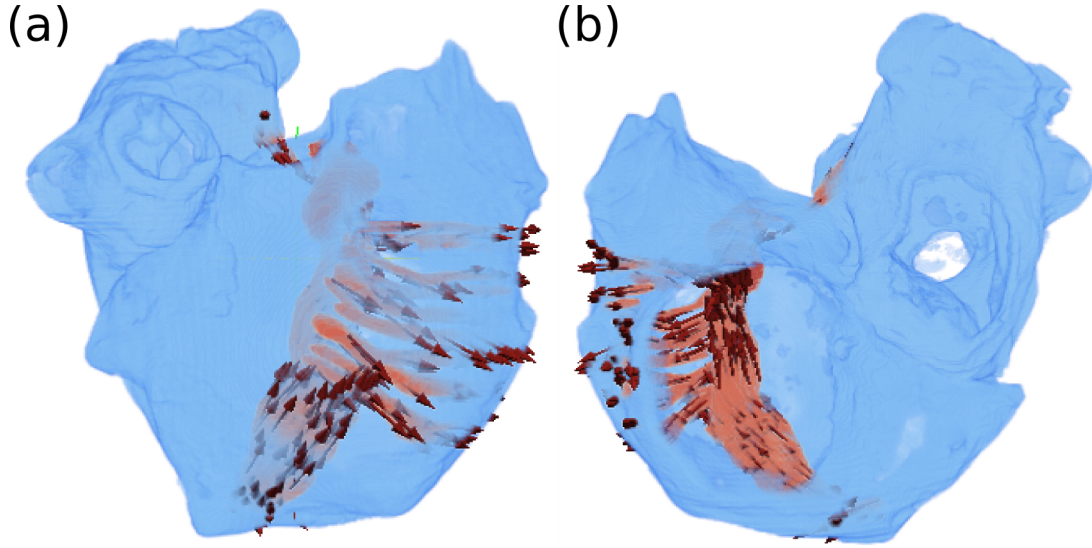


Figure 3.2: Representation of the fibre structure of the atrial geometry from a frontal view (a) and a view up into the atria from the ventricles (b). The arrows in red are aligned along the unit vectors of the fibre orientation. The crista terminalis and the pectinate muscles are very easy to see with their well defined fibre orientation.

3.2 Simulation Methods

3.2.1 Atrial Model

The electrical activity at each of the nodes was described by the equations of the Courtemanche–Ramirez–Nattel (CRN) of the human atrial myocyte [16]. This model, as previously described (§1.2.4), is a second generation model. It has 21 state variables, representing ionic gating activations and inactivations and intracellular concentrations of ionic species. In the model, the total current, I_{ion} is made up of the contributions of numerous ion channels and exchangers.

$$\begin{aligned} I_{\text{ion}} = & I_{\text{Na}} + I_{\text{K1}} + I_{\text{to}} + I_{\text{Kur}} + I_{\text{Ks}} + I_{\text{Kr}} + I_{\text{Ca,L}} \\ & + I_{\text{p,Ca}} + I_{\text{NaK}} + I_{\text{NaCa}} + I_{\text{b,Na}} + I_{\text{b,Ca}} \end{aligned} \quad (3.1)$$

where I_{Na} , I_{K1} , I_{to} , I_{Kur} , I_{Ks} , I_{Kr} , $I_{\text{Ca,L}}$, $I_{\text{p,Ca}}$, $I_{\text{b,Na}}$ and $I_{\text{b,Ca}}$ represent ionic currents and I_{NaK} and I_{NaCa} are ion exchangers. As a second generation model, the CRN model also has a detailed calcium handling system which can influence the action potential via its influence on the intracellular calcium concentration.

Table 3.1: Table showing the parameters altered to differentiate pectinate muscle (PM) and crista terminalis (CT) cells, compared to the normal Courtemanche et al. (CRN) parameters.

	CRN	PM	CT
$g_{\text{to,max}}$	0.1652	0.1652	0.2215
$g_{\text{Ca,L,max}}$	0.1238	0.1238	0.2067
$g_{\text{Kr,max}}$	0.0294	0.0294	0.0294

In some atrial simulations it was desirable to incorporate details of electrophysiological heterogeneity to represent the regional difference in electrical activity of atrial myocytes and the other cellular types present in the geometry, such as the pectinate muscles and crista terminalis. The parameters used for heterogeneity were based on measurements taken by Feng et al. [9] of the canine atrium. These were converted to parameters for the CRN model by Seemann et al. [126] and have been used in several simulation studies [120, 127]. They are shown in table 3.1.

3.2.2 Monodomain Equation

To simulate the propagation of electrical activity over the finite difference geometry previously described, the mono-domain equation (§1.2.5) is used to describe the changes in V in time, t , the trans-membrane voltage.

$$\frac{\partial V}{\partial t} = \nabla \cdot D \nabla V - \frac{I_{\text{ion}}}{C_m} \quad (3.2)$$

where D is a tensor representing the diffusivity of electrical potential, I_{ion} is described by the CRN model (3.1), C_m is the membrane capacitance and all other symbols have their usual meanings. Equation (3.2) is advanced in time via the forward Euler method with a timestep of 0.02 ms. For simulations with isotropic conductivity between nodes a 7-node approximation of the differential operator is used. When anisotropy is present, a 19-node approximation is used.

3.2.3 Tissue Anisotropy

The heart has a complex fibrous structure (Chapter 1), and this manifests electrically as regions which have preferential conduction directions. The preferential conduction directions show greatly increased conduction velocities, sometimes by a factor of up to five. The fibre structure and regions of preferential conduction are generally considered much more important for the ventricles than for the atria. The atria, or more specifically the right atrium, do possess several structures with a definite direction of preferential conduction. These are the crista terminalis, responsible for rapid conduction of the depolarization wave to the atrio-ventricular node, the pectinate muscles and the Bachmann bundle, the preferential pathway for conduction between the atria. To determine the influence of anisotropic conduction on the propagation of the electrical activity, we follow a method after Panfilov and Keener [128]. In this method there is a unit vector, \mathbf{f} , defined at every point in the tissue which has significant fibre orientation. This unit vector defines a set of co-ordinate axes, in which the conductivity tensor is diagonal

$$\tilde{\mathbf{D}} = \begin{pmatrix} D_{\parallel} & 0 & 0 \\ 0 & D_{\perp} & 0 \\ 0 & 0 & D_{\perp} \end{pmatrix} \quad (3.3)$$

where D_{\parallel} is the diffusion constant for conduction parallel to the preferential direction of conduction and D_{\perp} is the diffusion constant for conduction perpendicular to this direction. In this formulation it is assumed that there is no ‘sheet’ structure which gives a higher conduction velocity in one direction perpendicular to the main fibre axis. The diffusion tensor $\tilde{\mathbf{D}}$ will only be diagonal in the Cartesian co-ordinate system of the heart if the direction of preferential conduction is parallel to one of the axes. Therefore, to find the conductivity tensor in the global co-ordinate system, \mathbf{D} , we need to find two transformation matrices \mathbf{A} and \mathbf{A}^T such that

$$\mathbf{D} = \mathbf{A} \tilde{\mathbf{D}} \mathbf{A}^T \quad (3.4)$$

To find \mathbf{A} it is possible to write out the involved rotations explicitly, however an alternative method [129] uses the fact that \mathbf{f} and the two vectors orthogonal to it, \mathbf{g} and \mathbf{h} are eigenvectors of \mathbf{D} . These have the eigenvalues of D_{\parallel} and D_{\perp} . The matrix \mathbf{A} is therefore an orthogonal matrix of the form $\mathbf{A} = (\mathbf{f}, \mathbf{g}, \mathbf{h})$ and so,

using (3.4) \mathbf{D} can be written as

$$\mathbf{D} = D_{\parallel} \mathbf{f} \mathbf{f}^T + D_{\perp} (\mathbf{g} \mathbf{g}^T + \mathbf{h} \mathbf{h}^T) \quad (3.5)$$

Using the fact that $\mathbf{A} \mathbf{A}^T = \mathbf{I}$ it is possible to write

$$\mathbf{D} = D_{\perp} \mathbf{I} + (D_{\parallel} - D_{\perp}) \mathbf{f} \mathbf{f}^T \quad (3.6)$$

where \mathbf{I} is the identity matrix, and all other symbols are as defined previously. The directions of preferential conduction for the atrial geometry used in the study were described by a pair of angles θ and ϕ representing the orientation of the unit vector \mathbf{f} at each point in spherical polar co-ordinates. In cells with no assigned preferential conduction direction, the components of \mathbf{f} were set to zero, giving a diffusion tensor of

$$\mathbf{D} = \begin{pmatrix} D_{\perp} & 0 & 0 \\ 0 & D_{\perp} & 0 \\ 0 & 0 & D_{\perp} \end{pmatrix} \quad (3.7)$$

which is the diffusion tensor for isotropic conduction.

The fibre orientations for the anatomical geometry used in this study are defined in two files. These two files contain the θ and ϕ components of the fibre vectors between 0 and π , discretised in 255 steps. The relationship between the angles θ and ϕ and the unit vector of fibre direction, \mathbf{f} , are shown in figure 3.3. To convert θ and ϕ to the unit vector \mathbf{f} we use [130],

$$f_x = \cos \phi \sin \theta \quad (3.8a)$$

$$f_y = \sin \phi \sin \theta \quad (3.8b)$$

$$f_z = \cos \theta \quad (3.8c)$$

where θ and ϕ are as indicated in figure 3.3 and f_x , f_y , f_z are the x -, y -, z -components of the vector \mathbf{f} .

3.2.4 Computational Implementation

The atrial geometry used in these studies is quite large, consisting of almost 19 million nodes. As noted in 3.1, only approximately 1.6 million of these nodes correspond to active tissue—less than 10% of the total. The electrical activity

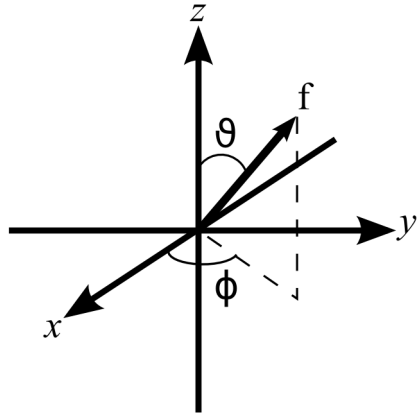


Figure 3.3: The relationship of the angles θ and ϕ with the unit vector of fibre orientation, \mathbf{f} . The angle θ is the angle between the z axis and \mathbf{f} . The angle ϕ is the angle of rotation of \mathbf{f} around the z axis in the x - y plane.

at each node is represented by the CRN model and thus requires 21 double precision numbers to be stored, representing the state variables of the model. The memory requirements of the model may be significantly reduced by storing state variables, and where anisotropy is present the diffusion tensor, only for the active nodes. This reduces the memory requirements for storing the state variables from approximately 2.9 GB to 256 MB. A further simplification may be obtained by decomposing the geometry into a linear array, containing the 6 or 18 neighbours of the active nodes to be used in the diffusion tensor approximation. The geometry and state information can therefore be represented by one linear array of cellular states, one linear array used as a ‘map’ and one linear array representing the components of the Laplacian. This linear data structure is very easy to parallelize on a shared memory system.

The parallelization was accomplished through the use of the OpenMP shared memory parallelism library [88]. The system was then solved on 1 node of the Horace supercomputer on a total of 8 cores. The linear array of active nodes was divided equally between the 8 cores, with each core solving (3.1) for all nodes its assigned section of the array. A snapshot of the trans-membrane potentials at each of the active node sites was output every 1 ms of simulated time. Simulation of 1 s of atrial activity took 3.4 hours.

3.3 Validation of the Model

To verify the model, it was used to simulate a normal propagation, initiated from the sino-atrial node. The fully detailed model was used. The Laplacian was pre-computed to include all the information on tissue anisotropy from the fibre orientation which accompanied the geometry. The bulk diffusivity, D , of the tissue was set to 0.18. The anisotropy ratio for transverse to longitudinal conduction was set to 1:9. The activity at each node was represented by the Courtemanche et al. model with voltage and ion concentration dependent parameters pre-computed and tabulated. A timestep of 0.02 ms was used to integrate both the cellular model at each node and the diffusion of electrical activity between the nodes. To initiate excitation a 2 nA current was delivered for 2 ms to cells corresponding to the sino-atrial node of the model. The excitation was then allowed to propagate without interference. After the propagation was allowed to run its course, activation maps were constructed.

3.3.1 Activation Maps

Snapshots of the electrical excitation are shown in figure 3.4 and figure 3.5. A map of activation times over the whole atria are shown in figure 3.6. Excitation is initiated in the sino-atrial node. The excitation wave is rapidly conducted along the muscle bundles which comprise the crista terminalis and the pectinate muscles towards the base of the atrium and the atrio-ventricular ring. The influence of the preferential conduction along the crista terminalis and pectinate muscle bundles is obvious on the epicardial surface of the right atrium. The presence of the muscle bundles on the endocardial surface causes earlier activation of the epicardial surface. The left atrium is activated first by the Bachmann bundle. After this excitation spreads down and around the left atrial wall to the atrio-ventricular ring and the left atrial appendage. Complete activation of the right and left atria takes approximately 120 ms. After the activation there is an extended plateau phase, which lasts for approximately 100 ms. During this plateau phase the whole atrium has a very uniform potential. Repolarization begins at the sino-atrial node, following a very similar pattern to the spread of excitation, with the region to first depolarise being that which was first excited. The repolarization appears to be less effected by the fibre structure of the atrial model, with repolarized tissue spreading uniformly over the surface of the right atrium.

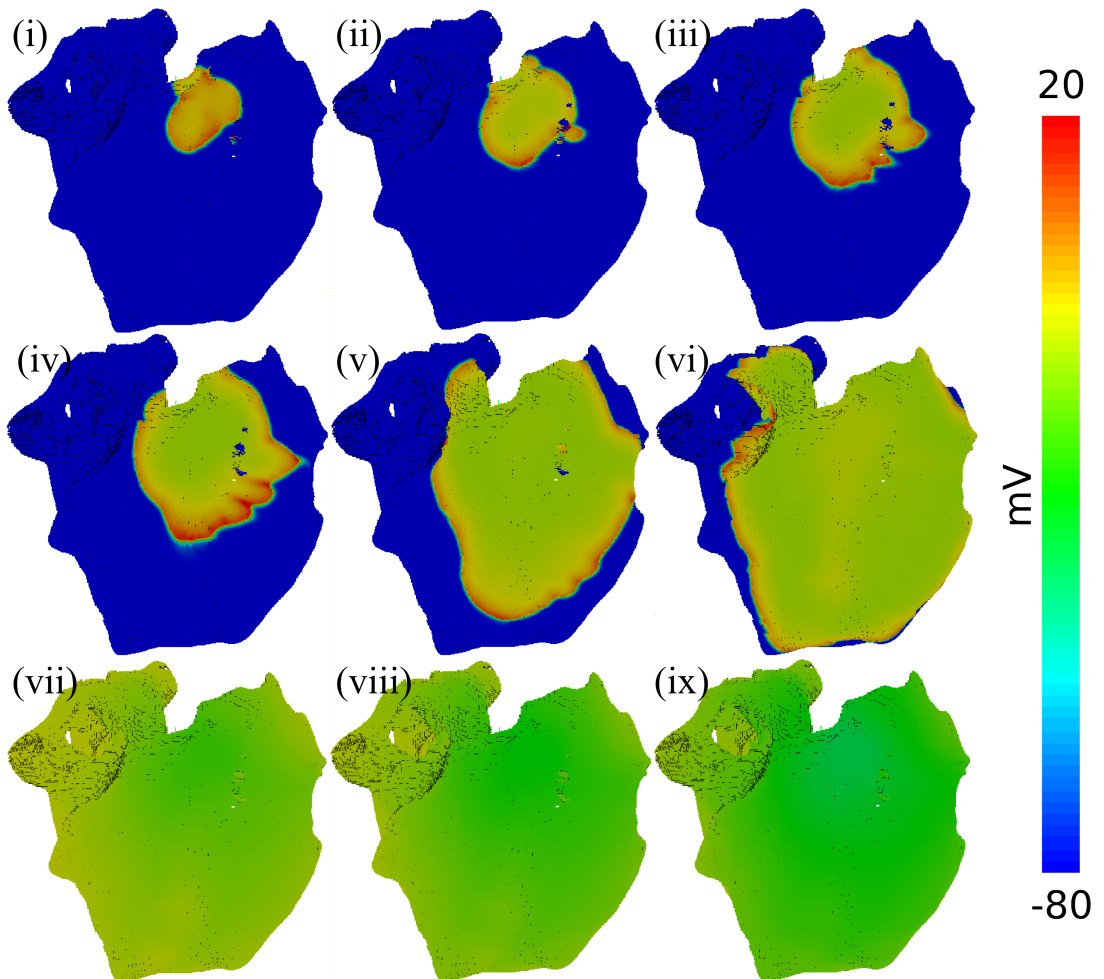


Figure 3.4: Simulated propagation of electrical excitation over the atrial model. Excitation is initiated in the region corresponding to the sinus node. Excitation spreads fastest along the fibres of the crista terminalis and the pectinate muscles. Snapshots shown for 10 ms (i), 15 ms (ii), 20 ms (iii), 25 ms (iv), 40 ms (v), 60 ms (vi), 180 ms (vii), 200 ms (viii) and 220 ms (ix).

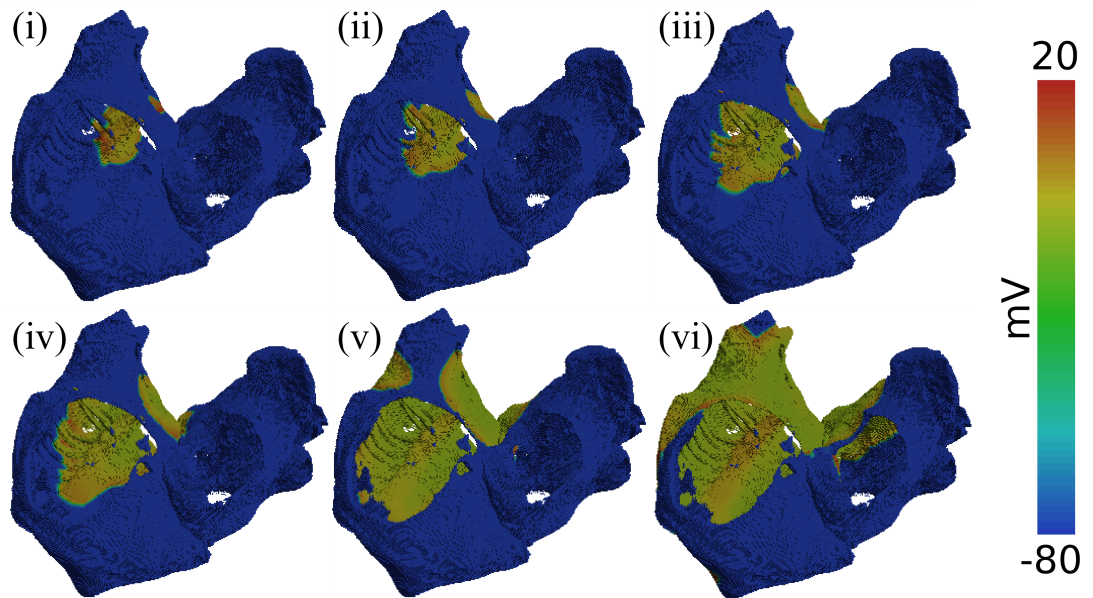


Figure 3.5: Simulated propagation of electrical excitation over the atrial model. Excitation is initiated in the region corresponding to the sinus node. Excitation spreads fastest along the fibres of the crista terminalis and the pectinate muscles. Snapshots shown for 10 ms (i), 15 ms (ii), 20 ms (iii), 25 ms (iv), 40 ms (v), 60 ms (vi).

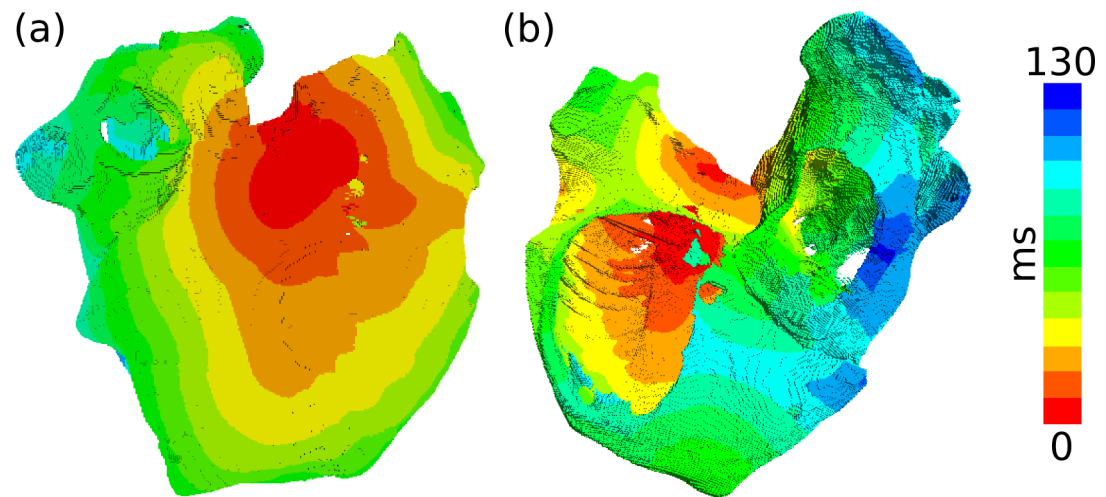


Figure 3.6: Activation times of the atrial geometry from a frontal view (a) and a view from the ventricles up into the atria (b). The influence of fibres on the activation times is clearly visible on both views. Excitation begins and the sinus node and spreads along the fibres over the atrial epi- and endocardial surfaces. The appendages are the last to activate.

Once activated, the whole atrium takes 121 ms to depolarise. Time to depolarisation was taken as the time for a myocyte to attain a potential of -60 mV . The site of first activation of the endocardial surface of the left atrium occurs at 26 ms in the region of the Bachmann's bundle. The time to total depolarisation of the endocardial surface was 95 ms for the right atrium and 94 ms for the left atrium. Conduction velocities were estimated from surface activation time information. Conduction velocities are found to be $1.30 \pm 0.05\text{ ms}^{-1}$ in CT and $0.75 \pm 0.06\text{ ms}^{-1}$ in the atrial wall.

3.3.2 Comparisons with Experimental Studies

In a recent patient study Lemery et al. [131] performed simultaneous recordings of extracellular potentials on the endocardial surfaces of the atria of twenty patients before they underwent catheter ablation therapy. They found the total activation time under sinus rhythm for the endocardial surfaces of both atria was 120 ms. The total activation time for the right and left atria was found to be 81 ms and 80 ms respectively. The time to first activation of the left atrium at the Bachmann's bundle was found to be 41 ms. The results from the simulated propagation are within the range of results measured clinically for all times and within one SD of the mean for all quantities except the left atrial activation time.

Conduction velocities for the classes of tissue present in the model have been measured experimentally from 0.68 ms^{-1} to 1.03 ms^{-1} for atrial wall muscle [132], from 0.7 ms^{-1} to 1.3 ms^{-1} for crista terminalis [133] in the human atrium. Conduction velocity in the pectinate muscles or Bachmann bundle has not been measured experimentally in human studies. The measured conduction velocities are within the experimental limits, providing further confirmation.

3.3.3 Comparisons with Existing Models

There are several existing three dimensional models of conduction in the whole human atrium [120, 134–136] which use some variant of a biophysical model for the atria. Others, such as the cellular automaton approaches [137] are not discussed here. They represent a range of electrophysiological detail, fibre structure and computational complexity. The model of Harrild and Hereniquez [134] has a detailed fibre structure, but this is coupled with homogeneous electrophysiology. In addition, the model has a relatively coarse space step, with an average

inter-element distance of 0.55 mm. The Zemlin [135] model was also based on the visible human dataset. They used a reduced formulation of the Courtemanche et al. model which has 6 variables. They included atrial wall muscle fibres based on dissection of anatomical specimens. There was no internal fibre structure such as the Bachmann bundle however. It is a very efficient model. The Vigmond [136] is an idealised model of an unusual construction. It is topologically, rather than anatomically, correct and formulated as a series of shells, made up of interconnected fibres. The fibre based construction allows for efficient solutions. The Seemann [120] model is closely related to the model proposed in this chapter—it would be accurate to say that this model is a simplification or refinement of the Seemann model. The Seemann et al. model features an autoactive sino-atrial node complex, while the model here focuses on the atrial conduction only. It uses a full formulation of the Courtemanche et al model, without lookup tables. It features regions of differing bulk conductivity. It is much more computationally demanding than the model proposed in this chapter.

The model of the whole atrium proposed in this chapter represents a compromise between electrophysiological detail and computational efficiency. It includes differential electrophysiology and fibre orientation. The omission of a functioning sino-atrial node is not a large flaw—many pathological simulations involve non-physiological pacing protocols. The additional incorporation of an MPI, rather than OpenMP, based implementation would allow much more distributed execution, allowing long term simulations to be performed.

3.4 Mutation in KCNQ1: A Simulation Study

Atrial Fibrillation (AF) is the most common arrhythmia in the developed world. It is a self-promoting condition, with paroxysmal AF episodes frequently degenerating into chronic and even permanent AF. Clinically, AF patients show an erratic and high frequency ECG. At the cellular level, AF is characterised by an abbreviated action potential (AP) which has no plateau phase and poor heart rate adaptability. The mechanisms through which AF influences the heart are complex, but the remodelling of the cellular electrophysiology is believed to contribute to reduced ERPs and through that, favour the formation of stable, long lived spiral waves and organ level microwavelet re-entry. AF is often preceded by congestive heart failure, cardiomegaly and other structural cardiac diseases, but

there are significant numbers of suffers with no such structural defects. There is also evidence of a genetic predisposition to AF, which is sometimes termed Familial Atrial Fibrillation. Several gene mutations have been causally implicated for AF, leading to AF which manifests both with and without associated structural cardiac disorders. The ion channels associated with the repolarization reserve (I_{K1} , I_{Kr} , I_{Ks}) are particularly important to the genesis of AF. Alterations in functions, gating and kinetics have been implicated in both short and long QT syndromes. The I_{Ks} channel has very slow activation kinetics which enable it to regulate cardiac APs over a wide range of plateau voltages. Mutations in the I_{Ks} channel are common. Several mutations in the α -subunit, coded for by the KCNQ1 gene, of the I_{Ks} channel have been identified including both loss-of-function and gain-of-function, leading to the SQT syndrome and to AF. Chen et al. studied a four generation Chinese family with hereditary persistent AF. They identified a missense mutation at nucleotide 418 from adenine to guanine resulting in a change from serine to glycine at position 140 (S140G mutation of I_{Ks}). This missense mutation lead to a large gain-of-function which included changes in the channel kinetics. It has been hypothesised that these changes in the function of the I_{Ks} channel in the human atrium result in abbreviations of both APD and ERP and thus provide an appropriate substrate for the genesis of AF.

This study had two goals: To construct a computer model of the available experimental data from Chen et al. and to then use this model to quantify the effects of the mutation through the use of cellular, 1D, 2D and 3D models

Modelling the Mutation

This study, as in the previous chapter, uses the CRN model, developed by Courtemanche et al. [16] for simulation of the human atrial action potential. As a biophysically detailed model with 21 state variables and numerous ion channels it is ideal for use in mutation studies. The CRN model has individual descriptions of several K^+ currents. These include the time-independent potassium current, I_{K1} , the ultra-rapid potassium current, I_{Kur} , the transient outward current, I_{to} and the rapid and slow delayed rectifier currents, I_{Kr} and I_{Ks} . The latter current is modulated by the mutation and is described in the control CRN cell by

$$I_{Ks} = g_{Ks}x_s^2(V - E_K) \quad (3.9)$$

where g_{Ks} is the channel conductance (0.129 nS/pF), x_s is the activation variable and E_K is the K^+ reversal potential, found through the Nernst potential.

Simulation of the S140G mutation of KCNQ1 I-V relationship

The Chen et al. [138] study determined that the most likely cause of familial AF was the S140G mutation of the KCNQ1 gene, which forms part of the α -subunit of the I_{Ks} channel. The gene was transfected into COS7 cells along with the second component of the α -subunit, KCNE1, in both normal (WT) and mutated type (MT). The transfected cells were used to perform voltage clamp experiments. The clamp protocol used by Chen et al. [138] was as follows: the cell was held at a holding potential of 80 mV for 0.5 s before being held at 10 mV steps between -130 mV to 50 mV for 3 s. The voltage steps were followed by a -40 mV holding potential, applied for 1 s. The values of I_{Ks} at the end of the step voltages were plotted against the step voltages to determine I-V relationships for WT and MT cells, shown in figure 3.7(a) (points with errors) and current traces, shown in figure 3.7(b) and (d) for WT and MT, respectively.

The I-V relationship shows that the mutation causes a gain-of-function across all the clamp potentials. It also reveals that the mutation appears to cause an inward current at negative potentials. The current traces suggest a drastic change in the kinetics of the I_{Ks} channel with a significant component of the current being activated immediately. The addition of a leakage component to (3.9) allowed simulation of I_{Ks} characteristics which closely matched the experimental data. Under MT conditions, the new total current I'_{Ks} was described by

$$I'_{Ks} = I_{Ks} + \varphi g_{Ks} x (V - E_{rev}) \quad (3.10)$$

where I_{Ks} is (3.9), φ is a multiplicative parameter from with values between 0 and 1, g_{Ks} is as in (3.9) and E_{rev} is the reversal potential of the leakage component. The reversal potential was estimated from the experimental I-V relationships to be -76.3 mV. The inclusion of the φ parameter allowed the simulation of several intermediate mutant states, representative of a heterozygous mutation. Setting $\varphi = 1$ and following the voltage clamp protocol the I-V relationship of I_{Ks} was simulated to provide a good match to experimental data, shown as the lines in panel (a) of figure 3.7. Also shown are the simulated current traces elicited by the voltage clamp protocol in panels (c) and (e). The non-gated leakage component of

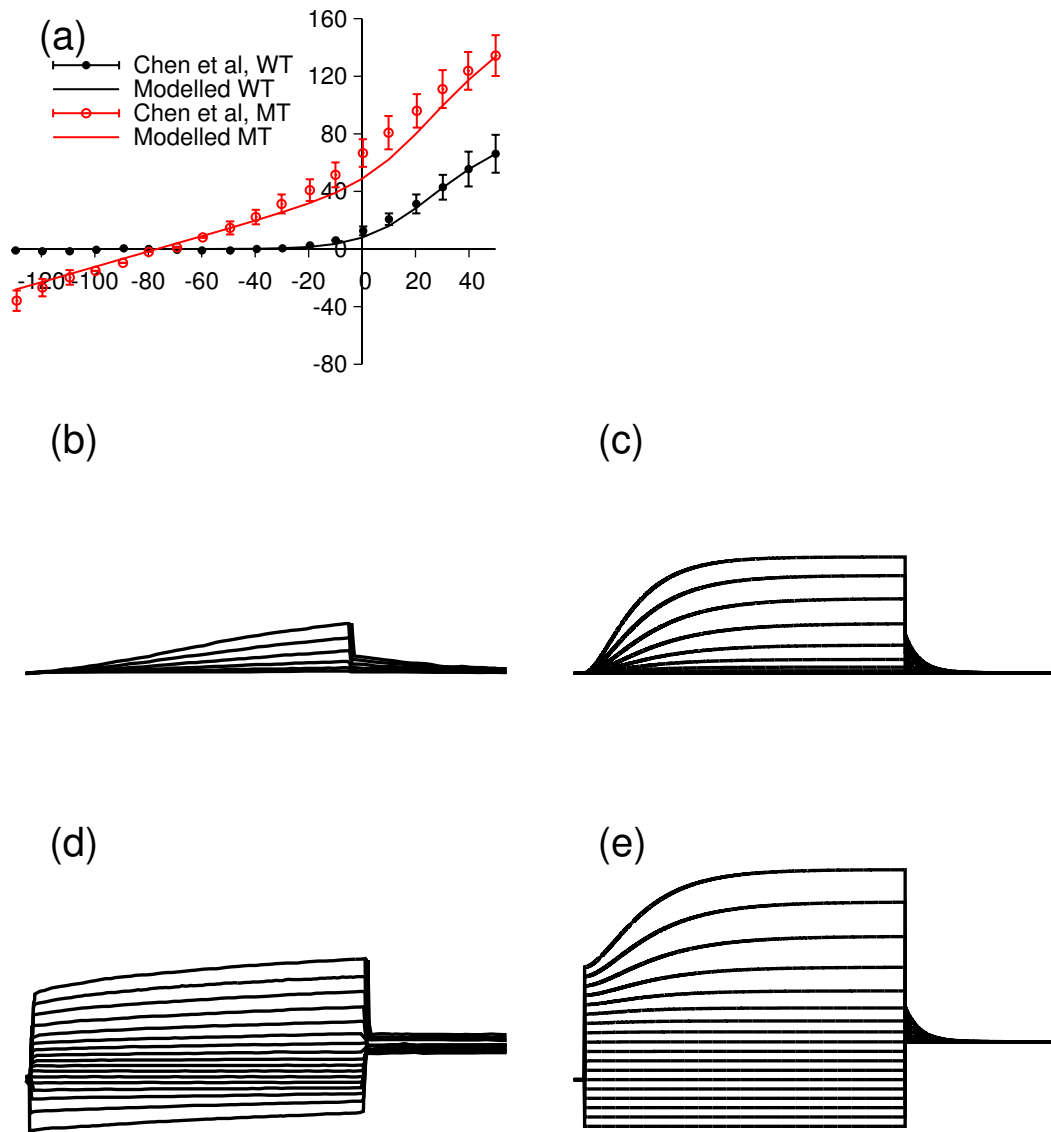


Figure 3.7: (a) Experimental WT (black, closed circles) and MT (red, open circles) I-V relationships recorded by Chen et al [138]. Simulated I-V curves for WT (black lines) and MT (red lines). Modelled curves are scaled to experimental points based on the WT current density at 50 mV. (b) Experimental current traces for WT. (c) Simulated current traces for WT. (d) Experimental current traces for MT. Note the instantaneous activation, and the significant inward current at negative clamp potentials. (e) Simulated current traces for MT.

I'_{Ks} sufficiently accounts for the changed current density and kinetics. Note that in panel (a) the modelled current traces have been normalised by the maximum current observed with a normal I_{Ks} and the WT KCNQ1. The differing time-course of the currents are likely due to the different temperatures at which the simulations were performed. However, no data on the temperature dependence of I_{Ks} was available.

Simulation Protocols

To assess the effects of the mutation on human atrial myocytes, cellular models including the modified I'_{Ks} described by (3.10) were used in a number of simulation protocols, as described in Chapter 2. Initially the APD₉₀ was evaluated under conditions corresponding to $\varphi = 0$ (WT) and $\varphi = 1$ (MT). Under such conditions, the induced APD₉₀ shortening was found to result in un-physiological APD₉₀ values, shown in figure 3.9. Therefore a pair of heterozygous cases, corresponding to $\varphi = 0.10$ (HT10) and $\varphi = 0.25$ (HT25) were created and used in the evaluation of the mutation's effects.

Using the models and protocols described in Chapter 2 the APDr,₉₀, ERPr, VW, CVr, SVW and the dynamic behaviours of spiral waves were evaluated for the WT, HT10 and HT25 cases. For the 3D simulations, the model described in Sections 3.1 and 3.2 was used. Since the intention was just to investigate the influence of the mutation, the model was used without tissue anisotropy. The mutation was applied homogeneously with the electrical activity at all nodes described by either the WT or HT25 cells. There was no heterogeneity introduced to account for the differing cell types present in the human atrium. To examine the behaviour of scroll waves under WT and HT25 conditions a protocol analogous to the wave-break protocol described for 2D sheets of tissue was used [121]. The protocol is illustrated in figure 3.8. First, a small number of cells are simulated at one extreme of the atrial model. The excitation is allowed to propagate through the model until the S2 stimulus is delivered. The S2 stimulus is delivered via briefly clamping a section of the atrial model to 50 mV and then releasing the clamp. A correctly timed S2 stimulus results in a scroll wave on the wall of the right atrium. After initiation, the models were simulated until activity ceased or until 6 s of simulated time had elapsed.

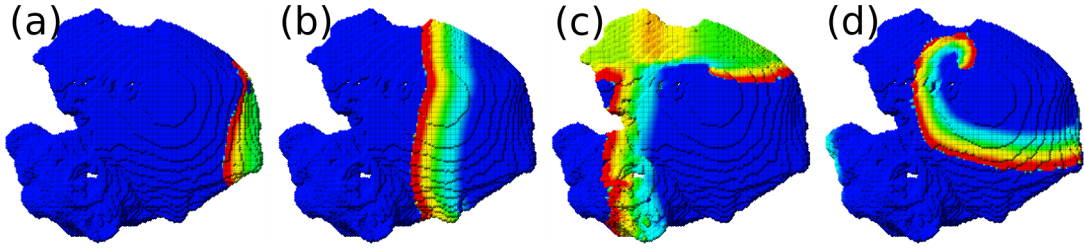


Figure 3.8: Stimulus protocol used to initiate a scroll wave. (a) One extreme of the atrial model is stimulated (b) The excitation is allowed to propagate (c) An S2 stimulus is delivered by clamping a section of the tissue, here the lower quarter. (d) A scroll wave begins on the wall of the right atrium.

Changes in APD₉₀ due to S140G mutation

The effect of an increase in the leakage current parameter were investigated. This was done using the standard APD₉₀ protocol and varying φ between 0 and 1. Variation in APD₉₀ as φ is altered is shown in figure 3.9(a). Representative APs are shown in figure 3.9(b). The APD₉₀ under Control conditions (WT) was seen to be 312.0 ms. Progressive mutation decreased the APD₉₀ to 150.5 ms in HT10 case and 79.3 ms in HT25 case. Under homozygous conditions, $\varphi = 1$ the APD₉₀ was seen to be 22.4 ms. Figure 3.9(b) shows the inclusion of the mutant channel causes the changes in morphology associated with none of the mutant types having a plateau region. Inclusion of the mutant channel decreased the upstroke velocity of the AP from 217.1 V/s in WT, to 214.0 V/s in HT10 and 208.6 V/s in HT25. The upstroke velocity in the homozygous case was 192.0 V/s. Figure 3.9(c) shows the current profiles of I_{Ks} over the course of an AP which correspond to the AP traces shown in panel B. I_{Ks} is seen to increase considerably in both the HT10 and HT25 cases compared with the WT case. The leak also changes the morphology of the current profile to one showing almost instant activation in HT10 and HT25 cases, compared to the slow activation in WT.

APDr,90 ERPr, CVr and VW

The APDr,90 figure 3.10(a), reflects the decreased APD₉₀ with the restitution curves considerably flattened for both the mutant cases. The ERPr curves, figure 3.10(b), also reflect the reduced APD₉₀ and show a similar flattening to that seen in the APDr,90 curves. At an S1 interval of 1000 ms the ERP was found to be 327.2 ms in WT, 168.4 ms in HT10 and 109.3 ms in HT25. In addition, the

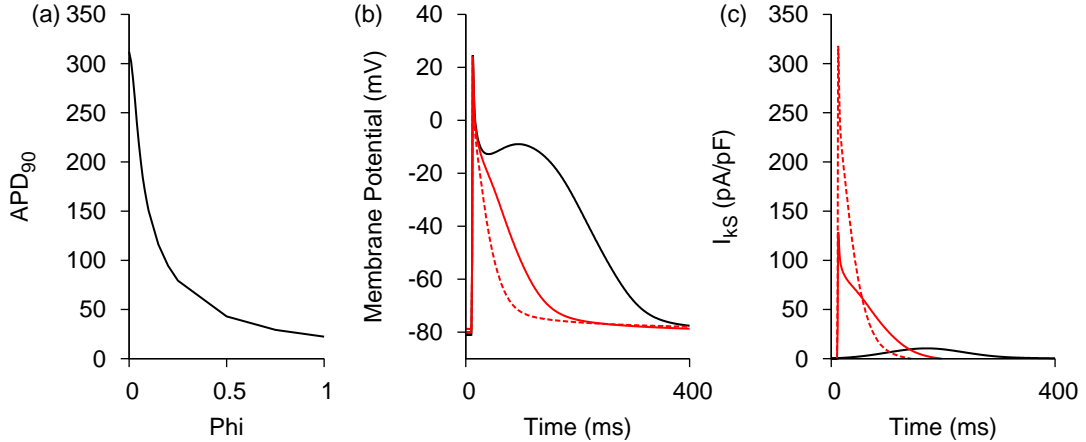


Figure 3.9: (a) Plot of APD_{90} vs φ , showing how increasing mutation reduces APD_{90} . AP profiles (a) and I_{Ks} current profiles (b) for WT (black), HT10 (red, solid) and HT25 (red, dashed). Stimulus is delivered at 10 ms. Note the large increase in current density under the S140G mutation, which causes a corresponding flattening of the AP profiles and removal of the plateau.

mutant cases supported excitation at much lower S1 intervals (or higher pacing rate) compared to the control case. The minimum S1 interval sustained during the $ERPr$ calculations was 328.7 ms in WT, 184.3 ms in HT10 and 126.7 ms in HT25. The solitary wave CV was not altered considerably by the mutation (26.7 cms^{-1} in WT c.f. 26.8 cms^{-1} in HT25). The CVr figure 3.10(c), curves confirm the findings of the $ERPr$ calculations, that the mutant case supports successful excitation after a considerably reduced S2 interval. The minimum S2 interval which still allowed the test stimulus to propagate was found to be 317.1 ms in WT, 151.7 ms in HT10 and 92.5 ms in HT25. Vulnerability to premature excitation was relatively unaffected by the mutation. It was observed to increase in tissues where the mutation was present from a VW of 3.2 ms in WT to 3.4 ms in HT10 and 3.3 ms in HT25 (figure 3.10(d)). This is a small (less than 5 %) change in the VW to premature excitation.

Dynamic Behaviours on a 2D sheet

Re-entry was initiated in 2D sheets of homogeneous virtual human atrial tissues for WT, HT10 and HT25 cases. The dynamical behaviours of the system were observed for 10 s or until all electrical activity ceased after the re-entry self terminated. Frames from the simulation and spiral tip traces are shown in figure 3.11. The lifespan of re-entrant waves in the WT case was seen to be 2.8 s, whilst in

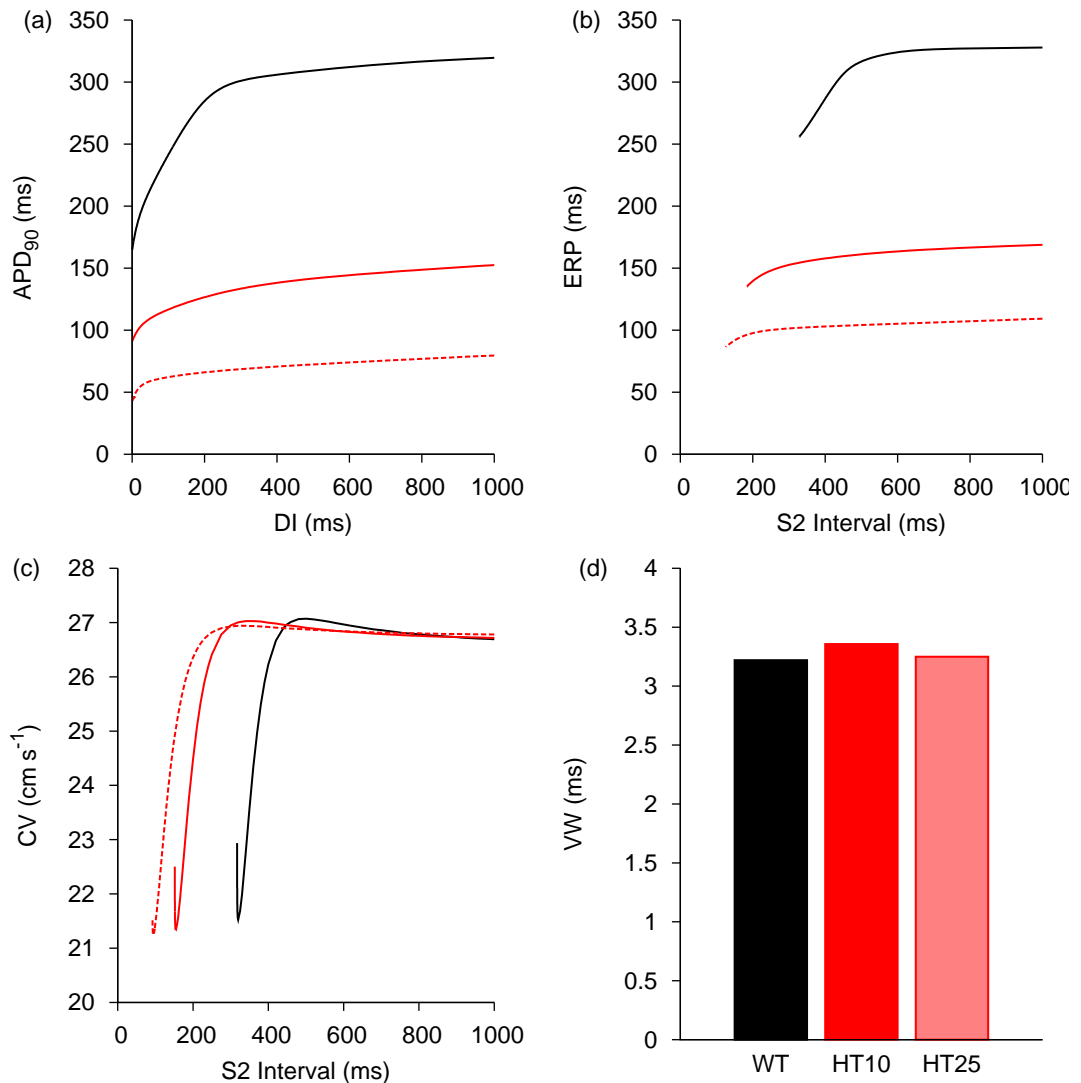


Figure 3.10: Restitution curves for WT (black), HT10 (red, solid) and HT25 (red, dashed). (a) $APDr_{90}$. (b) $ERPr$. (c) CVr . (d) Temporal VW to premature stimulus.

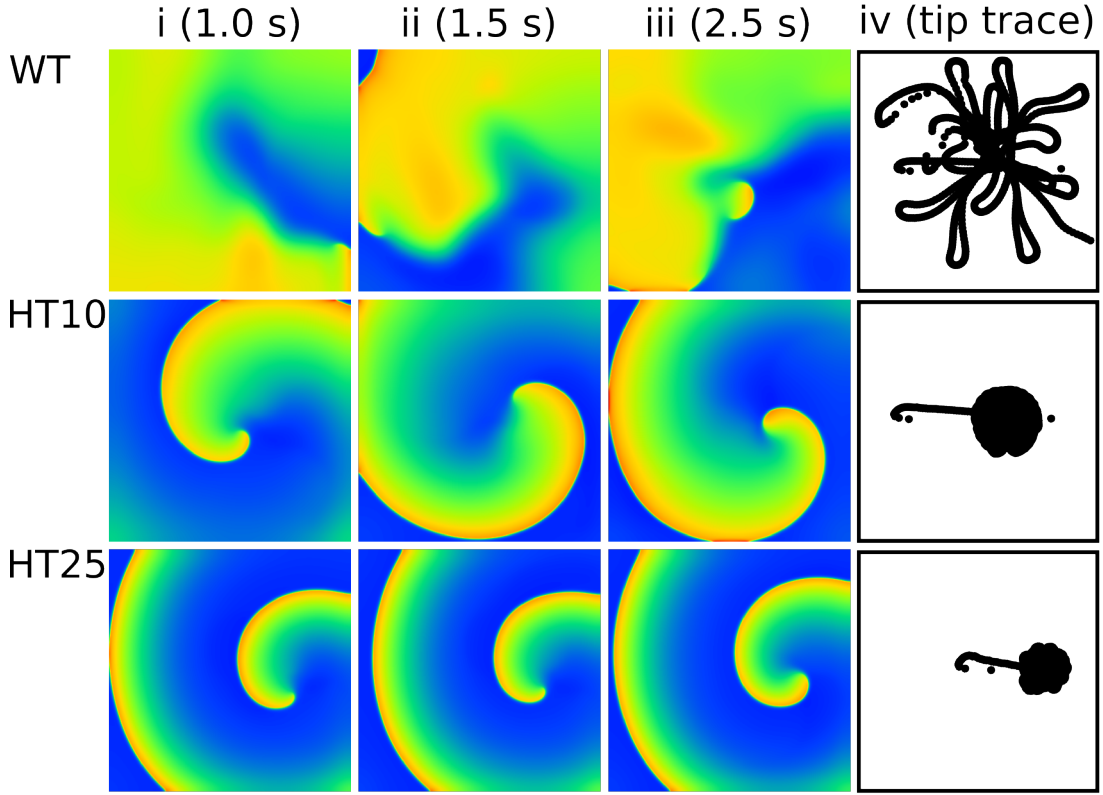


Figure 3.11: Snapshots of electrical activity extracted at 1 s (i), 1.5 s (ii) and 2.5 s (iii) after spiral wave initiation, with accompanying tip trace shown in (IV) for WT (top), HT10 (middle) and HT25 (bottom). In the electrical activity plots red is fully depolarized, blue is the resting potential. The WT spiral occupies much more of the tissue and has a very large meander, compared with the HT10 and HT25 cases, which show a very stable spiral after the initial transitory behaviour.

both the HT10 and HT25 cases the re-entry persisted for the duration of the simulation (10 s). In the WT case the spiral tip showed a large degree of meander (figure 3.11,top row, column iv) even after the initial transitory period. The tip trajectory shows that the spiral wave completes several rotations, each accompanied by large movements of the tip before finally tip exits along the lower edge of the tissue, unable to move back into the tissue due to its own refractory tail. In contrast in both HT10 and HT25 cases the meander is confined to a relatively small area after after the initial transitory period. The spiral wave tip precesses around a stationary point in a flower petal pattern, indicative of a highly stable re-entrant wave.

Representative APs were extracted from a point in the tissue and used in dominant frequency analysis, shown in figure 3.12. From the representative APs

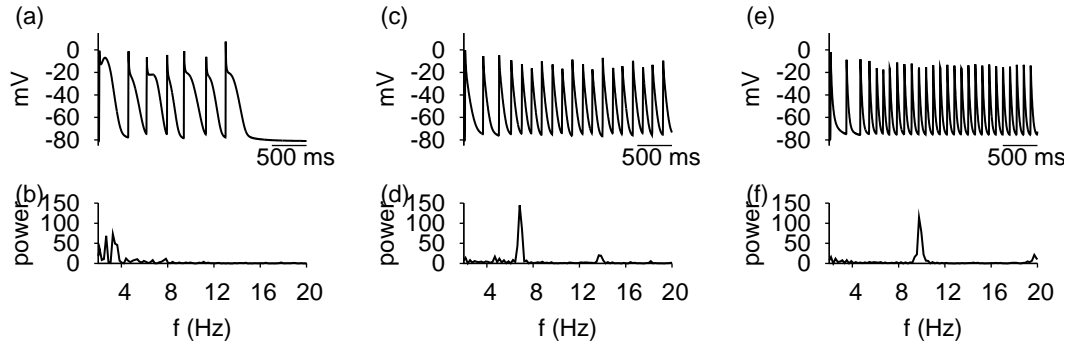


Figure 3.12: Representative AP traces (top panels) and dominant frequency analysis (bottom panels) for WT (left), HT10 (centre) and HT25 (right). Traces extracted from a point 6 mm from top and left of the 2D sheets every 2.5 ms of elapsed time.

(top panels) it can be seen that the APD_{90} decreases as a greater proportion of the mutation is present. The WT case also shows obvious alternans in the AP profiles reflecting its unstable and meandering spiral wave, contrasting with the general uniform APs seen with the HT10 and HT25 cases. Dominant frequency analysis of AP profiles (bottom panels) extracted along the sheet diagonal was performed. The dominant frequency analysis shows that whilst in the WT case there is a relatively low frequency of oscillations (less than 4 Hz) compared with the mutant cases (7 Hz in HT10, 10 Hz in HT25). The width of the peaks for the two mutant cases are smaller, indicating a greater stability compared to the more dispersed frequencies seen in the WT case.

The minimal stimulus substrate size was computed as shown in figure 3.13. The mutation induced remodelling dramatically reduced the size of the SVW, from 99.1 mm in WT conditions to 12.3 mm in HT25 conditions, a reduction of 87.5%.

Modelling the S140G mutation in the Whole Atrium

Scroll waves were initiated in the whole atrial model as described in 3.4. Scroll wave behaviour for control (WT) and $\varphi = 0.25$ (HT25) were studied as representative cases. The scroll waves were initiated on the right atrial free wall to allow initiation and initial evolution without interference with anatomical obstacles. The 3D simulation visualisations are presented in figure 3.14. In WT conditions, as observed in the 2D simulations, the scroll waves have a large meander and self-terminated in approximately 4.2 s. As long as the scroll wave was initiated

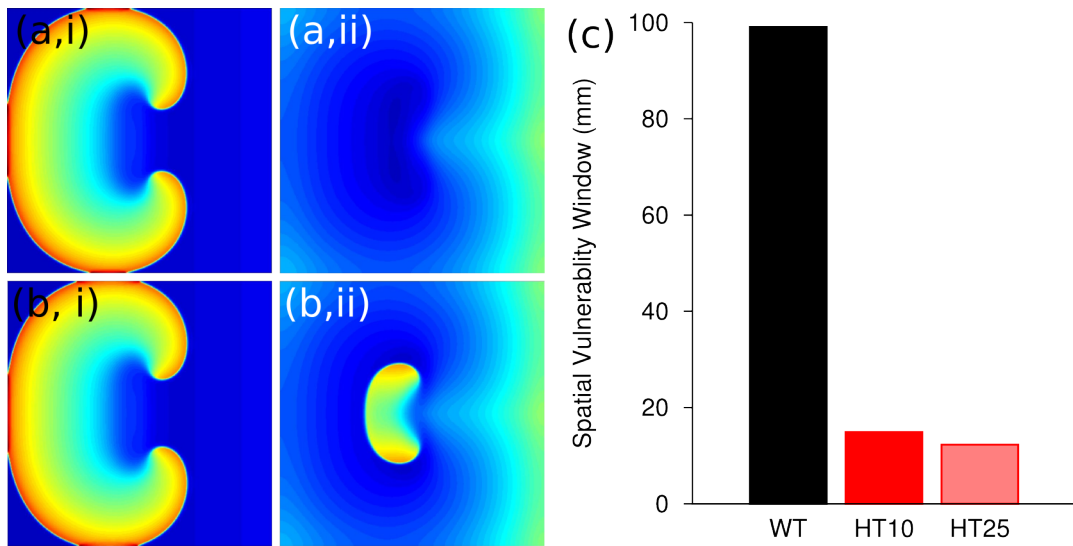


Figure 3.13: (a) Unsuccessful attempt at initiating figure-of-eight re-entry just before (I) and after (II) re-entry would occur. (b) Successful initiation of figure-of-eight re-entry just before (I) and just after (II) re-entry is initiated. (c) Spatial vulnerability window for WT (black), HT10 (red) and HT25 (pink) tissue. Spatial vulnerability window is the minimum length of tissue that produces figure-of-eight re-entry.

far from anatomical obstacles such as venous openings, self-termination was independent of position. In certain cases where it was not ‘entrainment’ of the scroll wave around an anatomical obstacle was observed, leading to prolonged scroll wave activity even in the WT case. Under HT25 conditions the small wavelength allowed scroll waves to become persistent in all cases, as observed in 2D simulations. In contrast to the 2D simulations the presence of anatomical obstacles led to break up of the scroll wave into erratic propagations and short-lived wavelets. This erratic behaviour then persisted until the end of simulation at 6 s.

Representative AP profiles were extracted from several points throughout the atrial model and used in dominant frequency analysis. The dominant frequency in the HT25 case was found to be much higher, approximately 10 Hz, than in the WT case, less than 3 Hz.

Discussion and Conclusions of the S140G Study

The S140G mutation of the KCNQ1 β subunit of the I_{Ks} ion channel causes a large gain of function. This gain of function manifests as a component of the I_{Ks} channel which shows instantaneous activation kinetics under voltage clamp

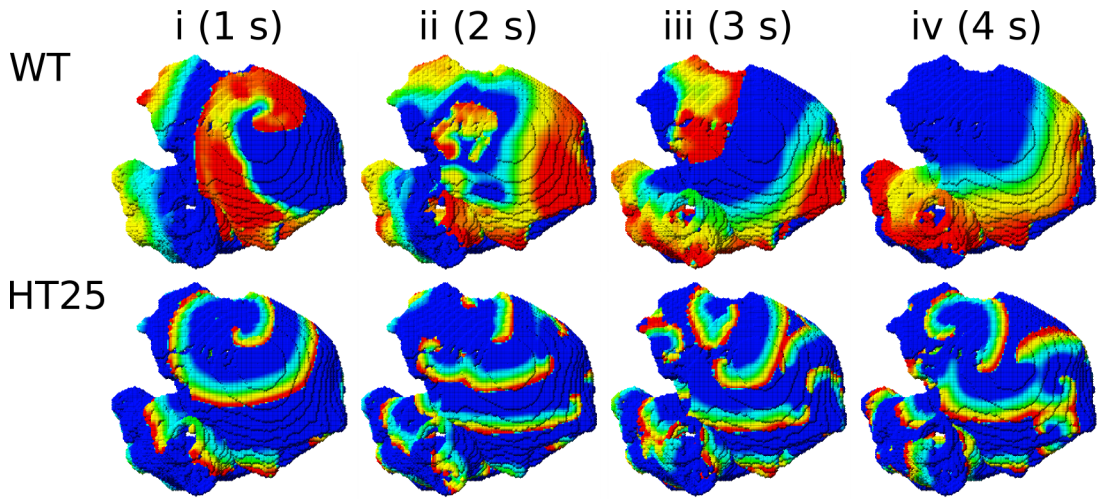


Figure 3.14: Snapshots of the membrane potential for WT (top panels) and HT25 (bottom panels) taken at 1 s (i), 2 s (ii), 3 s (iii) and 4 s (iv) of simulated time. In the plots, red shows full depolarized tissue, whilst blue tissue is at rest. By 2 s the activity shown in panel bottom,ii has started to break up, compared with the more stable ave shown in the upper panel, just about to self-terminate in panel top,iv, as the excitation wavefront hits the non-conducting atrio-ventricular ring.

conditions. Modelling the effects of the mutation as the addition of a leakage component with constant conductance to the I_{Ks} channel therefore seems to be a good fit to the experimental data provided by Chen et al. Incorporation of the mutation into models of cellular electrophysiology dramatically reduces the APD_{90} and the ERP. The increased repolarization current also flattens the plateau region, or eliminates it entirely. Conduction velocity was not significantly affected by the presence of the mutation, possibly due to the leakage component being inward at resting potentials, contributing to the upstroke. In 2D simulations, the mutation stabilised re-entrant spiral waves, leading to long lived arrhythmic activity at a high frequency. In 3D, simulations showed that with the addition of anatomical obstacles, scroll-waves would instead break up. The shorter wavelength and refractory length introduced by the mutation assists in the maintenance of the fibrillatory activity. The fibrillatory activity in the presence of the mutation shows a very high frequency, approximately 600 bpm, which is in agreement with the definition Chen et al. used when selecting AF sufferers for their study. The Chen et al. hypothesis is supported by this study, which reproduces both voltage clamp experiments and then provides insight into the mechanisms responsible for the maintenance of AF in those afflicted with the mutation.

Repolarisation of cardiac myocytes depends on the I_{K_s} (KCNQ1/KCNE1) and I_{K_r} (hERG) channels. Previous clinical and simulation studies have linked mutation leading to gain of function in the I_{K_s} to SQT syndromes [139, 140]. Studies by Bosch and Workmann into AF induced remodelling focused on the I_{K_1} and I_{to} potassium channels, as well as the L-type calcium channel. Atrial I_{K_s} is a much lower magnitude than ventricular I_{K_s} so its upregulation may have been overlooked in their studies. The simulations shows that I_{K_s} has an important role to play in the behaviour of atrial cell electrophysiology and that gain of function mutations in the channel can lead to a large reduction in the APD₉₀ and ERP.

This study was carried out using a model of the human atria which omitted spatial and electrical heterogeneity. This allowed the mutation to be studied without the additional complexity introduced by heterogeneity. In addition, it is well known that AF can induce significant structural remodelling [141, 142] with most AF observed in clinical settings accompanied by cardiac structural disorders. Inter-myocyte coupling can also be influenced [143] by chronic atrial fibrillation. Such etiology is beyond the scope of this study and would be a significant investigation in its own right. Despite the relative simplicity of the study in 3D, the control cases still show self-termination as expected, whilst the presence of the mutation leads to breakup and fibrillation. Simulation studies allow modelling of only the aspects of the disease which interest the investigator.

Electrical remodelling involves complex regulatory mechanisms. AF is known to be associated with the remodelling of several ion channels. Recent clinical studies have identified numerous genes [140, 144–150] responsible for a propensity towards AF due to reductions in the ERP and APD₉₀. A recent modelling study of mutation in the KCNJ2 Kir2.1 gene [103], leading to gain of function in the I_{K_1} channel, was found to lead to dramatic reduction in ERP and APD₉₀. An extension of the simulation study into three dimensions showed that it led to persistent and erratic propagations. A gain of function in the potassium repolarization currents seems to lead to behaviour which is qualitatively, if not quantitatively, similar to the study presented in this chapter.

Computational studies of AF have investigated the effects of AF at both cellular and tissue levels. Cellular effects of AF are important and have been explored in several investigations [102, 151, 152]. On the tissue level, Pandit et al. have studied the effects of channel blocking on 2D propagations [153]. Three

dimensional studies have included Reumann et al. who used a cellular automaton based model of the human atria to study AF [137]. Such a model, by its nature, does not consider the continuous time variation of potentials within the human atria, and may accumulate significant error in a short period of time.

3.5 Modelling the Whole Atrium: Conclusion

A realistic model of the human atria has been developed. The model uses a biophysically detailed second generation cellular electrophysiological model to describe the action potential kinetics at each node. The model includes a simplistic but effective electrophysiological heterogeneity, in the absence of more detailed experimental data. Solution times for the model are improved by the use of lookup tables for voltage dependent values. The geometry is based on data from a real human dataset. A simple description of fibre orientation has been included and conduction anisotropy has been considered. The resulting whole atrium model has a good parallel fraction and is solvable in tractable times on modern hardware.

The model accurately reproduces the activation sequence of the healthy human atrium. Time to total activation and individual tissue conduction velocities both fall within experimental and clinical values. Thanks to the use of a biophysically detailed model of cellular action potential, the model can also be used to simulate pathological cases such as familial atrial fibrillation.

The S140G mutation in the KCNQ1 protein causes a dramatic change in the electrophysiological behaviours of the I_{Ks} rectifier current. The up-regulation of the I_{Ks} channel causes a large reduction in the APD₉₀. This then influences the rest of the electrophysiology, effecting all aspects of the cellular electrical behaviour. It is very easy to see how the mutation is associated with a prevalence of atrial fibrillation in families which have inherited the gene.

Chapter 4

The Body Surface Potential

Modelling the atrium itself can provide valuable insight into the effects and mechanisms of drugs, diseases and inherited conditions as discussed in Chapters 2 and 3. These simulation studies directly compute the electrical potentials generated by the heart. However, such measurements are not available to physicians without the insertion of a catheter electrode or other, more involved, surgical procedures. Instead they must rely on external tools such as the echocardiogram and the electrocardiogram (ECG). To reproduce the ECG with mathematical models, it is necessary to solve the forward problem.

4.1 The Forward Problem

As was noted earlier (§1.4.3) solving the forward problem involves solving Poisson's equation in the body. In an infinite homogeneous conducting medium, a solution to Poisson's equation for the field at any given point, ϕ , is [154]

$$\phi = \frac{1}{4\pi\sigma} \int \frac{-\nabla \cdot \mathbf{J}^i}{r} dv \quad (4.1)$$

where r is the (scalar) distance from the elemental volume dv to the point at which the field is being evaluated. This is shown in figure 4.1. The distance r is the magnitude of the vector $\mathbf{r}' - \mathbf{r}$.

To account for the influence of the torso on the extra-cardiac potentials, we use a Boundary Element Method (BEM). The derivation for the BEM method is based on Green's Theorem [64, 77, 78], which states that for a volume, V , bounded

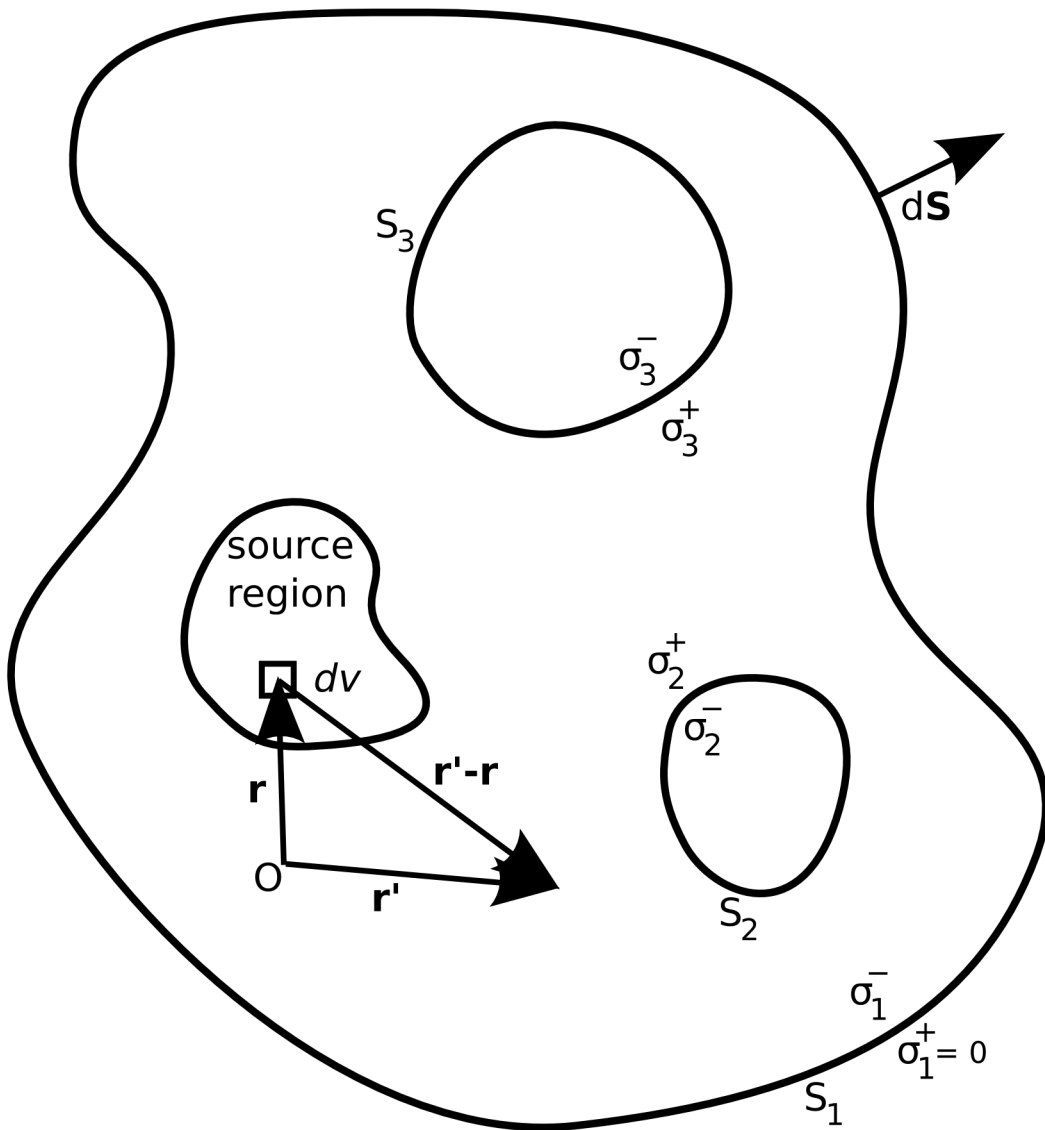


Figure 4.1: Vectors and surfaces involved in the boundary element method. The origin is at point O . There are three surfaces shown in the diagram: S_1 , S_2 and S_3 . Each surface has an internal, σ^- and an external, σ^+ , conductivity. The S_1 surface is the boundary of the region and contains all other surfaces and dipole sources. The external conductivity of S_1 , σ_1^+ , is therefore zero. The vector $d\mathbf{S}$ represents an infinitesimal element of the boundary surface.

The dipole sources are all contained within the region labelled 'source region'. The vector \mathbf{r} is a vector to a volume element dv in the source region. The vector \mathbf{r}' is a vector to an arbitrary point within the volume bounded by S_1 .

by a surface, S , that

$$\int_V (\phi \nabla^2 \psi - \psi \nabla^2 \phi) dv = \int_S (\phi \nabla \psi - \psi \nabla \phi) \cdot d\mathbf{S} \quad (4.2)$$

where ϕ and ψ are scalar functions of position. If ϕ is the electrical potential and ψ is set as $\frac{1}{r}$ where r is $|\mathbf{r}' - \mathbf{r}|$. Here, \mathbf{r}' is a vector to an arbitrary point in the volume V at which we wish to evaluate the field and \mathbf{r} is a vector to an elemental volume, dv , somewhere within the volume V . Using possion's equation (1.29) we have

$$\int_V \left(\phi \nabla^2 \left(\frac{1}{r} \right) - \frac{1}{r} \frac{(\nabla \cdot \mathbf{J}^i)}{\sigma} \right) dv = \int_S \left(\phi \nabla \left(\frac{1}{r} \right) - \left(\frac{1}{r} \right) \nabla \phi \right) \cdot d\mathbf{S} \quad (4.3)$$

The del operator in (4.3) operates on the unprimed (source) coordinates. Now,

$$\nabla^2 \left(\frac{1}{r} \right) = \nabla^2 \left(\frac{1}{|\mathbf{r}' - \mathbf{r}|} \right) = -4\pi\delta(\mathbf{r}' - \mathbf{r}) \quad (4.4)$$

where δ represents the dirac delta function. The surface S is the body surface and so on S , $\nabla \phi \cdot d\mathbf{S} = 0$ to a very good approximation. (4.3) becomes, after substitution and rearrangement,

$$\phi(\mathbf{r}') = \frac{1}{4\pi\sigma} \int_V \frac{-\nabla \cdot \mathbf{J}^i}{r} dv - \frac{1}{4\pi} \int_S \phi(\mathbf{r}) \nabla \left(\frac{1}{r} \right) \cdot d\mathbf{S} \quad (4.5)$$

By noting that

$$\nabla \left(\frac{1}{r} \right) \cdot d\mathbf{S} = \frac{(\mathbf{r}' - \mathbf{r})}{|\mathbf{r}' - \mathbf{r}|^3} \cdot d\mathbf{S} = d\Omega \quad (4.6)$$

where $d\Omega$ is a differential element of solid angle, (4.5) becomes

$$\phi(\mathbf{r}') = \frac{1}{4\pi\sigma} \int_V \frac{-\nabla \cdot \mathbf{J}^i}{r} dv - \frac{1}{4\pi} \int_S \phi(\mathbf{r}) d\Omega \quad (4.7)$$

The first term on the right hand side can be recognised as the infinite medium potential (4.1) and the second term consists of contributions from the torso surface. To discretise (4.7) we can consider S to be made up of n triangles, leading to

$$\phi(\mathbf{r}') \approx \frac{1}{4\pi\sigma} \int_V \frac{-\nabla \cdot \mathbf{J}^i}{r} dv - \frac{1}{4\pi} \sum_{j=1}^n \phi_j \Delta\Omega_j \quad (4.8)$$

where ϕ_j is the potential on the j^{th} surface element and $\Delta\Omega_j$ is the increment of

solid angle of the j^{th} element when viewed from \mathbf{r}' . To find a solution, Barr et al. noted that $\phi(\mathbf{r}')$ is the potential at an arbitrary point inside V . If these points are chosen to be at the centres of the triangles just inside the surface S then since $\nabla\phi \cdot d\mathbf{S} = 0$ we can get an expression for the potential on the i^{th} triangle, ϕ_i ,

$$\phi_i = \frac{1}{4\pi\sigma} \int_V \frac{-\nabla \cdot \mathbf{J}^i}{r} dv - \frac{1}{4\pi} \sum_{j=1}^n \phi_j \Delta\Omega_{ij} \quad (4.9)$$

where $\Delta\Omega_{ij}$ is the solid angle of the j^{th} triangle seen from the i^{th} triangle. In the summation in (4.9) there is one term which corresponds to the case where $i = j$. In this case, $\Delta\Omega_{ii} = -2\pi$ as from a point just inside i , i will obscure an angle of -2π . (As a consequence of the vector definition of solid angle, the solid angle obscured at any point within is negative) Equation (4.9) then becomes, after rearrangement,

$$\frac{\phi_i}{2} + \sum_{j=1, j \neq i}^n \left(\frac{\Delta\Omega_{ij}}{4\pi} \right) \phi_j = \frac{1}{4\pi\sigma} \int_V \frac{-\nabla \cdot \mathbf{J}^i}{r} dv \quad (4.10)$$

which represents a set of n simultaneous equations for the potentials on the surface elements of the torso. Using an alternate formulation of (4.1) [154] in which \mathbf{J}^i can be considered a dipole density

$$B_i = \frac{1}{4\pi\sigma} \int_V \frac{\mathbf{J}^i \cdot (\mathbf{r}' - \mathbf{r})}{r^3} dv \quad (4.11)$$

equation (4.10) can be written in matrix form as

$$\mathbf{A}\phi = \mathbf{B} \quad (4.12)$$

where \mathbf{A} is a matrix which depends entirely on the geometry of the torso surface with a typical term of $A_{ij} = -\frac{\Delta\Omega_{ji}}{4\pi}$ and $A_{ii} = 0.5$, ϕ is a column vector of the potentials of the n triangles and \mathbf{B} is a column vector of the infinite medium potentials at the centres of the triangles of the surface.

Using a multiple surface generalisation of Green's theorem, equation (4.10) can be extended to allow for multiple inhomogeneities, derivations for which can be

found in [64, 67, 78]. For a body consisting of m surfaces:

$$\phi_i + \sum_{s=1}^m \left(\frac{\sigma_s^- - \sigma_s^+}{\sigma_r^- + \sigma_r^+} \right) \sum_{j=1, j \neq i}^n \left(\frac{\Delta\Omega_{ij}}{2\pi} \right) \phi_j = \frac{1}{2\pi(\sigma_r^- + \sigma_r^+)} \int_V \frac{-\nabla \cdot \mathbf{J}^i}{r} dv \quad (4.13)$$

Where r is the surface of the element i and s the surface of the element j .

If the surface S was discretised with sufficient accuracy then \mathbf{A} will necessarily be singular, due to the physical nature of the problem. This was noted by Salu [155] who proposed a solution which takes advantage of the physical properties of the system (an alternative method of removing the singularity of the system was proposed by Lynn and Timlake, the deflation method as by employed in [65]). Salu noted that, experimentally, the potential ϕ can only be determined up to an additive constant. Therefore ϕ can be taken as 0 at arbitrarily chosen point, without effecting the general solution. Assigning $\phi_1 = 0$ in (4.12) leads to

$$\sum_{j=2}^n A_{ij} \phi_j = B_i \quad i = 1, \dots, n \quad (4.14)$$

which is a set of n equations in $n - 1$ unknowns. These equations should have exactly one solution. If an exact solution exists, this implies two things: (a) (4.14) is a set of n consistent equations in $n - 1$ unknowns and (b) the rank of the sub-matrix $A_{ij} : i = 2, \dots, n, j = 2, \dots, n$ is $n - 1$. Hence there are n nontrivial λ_i such that the rows of \mathbf{A} fulfil

$$\sum_{i=1}^n \lambda_i A_{ij} = 0 \quad j = 2, \dots, n \quad (4.15)$$

The λ_i s may be determined up to a proportional factor. For (4.12) to be consistent, it is also required that

$$\sum_{i=1}^n \lambda_i B_i = 0 \quad (4.16)$$

Salu notes that (4.16) might not hold for a number of reasons, including numerical inaccuracies in the discretisation of surface or errors in the calculation of the B_i s. This would lead to a difference between $\phi_{\text{calculated}}$ and ϕ_{real} . Considering once more the physical properties of the system, B_i as an electrostatic potential could only

be determined up to some additive constant, α . Equation (4.15) then becomes

$$\sum_{i=1}^n \lambda_i (B_i + \alpha) = 0 \quad (4.17)$$

This can be incorporated into (4.14) to get a set of n equations

$$\sum_{j=2}^n A_{ij} \phi_j = B_i + \alpha \quad i = 1, \dots, n \quad (4.18)$$

Equation (4.18) is now numerically consistent and is equivalent to (4.12). Whenever (4.16) is not fulfilled, due to numerical errors in the discretisation and creation of \mathbf{A} or in the calculation of \mathbf{B} , the addition of the α term ensures that (4.18) has a consistent solution. It is important to note that consistent does not necessarily mean accurate or correct. The addition of the α term merely ensures that a solution will exist. Due care must still be taken with the construction of each A_{ij} term and accuracy can be improved via choosing a finer discretisation for the body surface mesh.

An efficient solution to the problem of solving the equations and for α was given by Salu. To do this, we let $\phi_j^*(j = 2, \dots, n)$ be a solution to the $n - 1$ equations

$$\sum_{j=2}^n A_{ij} \phi_j^* = B_i \quad i = 2, \dots, n \quad (4.19)$$

and let $\phi_j^1(j = 2, \dots, n)$ be a solution to the $n - 1$ equations

$$\sum_{j=2}^n A_{ij} \phi_j^1 = 1 \quad i = 2, \dots, n \quad (4.20)$$

where the 1 represents a column vector of 1s. The two vectors ϕ_j^* and ϕ_j^1 both multiply the same matrix, \mathbf{A} so it need only be inverted once to solve both (4.19) and (4.20). Letting $\phi_j(j = 2, \dots, n)$ be a solution to the set of $n - 1$ equations

$$\sum_{j=2}^n A_{ij} \phi_j = B_i + \alpha \quad i = 2, \dots, n \quad (4.21)$$

where α is the same alpha introduced in (4.17). From equations (4.19)–(4.21),

the solution to the set of equations will be

$$\begin{aligned}\phi_j &= \phi_j^* + \alpha\phi_j^1 \quad j = 2, \dots, n \\ \phi_1 &= 0\end{aligned}\tag{4.22}$$

Substituting (4.22) into the first equation of (4.18) will give

$$\sum_{j=2}^n A_{1j} (\phi_j^* + \alpha\phi_j^1) = B_i + \alpha \tag{4.23}$$

or after re-arranging to solve for α

$$\alpha = \frac{\left(\sum_{j=2}^n A_{1j} \phi_j^* \right) - B_i}{1 - \left(\sum_{j=2}^n A_{1j} \phi_j^1 \right)} \tag{4.24}$$

Equation (4.24) can be used along with (4.19)–(4.21) to solve (4.12) to find the body surface potential.

4.2 The Atrial Dipole

In the previous section, the method for solving Maxwell's equations to determine the body surface potential was derived. The \mathbf{B} term in the Equation (4.12) is the infinite homogeneous medium potential for a number of impressed current sources \mathbf{J}^i . The model of atrial electrophysiological activity developed in the previous chapter provides an output of the trans-membrane potentials, V_m . To relate the values of V_m to \mathbf{J}^i we consider the bidomain model [31, 156]. As previously discussed, the bidomain model considers the cardiac tissue as comprising two ‘syncytica’ occupying the whole of cardiac tissue and separated by the cell membrane. These are the intra- and extra-cellular spaces. This leads to the following two relationships

$$\mathbf{J}_i = -\sigma_i \nabla \phi_i \tag{4.25}$$

$$\mathbf{J}_e = -\sigma_e \nabla \phi_e \tag{4.26}$$

where \mathbf{J} is a current density, σ is the conductivity, ϕ is the potential and the subscripts ‘i’ and ‘e’ denote the intra- and extra-cellular spaces, respectively.

Charge moving from one space to another must cross the cell membrane and is conserved, leading to the following relationship for I_m , the membrane current per unit volume

$$I_m = -\nabla \cdot \mathbf{J}_e = \nabla \cdot \mathbf{J}_i \quad (4.27)$$

By definition the transmembrane potential, V_m is

$$V_m = \phi_i - \phi_e \quad (4.28)$$

Combining these two equations leads to

$$\nabla \cdot \sigma_i \nabla V_m = -\nabla \cdot \sigma \nabla \phi_e \quad (4.29)$$

where $\sigma = \sigma_i + \sigma_e$, the bulk conductivity of the cardiac tissue. Equation (4.29) is of the form of Poisson's equation. The equation can be interpreted to indicate that the term on the left hand side is the source of the extracellular potentials. By comparing (4.29) with (1.29) it is obvious that

$$\mathbf{J}^i = -\sigma_i \nabla V_m. \quad (4.30)$$

4.3 Torso Geometry

The torso geometry used in this study is shown in figure 4.2(a). It was created by Weixue and Ling [70, 71] and has been used in numerous simulations. The geometry was derived from CT images of the human torso. The geometry consists of 412 vertices which were linked by 820 triangular elements for the thorax and 297 vertices for the lungs which were linked by 586 triangles. In addition, a geometric representation of the ventricular blood masses was constructed based on the ventricular mesh from the Weixue and Ling geometry. This mesh had 295 vertices and 582 elements. The blood masses of the atria were approximated by a pair of spheres, situated in the centre of the atrial chambers. The spheres for the left and right atria each had 162 vertices linked by 320 triangular elements. These meshes were subdivided using the Blender [157] graphical package into meshes consisting of 13120 elements for the torso, 2344 elements for the lungs and 2328 for the ventricular blood masses. Subdividing the meshes in this way did not influence the final form of the ECG significantly, but did improve the clarity of visualisation of the body surface potential. Initial studies using a spherical

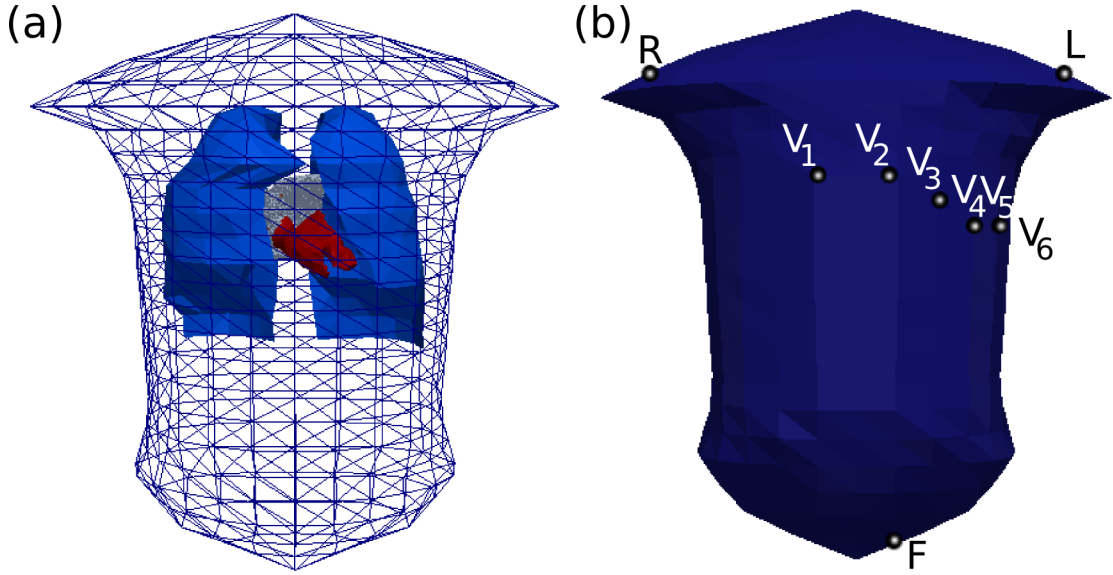


Figure 4.2: (a) Torso geometry used in this study. The torso geometry, shown unrefined for clarity is shown as a wireframe. The lungs are shown in blue, the blood masses in red. The atrium is visible above the bloodmasses. (b) Solid torso geometry showing the locations used for the simulated electrodes.

geometry with a similar number of triangle and the analytical formula for the potential within a conducting sphere suggest that the errors [158] induced through the descretisation are less than 0.01%.

The atrial model constructed in the previous chapter was positioned within the torso using the descriptions of Ho and Sánchez-Quintana [6] with the ventricular meshes from the original torso used as an additional guide. First, the model was centred in the atrial co-ordinate system. Using the z-x-z convention for Euler angles [159] acting on the heart (rather than the co-ordinate system of the heart), the atrium was rotated by (315, 135, 310). Following rotation, a translation of $(-0.003, -0.075, -0.217)$ was applied to the atrium. Several of the triangular elements were picked as the sites of the ECG electrodes. The electrode locations are shown in figure 4.2,(b). Conductances used for the various compartments of the torso are shown in table 4.1.

4.4 Computational Implementation

The program which solved the equations and generated the potentials at each of the elements of the geometry was written in the Fortran 95 programming

Table 4.1: Conductances used for the various compartments of the torso for solving the boundary element method [73].

Tissue	Conductivity
Torso	0.2 Sm^{-1}
Lungs	0.08 Sm^{-1}
Blood	0.6 Sm^{-1}

language. The **A** matrix from (4.12) was constructed using the method proposed by van Oosterom and Strackee [160] to estimate the solid angle subtended by each triangular element. A subroutine written in C was used to read in the gzip or xz compressed data files corresponding to each snapshot in time (1 ms) generated by the atrial model. The impressed current density at each node of the tissue was calculated using (4.30). To reduce computational time and memory requirements, the atrial geometry was divided into 10x10x10 node blocks, around 4000 of which actually had active nodes within. The dipoles generated by each active node were aggregated and considered to act at the centroid of the block determined from the distribution of active nodes within the block. These ‘large’ dipoles were then used as the source terms in (4.1). To reduce computation time, the equations were formed into 3 sets of coefficient matrices, corresponding to the x, y and z components of the radius vector. These were then multiplied by the relevant dipole components and the results summed to calculate the potential in the centre of each element. Decreasing the block size to 5x5x5 nodes had a negligible effect on the computed body surface potential. From these dipoles, the **B** matrix was calculated.

To solve the resulting set of equations, the LAPACK [161] library was used. The **A** matrix was factorized using the SGTRF sub-routine. Numerical experiments determined that only single precision arithmetic was required. Solutions calculated using double and single precision showed differences only at the limits of single precision accuracy—approximately 7 significant figures. Since the torso is static this need only be done once, at the start of the calculations. The SGTRRS sub-routine was then used to solve (4.20) and (4.19) for each time snapshot using this factorised matrix. The zero potential, required for the consistency criterion of Salu, was chosen to be at element 1 of the mesh. This element is located at the top of the mesh, at the ‘neck’. Generating the body surface potential took

one core of horace approximately 60 minutes for 2 s of atrial activity using the original mesh. Using the fully refined mesh required approximately 190 minutes for the same computation.

After computation of the potentials at all points on the body surface, the results were post-processed to extract the ECG. These data were stored in a JSON [162] formatted file which contained arrays representing the voltage of each of the 12 leads, the time step between each point and, optionally, information on the parameters used by the BSP algorithm. JSON offers a lightweight alternative to XML, whilst still being highly readable without the aid of computer translation. The high-precision ECG signals, typically at a frequency of 1 kHz were been passed through a digital low-pass filter at 100 Hz, corresponding to the typical frequency response of a clinical ECG unit, from 0.5 Hz to 100 Hz. Using the three limb leads (LA, LL, RA) the WCT was computed and used to construct isopotential maps. Whilst the algorithm employed offers a natural zero potential, the use of the WCT allows for direct comparison with clinical studies which almost exclusively employ the WCT for this purpose [163, 164]

4.5 Simulating Sinus Rhythm

To simulate the P-wave body surface potential and ECG for the atrium in sinus rhythm, the atrial model developed in the previous chapter was used. The simulation of the electrical activity involved the full fibre orientation description with an anisotropy ratio of 1:9. There was heterogeneous cell electrophysiology used, with differential electrophysiology for the atrial myocyte, pectinate muscle and crista terminalis cells. The atrium was paced at the site corresponding to the sinus node at a frequency of 1 Hz for 2 s. The body surface potential was calculated both with and without the presence of internal inhomogeneities by setting the internal conductivity of the relevant compartment to the value in table 4.1 to include that compartment, or to the torso conductivity to remove its influence.

4.5.1 Simulated Body Surface Potential Maps

The Body Surface Potential Maps (BSPM) were constructed from the output of the simulations. In the following descriptions, the distribution is described using the using the coordinate system of the body rather than of the image. Note that

the raw signals are presented here, that is to say there is no filtering performed on the signals in the time domain.

The evolution of the body surface potential on a homogeneous torso is shown in figure 4.3. The timings of the body surface potential snapshots correspond to the snapshots of membrane potential shown in figure 3.4. The potential distribution starts off very close to uniform in frame (i) at 10 ms after initial excitation. Only excitation and repolarization wavefronts generate dipoles and in the initial milliseconds the excitation wavefront is very small. In 4.3(iv) (25 ms after initial stimulus) there is an area of positive potential beginning to appear over the lower right lung, caused by the spread of excitation over the pectinate muscles. By frames (v) and (vi), the regions of different potential are much more regularly distributed with a predominately negative region centred on the upper right lung and a positive region over the lower torso, centered further to the right than the left. The excitation wavefront is moving towards the legs.

The three frames (vii–ix) corresponding to the plateau and beginnings of the repolarization show a much more diffuse arrangement of potentials. The distribution is approximately the mirror image of that seen during depolarisation, with the predominantly positive regions over the right shoulder. The diffuse pattern of potentials is caused by the slower repolarization of atrial myocytes compared to their depolarisation. It does not show a disturbance from the smooth pattern as seen for depolarisation in frame (iv) as the repolarization is less influenced by the underlying fibre structure.

The evolution of the body surface potential with lungs is shown in figure 4.4. In 4.4(iv) (25 ms after initial stimulus) a peak is beginning to appear over the lower right lung, caused as excitation starts to spread through the crista terminalis and pectinate muscles. By frames (v) and (vi), the potential is much more regularly distributed. In contrast to the simulation without lungs, the region of predominantly negative potential seems to be larger in spatial extent than that which is observed without lungs. The corresponding positive peak does not seem to be any more extended, but it does have a greater magnitude. It appears that the lungs act to give a slight amplification effect, increasing the ranges of potential seen [67].

The three frames (vii–ix) corresponding to the plateau and beginnings of the repolarization show a much more diffuse arrangement of potentials. The distribution is approximately the mirror image of that seen during depolarisation,

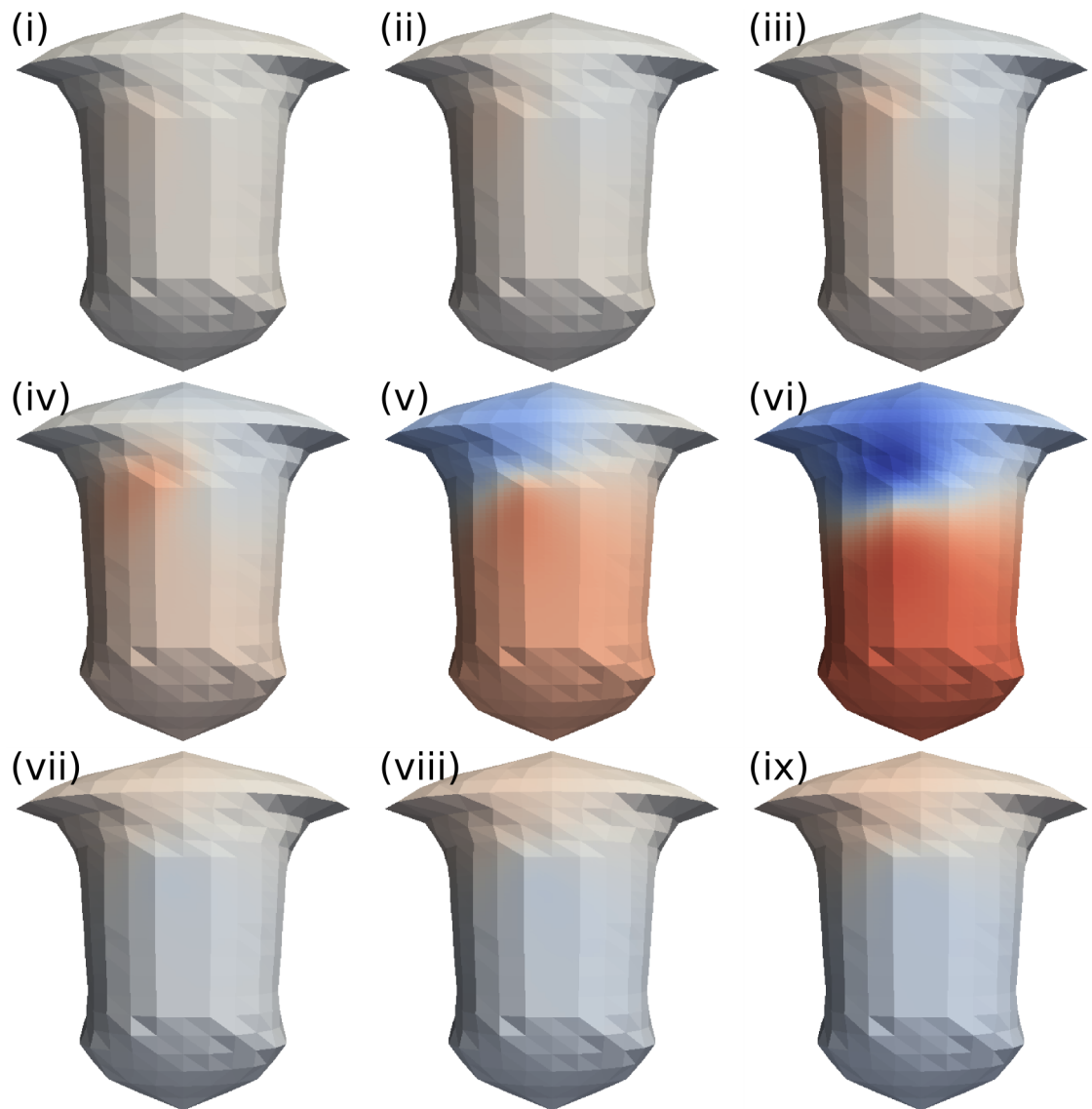


Figure 4.3: Simulated BPSM during sinus rhythm with a homogeneous torso. Blue represents negative potentials, and red positive ones, relative to the zero defined by the Wilson's central terminal. The torso begins approximately isopotential before a distinct pattern of potential, with an area of negative potential over the upper right lung and an area of positive potential on the lower torso. This pattern then reverses during repolarization, although the magnitudes are much lower. The maximum potential observed is 0.334 mV and the minimum is -0.412 mV. Snapshots shown for 10 ms (i), 15 ms (ii), 20 ms (iii), 25 ms (iv), 40 ms (v), 60 ms (vi), 180 ms (vii), 200 ms (viii) and 220 ms (ix)

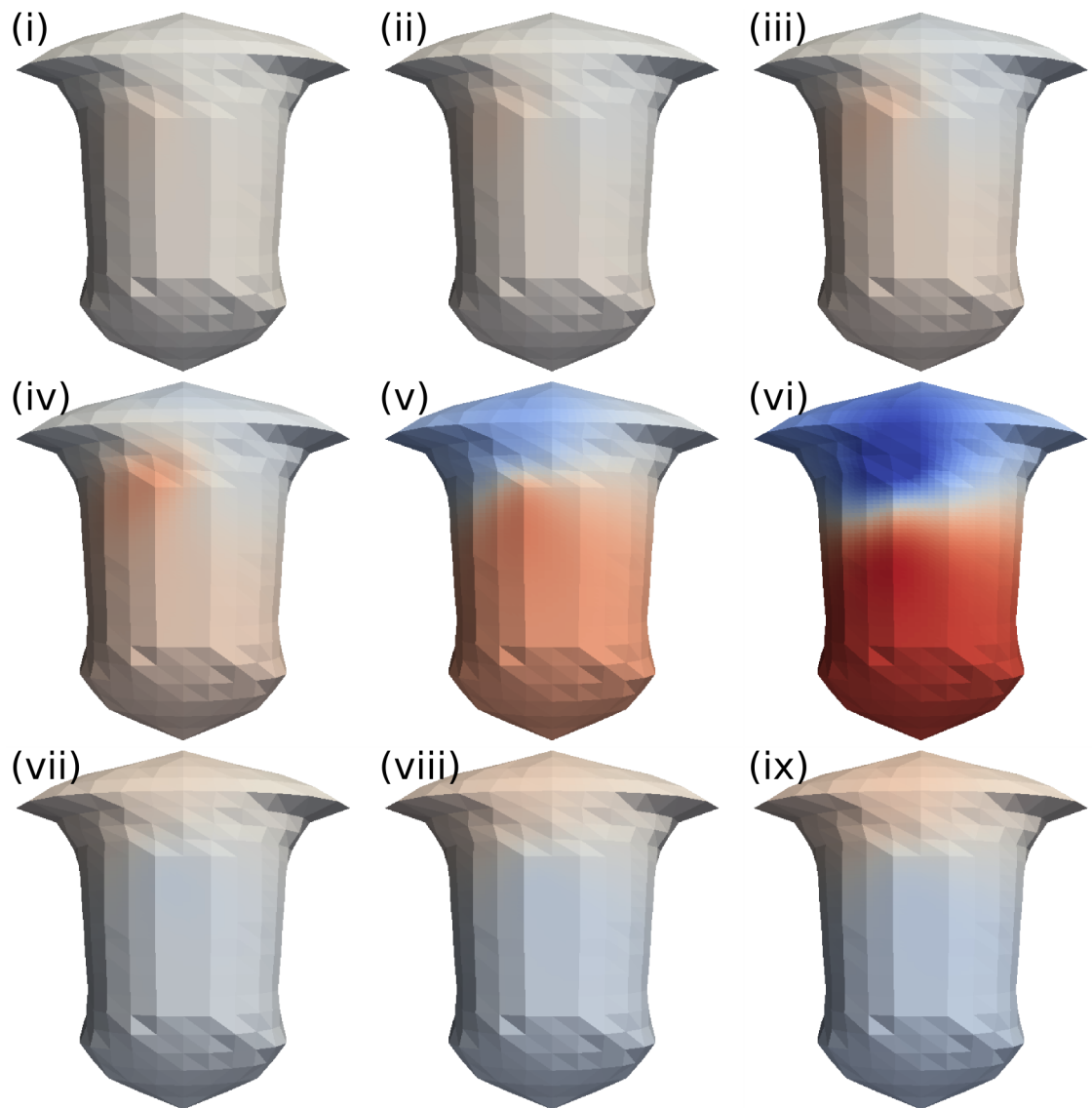


Figure 4.4: Simulated body surface potential plots during sinus rhythm with lungs assigned conductivity from table 4.1. Blue represents negative potentials, and red positive ones, relative to the zero defined by the Wilson's central terminal. The torso begins approximately isopotential before a distinct pattern of potential, with an area of negative potential over the upper right lung and area of positive potential on lower half of the torso. The positive peak is higher than that observed without lungs and the negative region appears to be larger. The positive–negative pattern then reverses during repolarization, with the upper torso having a positive potential. The maximum potential observed is 0.379 mV and the minimum is -0.475 mV. Snapshots shown for 10 ms (i), 15 ms (ii), 20 ms (iii), 25 ms (iv), 40 ms (v), 60 ms (vi), 180 ms (vii), 200 ms (viii) and 220 ms (ix)

with the predominantly positive regions over the right shoulder. The effects of the lungs are almost unnoticeable when compared to the simulations in the homogeneous torso.

The evolution of the body surface potential with blood masses present is shown in figure 4.5. The potential distribution is initially almost uniform, when in frame (i) at 10 ms after initial excitation. In 4.5(iv) a positive potential is beginning to appear over the lower right lung, caused by the rapid conduction along the crista terminalis and associated structures. In contrast to the simulations with the lungs present, or in the homogeneous torso, this appears to have a relatively well defined peak compared with the more diffuse potential seen in those simulations. The corresponding negative potential area is more widely spread than in those cases, extending further down the torso. By frames (v) and (vi), the pattern of potential observed on the body surface is very close to that seen in the homogeneous torso, although the maxima and minima are less extreme in the frames where the blood masses are included. The blood masses also seem to act as a focus, with the peak visible in frame (v) much smaller in spatial extent than the peak which is observed in the corresponding frames both in the homogeneous torso and in the torso with lungs. This effect is much less noticeable by frame (vi) however.

The three frames (vii–ix) corresponding to the plateau and beginnings of the repolarization show a much more diffuse arrangement of potentials. The arrangement looks very similar to the corresponding frames from the homogeneous calculations.

The evolution of the body surface potential with all inhomogeneities present is shown in figure 4.6. In (iv) an isolated peak is beginning to appear over the lower right lung. This is closer to the potential distribution shown in the simulations with just blood masses included than those where lungs are present or where there is a homogeneous torso. In contrast to this, frames (v) and (vi) show a distribution of potential much closer to that seen in the simulations where lungs are present, with a larger area of negative potential than is observed in the homogeneous torso. The final stages of evolution of the P-wave body surface potential, shown in frames (vii–ix) show a diffuse pattern, similar to that seen in all the other simulations.

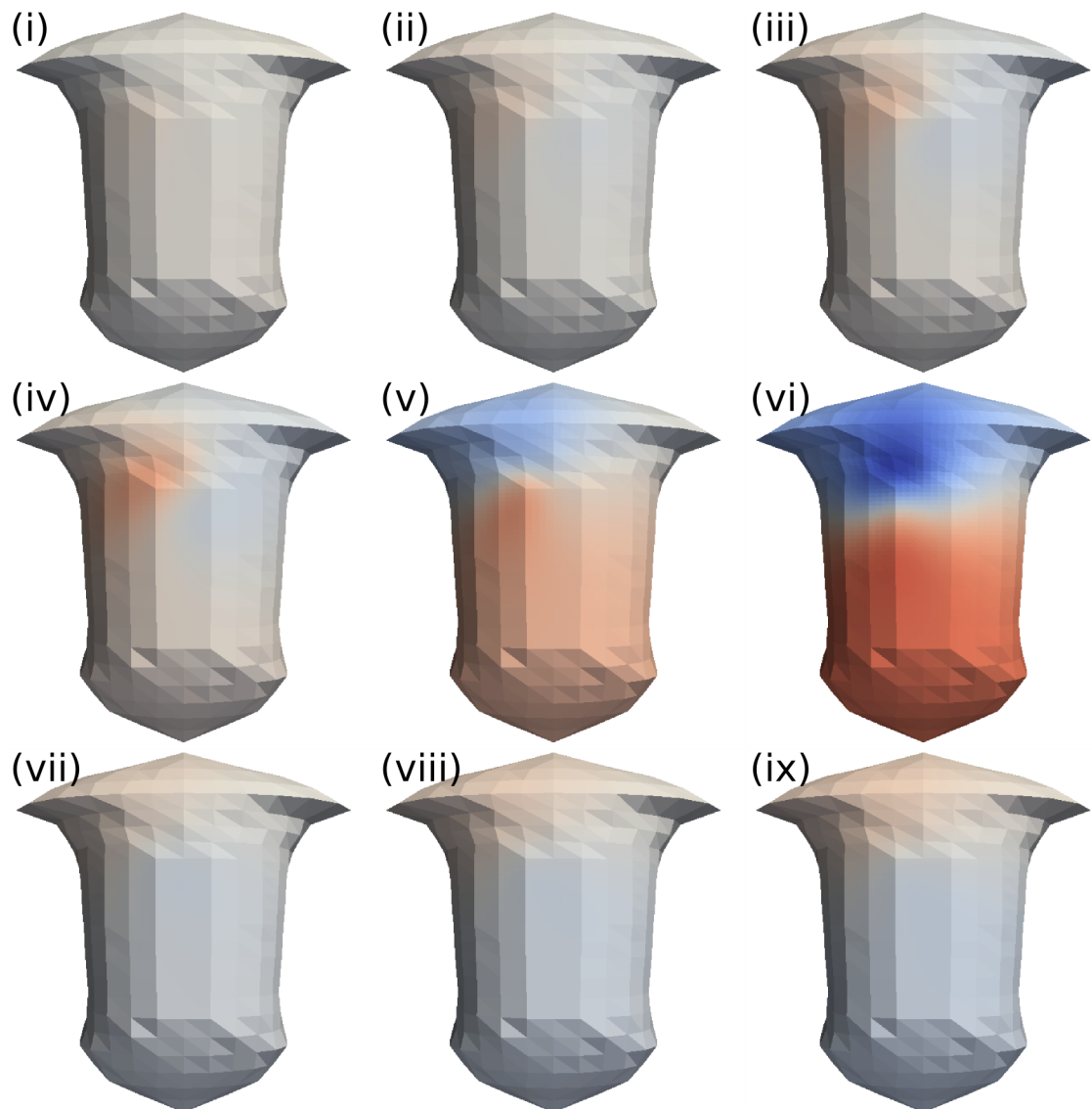


Figure 4.5: Simulated body surface potential plots during sinus rhythm with blood masses assigned conductivity from table 4.1. Blue represents negative potentials, and red positive ones, relative to the zero defined by the wilson's central terminal. The torso begins approximately isopotential before a distinct pattern of potential, with an area of negative potential over the right shoulder and an area of positive potential below. The pattern of potentials is similar to that observed in the simulation with a homogeneous torso, but it has a smaller magnitude. This pattern then reverses during repolarization. The maximum potential observed is 0.304 mV and the minimum is -0.406 mV. Snapshots shown for 10 ms (i), 15 ms (ii), 20 ms (iii), 25 ms (iv), 40 ms (v), 60 ms (vi), 180 ms (vii), 200 ms (viii) and 220 ms (ix)

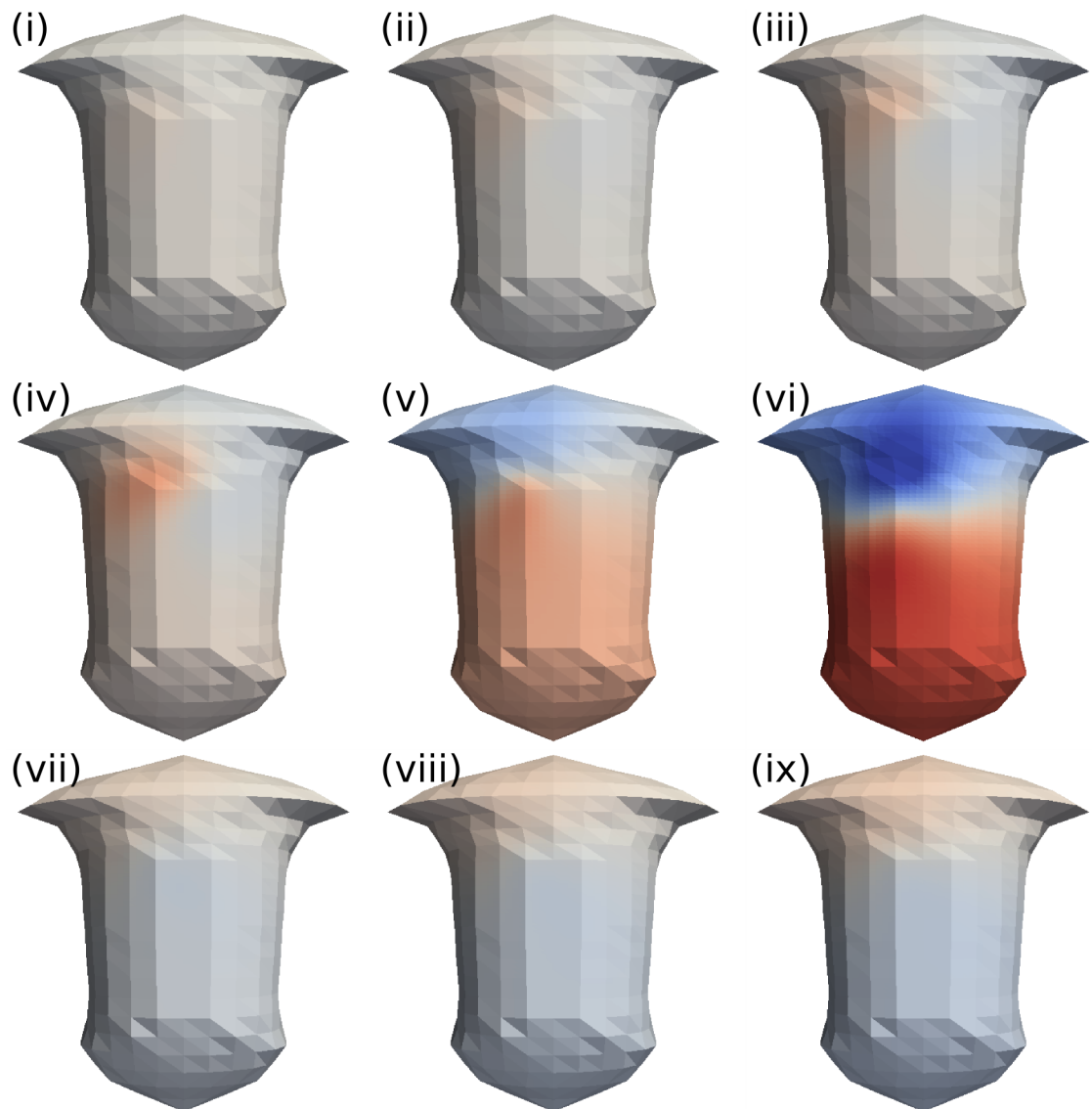


Figure 4.6: Simulated body surface potential plots during sinus rhythm with all inhomogeneities assigned conductivities from table 4.1. Blue represents negative potentials, and red positive ones, relative to the zero defined by the Wilson's central terminal. The torso begins approximately isopotential before a distinct pattern of potential, with an area of negative potential over the upper right lung and an area of positive potential below it. This pattern then reverses during repolarization. The maximum potential observed is 0.359 mV and the minimum is -0.465 mV. Snapshots shown for 10 ms (i), 15 ms (ii), 20 ms (iii), 25 ms (iv), 40 ms (v), 60 ms (vi), 180 ms (vii), 200 ms (viii) and 220 ms (ix)

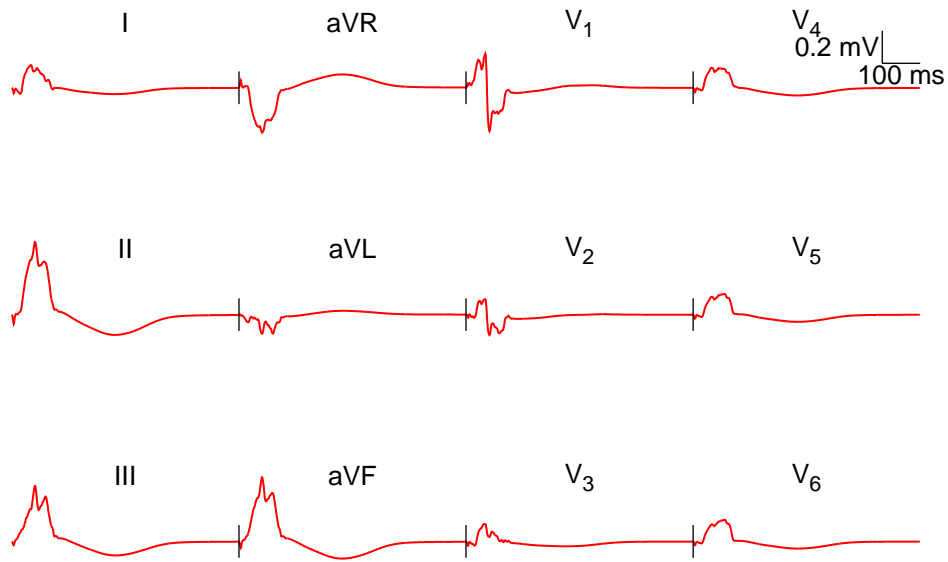


Figure 4.7: Simulated P-Wave ECG traces during sinus rhythm with homogeneous torso. One complete action potential cycle is shown. The stimulus is initiated at $t = 0$ in all traces. All traces have been smoothed with a 100 Hz low-pass filter, to simulate the typical frequency response of clinical ECG units.

4.5.2 Simulated Electrocardiograms

In this section, electrocardiograms derived from the BSP distribution are presented for sinus rhythm. All of the leads show a minor artifact during the first 2–4 ms, due to the stimulation protocol employed. Disregarding this, the following classifications are used [165]. A positive, or upright, P-wave is one that attains a potential of ≥ 0.05 mV and remains above the 0 potential baseline for duration of the P-wave. A negative, or inverted, P-wave is one that attains a potential of ≤ -0.05 mV and remains below the baseline for the duration of the P-wave. A biphasic P-wave is one that is both positive and negative, following the previous two definitions.

The ECG derived from the body surface potential simulations with a homogeneous torso is shown in figure 4.7. The P-wave has a duration of 109 ms in lead II and an amplitude of 0.466 mV. The maximum and minimum potential differences observed in the leads are +0.446 mV and -0.275 mV seen in lead II and lead aVR, respectively. The P-wave is positive in leads I, II, III, aVF and V_{3-6} . It is positive-negative biphasic in V_1 and V_2 . It is inverted in leads aVR

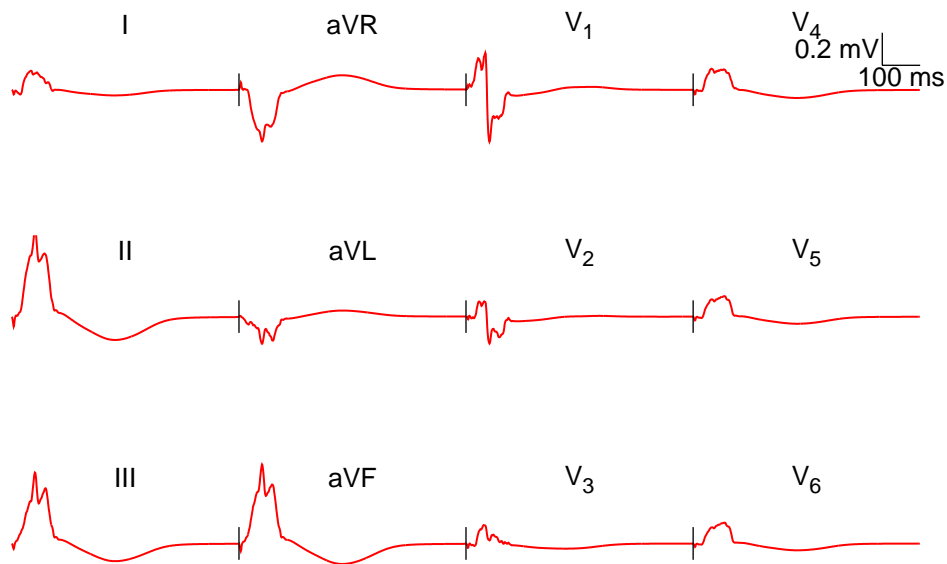


Figure 4.8: Simulated P-Wave ECG traces during sinus rhythm with inhomogeneous torso. Lungs assigned conductivity from table 4.1. One complete action potential cycle is shown. The stimulus is initiated at $t = 0$ in all traces. All traces have been smoothed with a 100 Hz low-pass filter. This is to closer emulate the frequency response of a typical clinical ECG unit.

and aVL.

The atrial repolarization wave, the T_P wave, is easily visible in most leads. It is very flat, almost to the point of invisibility, in leads I, aVL and V_{1-3} . In all the leads in which it appears, it is inverted compared to the P-wave in that lead and has a lower (less than 50% in all leads) amplitude. It appears to start immediately after the P-wave in all leads. The T_P is broader than the P-wave, corresponding to the lower speed of repolarization.

The ECG corresponding to the simulations with inhomogeneous lungs is shown in figure 4.8. The P-wave has a duration of 117 ms in lead II and an amplitude of +0.535 mV. The maximum and minimum potential differences observed in the leads are +0.535 mV and -0.319 mV seen in lead II and lead V_1 , respectively. The P-wave is positive in leads I, II, III, aVF and V_{3-6} . It is positive-negative biphasic in V_1 and V_2 . It is inverted in leads aVR and aVL. In general, the presence of the lungs appears to amplify the signal compared to the simulations without lungs.

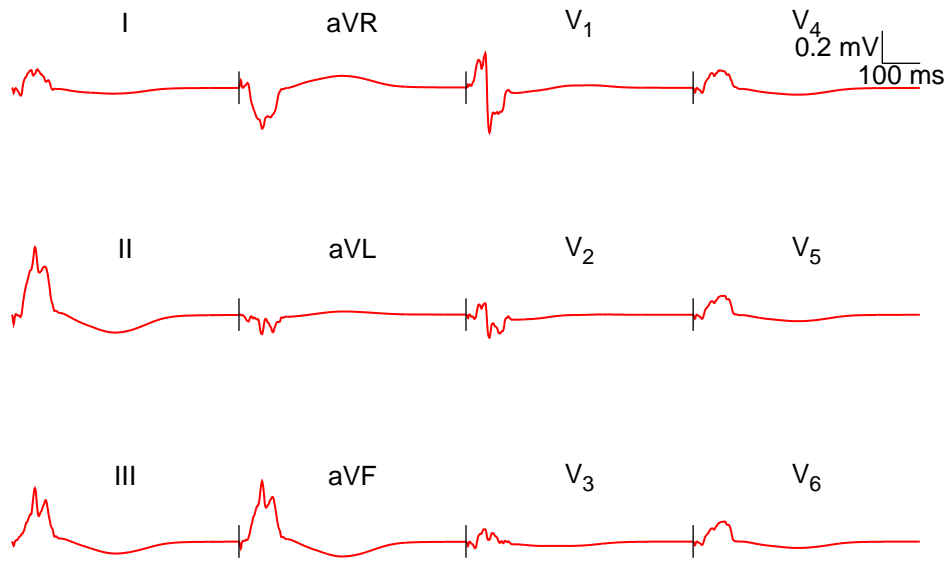


Figure 4.9: Simulated P-Wave ECG traces during sinus rhythm with inhomogeneous torso. Blood masses assigned conductivity from table 4.1. One complete action potential cycle is shown. The stimulus is initiated at $t = 0$ in all traces. All traces have been smoothed with a 100 Hz low-pass filter. This is to closer emulate the frequency response of a typical clinical ECG unit.

The T_P wave is visible in most leads, though in the leads which did not attain very high potentials (I, aVL, V_{1-3}) it is very flat. In all the leads in which it appears, it is inverted compared to the P-wave in that lead and has a lower (less than 50% in all leads) amplitude. It appears to start immediately after the P-wave in all leads. The T_P is broader than the P-wave in all leads.

The ECG corresponding to the simulations with inhomogeneous blood masses is shown in figure 4.9. The P-wave has a duration of 100 ms in lead II and an amplitude of +0.415 mV. The maximum and minimum potential differences observed in the leads are +0.415 mV and -0.275 mV seen in lead II and lead V_1 , respectively. The P-wave is positive in leads I, II, III, aVF and V_{3-6} . It is positive-negative biphasic in V_1 and V_2 . It is inverted in leads aVR and aVL. The presence of the bloodmasses generally acts to reduce the amplitudes of the P-wave ECG.

The T_P wave is visible in most leads, though in the leads which did not attain very high potentials (I, aVL, V_{1-3}) it is very flat. In all the leads in which it

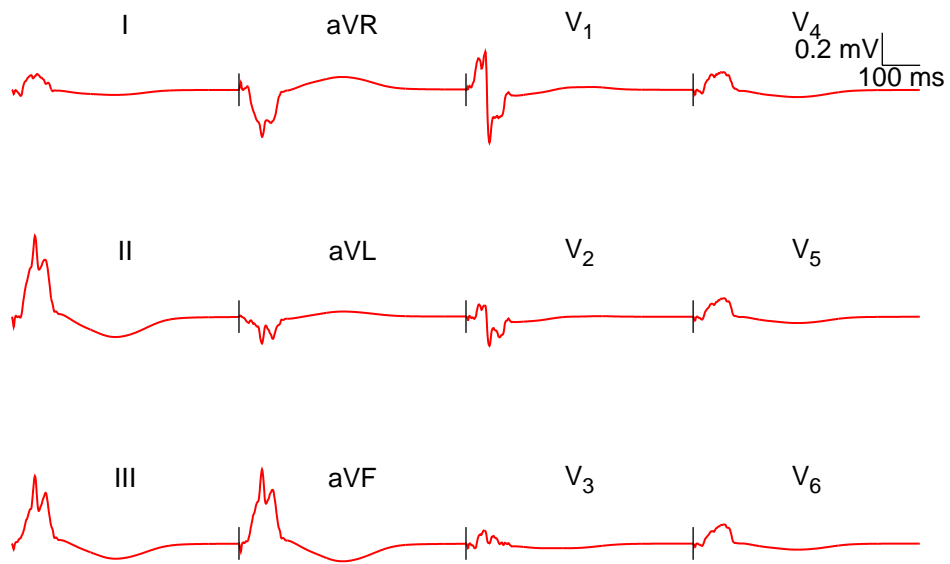


Figure 4.10: Simulated P-Wave ECG traces during sinus rhythm with inhomogeneous torso. Lungs and blood masses assigned conductivity from table 4.1. One complete action potential cycle is shown. The stimulus is initiated at $t = 0$ in all traces. All traces have been smoothed with a 100 Hz low-pass filter, a typical upper limit of frequency response in clinical ECG machines.

appears, it is inverted compared to the P-wave in that lead and has a lower (less than 50% in all leads) amplitude. It appears to start immediately after the P-wave in all leads. The T_P is broader than the P-wave in all leads.

The ECG corresponding to the simulations with all inhomogeneities considered is shown in figure 4.10. The P-wave has a duration of 103 ms in lead II and an amplitude of +0.497 mV. The maximum and minimum potential differences observed in the leads are +0.497 mV and -0.325 mV seen in lead II and lead V_1 , respectively. The P-wave is positive in leads I, II, III, aVF and V_{3-6} . It is positive-negative biphasic in V_1 and V_2 . It is inverted in leads aVR and aVL. When the blood masses and the lungs are both present, the resulting ECG is a mixture of the effects of both sets of inhomogeneities. This results in an ECG which generally has lesser amplitudes than those observed in the simulations where only the lungs are present, though greater than the magnitudes where there is just the torso.

The T_P wave is visible in most leads, though in the leads which did not attain

Table 4.2: Maximum and minimum potentials observed in the twelve leads of the ECG for differing inhomogeneities considered. Torso corresponds to the homogeneous case, lungs to the case where the lungs are given a conductivity from table 4.1, blood to case where the blood masses were assigned the conductivity from table 4.1 and all, for when both lungs and blood masses were assigned differing conductivities. For upright and inverted leads, only one potential is given, the maximum or minimum potential observed, respectively. For biphasic leads, both the maximum and minimum potentials are given. All values in mV.

Lead	Torso	Lungs	Blood	All
I	+0.139	+0.117	+0.113	+0.097
II	+0.446	+0.535	+0.415	+0.497
III	+0.341	+0.435	+0.328	+0.414
aVR	-0.275	-0.317	-0.251	-0.290
aVL	-0.118	-0.167	-0.121	-0.165
aVF	+0.394	+0.485	+0.372	+0.455
V ₁	+0.208 / -0.265	+0.227 / -0.319	+0.211 / -0.275	+0.233 / -0.325
V ₂	+0.095 / -0.125	+0.093 / -0.166	+0.068 / -0.142	+0.075 / -0.180
V ₃	+0.109	+0.113	+0.076	+0.080
V ₄	+0.123	+0.129	+0.108	+0.108
V ₅	+0.127	+0.125	+0.116	+0.113
V ₆	+0.133	+0.128	+0.122	+0.116

very high potentials (I, aVL, V₁₋₃) it is very flat. In all the leads in which it appears, it is inverted compared to the P-wave in that lead and has a lower (less than 50% in all leads) amplitude. It appears to start immediately after the P-wave in all leads. The T_P is broader than the P-wave in all leads, corresponding to the lower speed of repolarization.

A summary table of the maxima or minima of the leads is shown in table 4.2.

The phase of the signal, that is whether it is rising or falling, does not seem to be influenced by the presence or absence of inhomogeneities [67, 166], only the amplitude. However, the influence of the inhomogeneities in each lead is not equal, with some leads being increased and others decreased. This suggests that the inhomogeneities might have greater importance in the atria, possibly due to the lower mass of atrial tissue and its thinner walls.

4.5.3 Comparisons with Clinical Studies and Information

Opinions vary on what is considered a ‘normal’ P-Wave ECG [53, 167, 168]. All sources agree that the P-wave should be positive in leads I, II, aVF and V_{4–6} and negative in aVR which the model shows. Lead III is considered normal if it is positive or biphasic. None of the three sources agree on the orientation of a normal P-wave in aVL, but a negative P-wave is considered acceptable. Leads V_{1–3} are considered normal if they are positive in some of the sources, but others suggest they should, or can be biphasic. The generated ECGs therefore seem to lie within the normal limits for their basic phase relationships.

Another notable feature is the presence of the T_P in many of the leads, which is not normally observed in clinical ECG recordings. Its presence in the traces generated by this model is due to a combination of factors. The first and most obvious reason is that the traces produced by the model are a lot ‘cleaner’ than those recorded clinically since there are no problems due to RF interference from wiring, or skeletal muscle activation. They are also scaled appropriately to view the P-wave, which has an amplitude which is approximately an order of magnitude smaller than the QRS-complex which most 12 lead systems are scaled to view. There is also the lack of the QRS complex, which often obscures the T_P wave.

Macfarlane and Lawrie [169] give the P-wave duration in lead II for males and females in various age groups. Due to the hybrid nature of the model, it is hard to know which group gives the most accurate comparison. The P-wave duration for the fully inhomogeneous model of 103 ms gives good agreement with both the 104 ± 12.9 ms reported for a females of ages 40–49, which is the age of the heart and with the 103 ± 14.2 ms figure reported for males of age 18–29, the age of the torso. They report the maximum P-wave potential in lead II to be approximately 0.23 mV. The maximum potential observed in the fully heterogeneous case is +0.497 mV. In general, the amplitudes in all leads fall outside the maxima observed in the clinical data. This is expected [67, 74, 78, 166] as internal inhomogeneities tend to reduce the observed potentials as they ‘smear’ the electrical signal out over the torso.

Clinical BSPM data for the P-wave has been taken by Taccardi [163] and Mirvis [164]. A comparison of the data taken by Mirvis is shown in figure 4.11. They presented a ‘typical case’ from their study of 40 individuals. The BSPM generated by the combined atrial and torso model shows quite good agreement with the experimental BSPM recorded by Mirvis. The BSPM starts off almost

isopotential with a single positive peak. This then grows in both physical extent and magnitude, moving towards the middle of the precordial leads. At 48 ms there are two distinct negative and positive regions, with a single peak. This peak then moves off to the left, over the precordial leads. As the P-wave ends, there is a single negative peak, sitting over leads 1 and 2. Apart from the obvious, that of amplitude differences, the Mirvis study does differ slightly from the model. In general the model's peaks are slightly to the left of those which Mirvis observed. In addition, the Mirvis BSPM seems to suggest a P-wave axis which is rotated slightly, with the zero line sloping upwards from right to left (in the body's sense), rather than the almost horizontal line observed in the plots from the model. However, the essential properties of the Mirvis data are reproduced. The positive and negative regions are single peaked and a very similar evolution of potentials is observed.

4.5.4 Comparisons with other Modelling Studies

Modelling studies of the P-wave BSP are relatively rare in the literature with the vast bulk of studies concerning themselves with the ventricles. There have been several studies [72, 73, 170, 171] which have considered the generated P-wave. These studies represent a range of approaches to the problem.

The Lian et al. [170] study used the Weixue [70, 71] torso geometry as in this study. Their source model was based on atrial geometry extracted from the original CT images the torso surface was also based on. It was discretised at a resolution of 1.5 mm. Electrical activation of each of the 65,000 nodes was determined using a rule based [70] system, similar to cellular automata, although a full electrophysiological model was used at each point. The activation sequence of the nodes is predetermined and there is no direct coupling between cells. For calculation of the BSP, the nodes are assigned to one of 29 dipole blocks. The Lian et al. model is very simplistic, but can never-the-less reproduce the broad detail of the P-wave BSPM. They see a similar distribution of potential, although their maps show a very simple distribution of potential without the complexities visible in both the BSPMs generated by the model described in this chapter and seen in the data from Mirvis [164].

Seger et al [73] used a finite element approach to compute the P-wave BSPM in both sinus rhythm and with clockwise and counter-clockwise AF. Their atrial model and the torso model were extracted from MRI data. Propagation in the

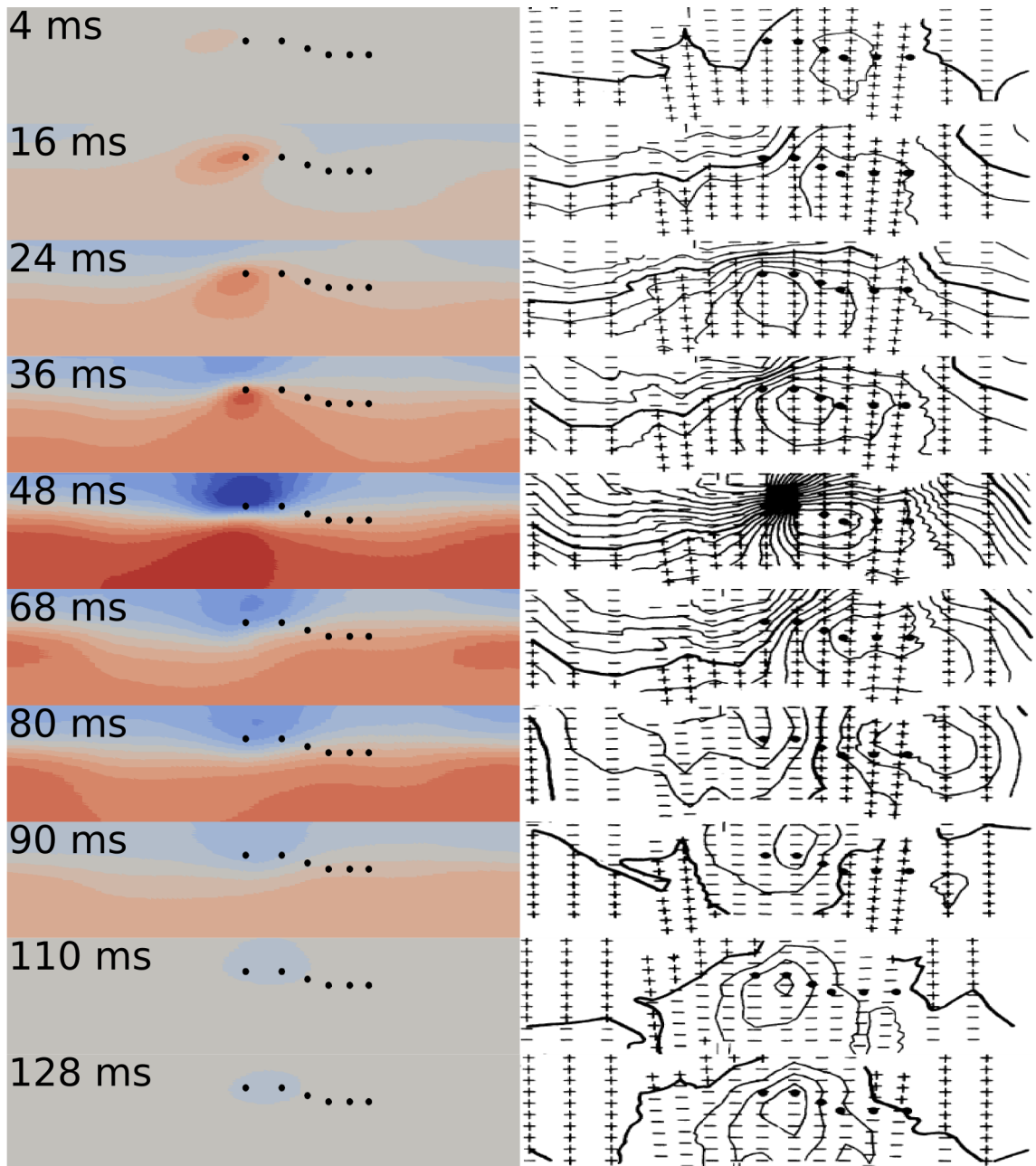


Figure 4.11: BSPMs generated by the combined torso and heart model (left) compared with clinical BSPM data recorded by Mirvis [164] (right). Precordial leads are shown as black circles (both sides). On the left, red indicates increasingly positive potentials, blue increasingly negative and Grey indicates a potential near zero. On the right, + and - signs indicate regions of positive and negative potentials, respectively. Zero potential is the bold contour, other contours in 0.01 mV intervals. All potentials relative to the Wilson's Central Terminal. The snapshots of the BSPM are from the indicated times, relative to the start of the P-wave. Right hand panels adapted from Mirvis [164], figures 2–4.

atrial model used a 3 state cellular automaton model for the membrane potentials, but used a complex distribution of conduction velocities. Calculation of the BSPM considered heterogeneous lungs and blood masses, as well as anisotropic conduction within the atria itself. Their P-wave duration and BSPM show a very similar distribution of potentials to that observed in this chapter. They report that the maximum and minimum potentials observed are approximately 0.25 mV and -0.25 mV respectively—similar in magnitude to those observed in this model, although closer to the normal limits. The use of a cellular automaton model would make simulation of ischaemia, genetic mutation or atrial fibrillation induced remodelling problematic.

Oosterom et al. [171] used a technique called the Equivalent Double Layer [172] (EDL). Briefly, this technique uses Gauss' Theorem to represent the dipole generated by the whole atria using the voltage distribution on the surface of the atria. The validity of this technique under all conditions has been questioned both theoretically [173, 174] and experimentally [175]. Their torso and atria are based on MRI data. The atrial model is generated from the endocardial surface of the atria. The atrial walls are then assumed to have a uniform thickness of 2 mm, extending out from the endocardial surface in all directions, which may not be an ideal approximation [6]. Membrane kinetics within this volume use a modified version of the Courtemanche et al. [16] model, modified to have a shorter APD₉₀ which was optimized based on recorded potentials from the patient who provided the MRI geometry. They do not present BSPMs from their simulations, though their optimized results show very close agreement with the recorded clinical ECGs from the study.

Van Dam et al. [72] also use the EDL for their BSP calculations. They used a similar model that of Oosterom et al. [171], though in this case it was entirely derived from one patients MRI dataset. They used the model to investigate the effects of including or removing internal inhomogeneities. They noticed different effects (both qualitatively and quantitatively) on the ECG leads to the study in this chapter. This is most significant in the influence of the blood masses. The reasons for these differences are unclear due to the complexities of both of the involved models. One possible reason is the difference in the relative size of the atria to the various inhomogeneities. The van Dam model has a much lower atrial tissue mass as it has walls of uniform thickness, whilst the anatomical model used in this chapter has non-uniform walls which are generally thicker than 2 mm. In

addition, the bloodmasses used in the van Dam model are two continuous regions of raised conductivity, whilst there are four such regions in the model developed here. However, they agree in the need for the inclusion of such inhomogeneities.

4.6 Limitations of the Model

Whilst the presented model of the human atrium and torso provides a relatively good reproduction of the features of the body surface potential distribution and ECG, it does omit several factors that could be considered. There were also compromises made due to the ‘assembled’ nature of the model. It is possible that a ‘better’ orientation for the atrium could be found, due to the scarcity of anatomical landmarks present in the torso for the study to guide its placement. The model of the blood masses, particularly those of the atria could be improved to more realistically model the shape, perhaps by basing the outer surface of the blood masses off a mesh extracted from the epicardial surface. The size and shape of the ventricular bloodmasses, whilst extracted from the internal surfaces of the ventricular mesh associated with the torso, do not exactly correspond to the sizes of the atrial valve openings. In addition, the presence of the lungs presented a constraint on the location of the atria, due to a requirement that the atrium should reside wholly within the main torso cavity—an orientation that had previously been considered ‘good’ had to be discarded when lungs were introduced.

The model considers only a few internal inhomogeneities, the lungs and the blood masses. Other inhomogeneities such as the skeletal muscle layers and subcutaneous fat have not been included, although previous simulation studies suggest their influence is small [74]. However the smaller mass of the atria might make their influence more significant [72] and so this factor might need further investigation. In addition, the anisotropic nature of cardiac muscle was only considered during the calculations of the electrical propagation, it was not considered during the computation of the dipole sources of the heart. What influence this has is unknown, as only one computational study of the atrial excitation appears to have considered it [73] and then not in isolation.

The model considers coupling only in one direction; the heart potential distribution drives the torso potential distribution. A more complete study might consider coupling in the other direction as well. This would require significant changes to the model, necessitating a bidomain approximation to be used for

the propagation and a finite difference or finite element formulation used for the torso.

Finally, the model is completely static. There is no consideration of the contractile nature of the myocardium. This would have influence both on the pattern of propagation and the distance between dipole locations and the boundary elements. The contractile cycle would also influence the spatial distribution of the blood masses. This would significantly increase the amount of computational power required to solve the problem, but would not be impossible with the current generation of computers.

4.7 Conclusions

A model capable of reproducing the P-wave body surface potential has been produced. The model is based on a realised atrial geometry which includes both anisotropic conduction and heterogeneous electrophysiology. The atrial model is embedded in a torso which was derived from CT images. The torso features regions of inhomogeneous conductivity, representing the blood masses of the heart and the lungs. The effects of including or removing these inhomogeneities has been investigated. Their presence is found to generally improve the quality of the generated ECG, making the generated potentials closer to physiological values. The complete model has been validated by comparison with both other computer models and with clinical data.

The model is the start of a tool for investigating many diseases of the atria and the effect they have on the ECG and BSPM. Since it is based on the Courtemanche atrial myocyte model, a biophysically detailed second generation model, it can be used for the investigation of a broad spectrum of effects, including both conduction defects and the complex electrophysiological changes induced by both genetic mutation and atrial fibrillation.

Chapter 5

Applications Of The Forward Problem

The ECG is the first tool cardiac physicians turn to when diagnosis of a problem is required. A model of the atria and the surface potentials developed by the excitation of the model can be used to correlate ECG profiles to cardiac function in a variety of conditions. This can provide more details about the direct link between ECG indices and cardiac arrhythmia or other dysfunction.

While inverse solutions promise to reproduce the excitation sequence of the heart from the recorded potentials on the surface, the technique has serious limitations. For accurate solutions, patient specific geometries have to be constructed from MRI scans. There is also a need for complex lead systems, sometimes featuring more than two hundred leads. Also, many of the inverse techniques rely on ‘smooth’ propagation patterns to reduce the uncertainties in the technique which may not be found in pathological cases. A device which can perform such calculations automatically is a long way off, both in terms of computational power required and complexities to resolve.

By contrast, diagnostic guides based on a forward solution can be of use to any doctor. They can also be used to further validate simulation studies of genetic or diseased conditions, by comparison of the generated ECGs with those recorded from real patients. This chapter explores some of these predictions, using the model developed in the previous chapter.

5.1 Focal Atrial Tachycardia

Atrial Tachycardias are one of the rarer forms of supraventricular tachycardia. They account for approximately 10% of diagnosed supraventricular tachycardias and tend to occur as a result of other cardiac or respiratory diseases. They are characterised by a high heart rate (≤ 250 bpm) and typically have evidence of an abnormal cardiac axis or P-wave morphology [53, 167, 176]. They are hard to treat with drugs, but radiofrequency ablation can be used with a high probability of success. Diagnosis of atrial tachycardia, and focus, can be difficult due to a lack of research data. Attempts to locate the sites of the ectopic focus are current topics of clinical research [165, 177, 178]. In this part of the study, I investigated possible correlations between P-wave ECG profiles and variation in ectopic focal site.

5.1.1 Model of Focal Atrial Tachycardia

To simulate focal atrial tachycardia, the model developed in Chapter 4 was used. The model was paced from a number of sites located around the atria, close to common foci of focal point tachycardia. The sinus node of the model was not stimulated. These sites are shown in figure 5.1. Their anatomic locations are summarised in table 5.1. All the nodes which have active cells within 10 cells (3.3 mm) are excited via direct current injection of 2 nS for 2 ms. The resulting excitation wave is then allowed to propagate without interference and the BSPM, ECG and derived VECG calculated. The algorithm developed by Kistler et al. [165] is applied to the 12 lead ECG and the origin of the focal point tachycardia estimated.

5.1.2 Results

Twelve Lead ECG

Pacing the atria from different sites results in a dramatic variability in the observed waveforms of the P-wave ECG. The ECGs corresponding to the stimuli are shown in figure 5.2. The classifications of the waveforms are shown in table 5.2. Classifications consider only the P-wave and not the T_P wave. In the case of more than two significant deflections, the largest two are chosen. The effect of any electrical flow is exaggerated by the large P-wave magnitudes previously noted and

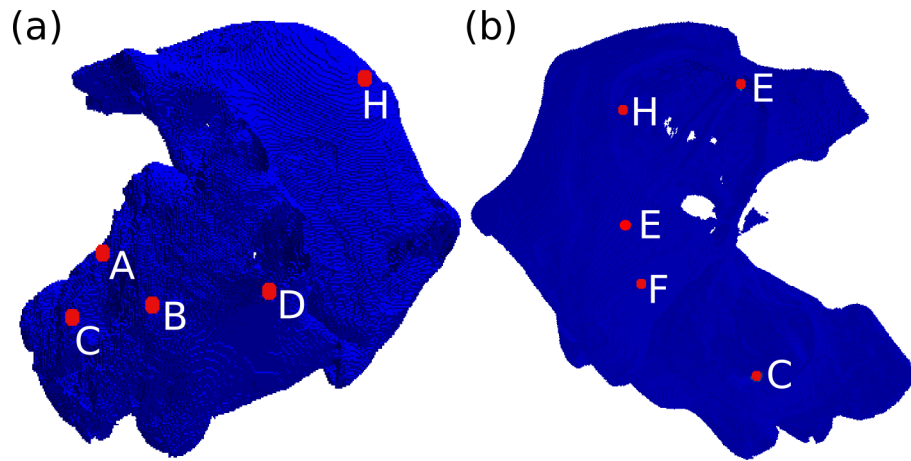


Figure 5.1: Pacing sites used assessment of the Kistler et al. algorithm. The pacing centres are indicated by red dots. Note that sites are often on the interior of the atria at the indicated locations, or embedded in the wall.

(a) View of the pulmonary veins. (b) View of up through the valve openings.

Table 5.1: Anatomical locations of the pacing sites chosen for the study. Abbreviations: AA = atrial appended, PV = pulmonary vein, TA = tricuspid anulus, CS = coronary sinus, S = septum, CT = crista terminalis. L and R denote left and right, respectively.

Site	Origin
A	LPV
B	LPV
C	LPV
D	RPV
E	RAA
F	CS
G	LS
H	CT

Table 5.2: Lead classification after pacing from sites along the crista terminalis. Leads are classified based on the criteria used by Kistler et al. [165]. A positive P-wave is denoted by a + sign, a negative P-wave by a - sign and a isoelectric (no significant positive or negative component) one by ~. In the case of a biphasic wave, it is classified based on the polarity of the two component waves, separated by a slash. Site denotes the pacing site as illustrated in figure 5.1. Site S denotes pacing from the sinus node, and is provided for comparison.

Site	I	II	III	aVR	aVL	aVF	V ₁	V ₂	V ₃	V ₄	V ₅	V ₆
S	+	+	+	-	-	+	+/-	+/-	+	+	+	+
A	-	+	+	-	-	+	+/-	+	+	+	+	+
B	-	+	+	-	-	+	+	+	+	+	+	+
C	+/-	-	-/+	+	+/-	-/+	+	+	+	-	-	-
D	+	-/+	-	-	+	-	+	+	+	+	+	+
E	+	+	+	-	-	+	-	-	-/+	+	+	+
F	+/-	-	-	+	+	-	-/+	-/+	-	-	-	-
G	+	-	-	+	+	-	~/+	-/+	-	-	-	-
H	+	+	-/+	-	+	+	+/-	+/-	+	+	+	+

so it is likely that with correct magnitudes in the P-waves, these lesser deflections would not show.

Pacing from site A, shown in figure 5.2(a), results in a P-wave which is positive in most leads. The P-wave is positive in leads II, III, aVF and V₁₋₆. It is negative in leads I, aVR and aVL. The sharp negative spike visible in V_{1, 2} at approximately 110 ms is caused by the faster conduction along the pectinate muscles, which are in places disconnected from the main wall of the atrium. This causes brief high voltage ‘islands’ to appear ahead of the main waveform, which generate dipoles of opposing sign to the main waveform. This isn’t a problem under sinus rhythm, which shows a much more regular excitation of the pectinate muscles due to the differing origin of excitation. In addition, the excitation wave front has just started to loop back around the inferior vena cava, travelling away from the frontal precordial leads. Many of the limb leads show a quite ragged profile, and are slightly bifid.

Pacing from site B, shown in figure 5.2(b), results in a P-wave which is positive in most leads. The P-wave is positive in leads II, III, aVF and V₁₋₆. It is negative in leads I, aVR and aVL. All of the inferior leads (II, III and aVF) are smooth

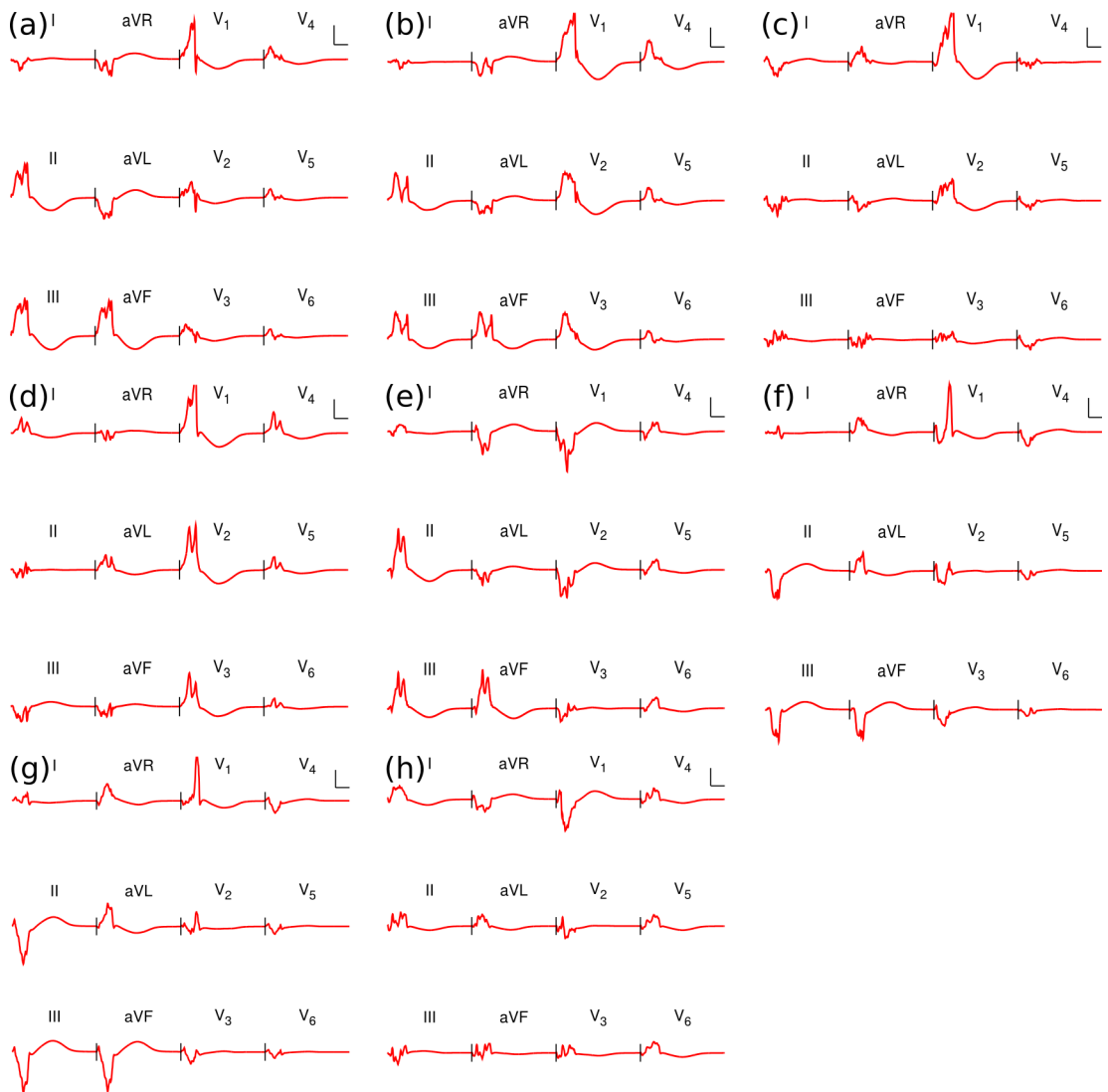


Figure 5.2: Shown is one complete P-wave and T_P wave, associated with each of the pacing sites A–H (table 5.1). Scalebars are shown for each figure. The vertical scale bar is 0.2 mV, the horizontal 100 ms.

but highly bifid. This occurs as the P-wave depolarises first down the left atrium and then the right, away from the left limb lead electrode. After the initial depolarisation of the left atrium from the top and right, towards the left, much of the excitatory activity is parallel to the lateral precordial leads (V_{4-6}).

Pacing from site C, shown in figure 5.2(c), results in a P-wave which is relatively flat. The P-wave is positive in aVR and V_{1-3} . It is negative in leads II and V_{4-6} . It is biphasic in leads I, III, aVL, aVF. The signal in all leads, though especially III, aVF and V_4 is highly variable. This is due to an uneven propagating wavefront, caused by the anatomical obstacles.

Pacing from site D, shown in figure 5.2(d), results in a P-wave which is mostly positive. The P-wave is positive in leads I, aVL and V_{1-6} . It is clearly bifid in all the leads it is positive in, except lead V_1 . The P-wave is negative in leads III, aVR and aVF. It is bifid in both III and aVR. The ECG is biphasic in lead II.

Site E is shown in figure 5.2(e). The P-wave is positive in lead I, II, III, AVF and $V_{5,6}$. The P-wave is negative in lead aVR, aVL and V_{1-3} . The P-wave is biphasic in lead V_4 . It is bifid in the positive leads II, III and aVF and in the negative leads aVR, aVL and $V_{1,2}$. The P-wave is smooth in most leads, aside from the bifidity. The electrical excitation is spreading down and slightly to the left of the body, leading to the very positive potentials observed in the inferior leads, and the positive potentials in leads V_{4-6} . The negative potentials in leads $V_{1,2}$ suggest a spread of excitation anterior to posterior.

Pacing from site F, figure 5.2(f), produces predominately negative P-waves. The P-wave is positive in leads aVR and aVL. It is negative in leads II, III, aVT and V_{3-6} . It is biphasic in leads I, V_1 and V_2 . The P-wave is generally quite clean in all the leads, although it shows significant oscillation at the end of the P-wave in leads II, III and aVF. This is likely causes as the excitation wave which is spreading up the right atrium encounters the complex anisotropy of the junctions between the crista terminalis and the pectinate muscles.

Pacing from site G, shown in figure 5.2(g), produces a predominately negative P-wave. The P-wave is positive in leads I, aVR and aVL. It is negative in leads II, III, aVF and leads V_{3-6} . It is biphasic in leads V_1 and V_2 . The negative leads V_{3-6} are indicative of a left atrial pacing site, with the excitation mostly spreading away from the left. The positive P-wave in leads aVR and aVL, combined with the negative P-waves in leads II, III and aVF, suggest the excitation is at the base of the heart and is spreading upwards. The lead traces are generally clean.

Table 5.3: Classification of the origin of focal point tachycardia according to the algorithm developed by Kistler et al. compared with the actual anatomic location. Where the algorithm presents multiple sites as a possibility, both are given. Abbreviations: AA = atrial appended, PV = pulmonary vein, TA = tricuspid anulus, CS = coronary sinus, S = septum, CT = crista terminalis. L and R denote left and right, respectively.

Site	Predicted	Origin
A	CT	LPV
B	LAA / LPV	LPV
C	RPV	LPV
D	RPV	RPV
E	RAA / TA	RAA
F	CS os / LS	CS
G	CS os/ LS	LS
H	CT	CT

Site H, figure 5.2(h), produces jagged P-waves. The P-wave is positive in leads I, II, aVL and V₄₋₆. The P-wave is negative in lead aVR. The P-wave is $-/+$ biphasic in leads III, aVF and V₃. It is $+/-$ biphasic in leads V₁ and V₂. Leads II, V₄ and V₅ are bifid. In addition, leads aVF and V₃ are very bifid in appearance, although the trough becomes negative enough to classify them as biphasic.

Application of the Focus Location Algorithm

The algorithm developed by Kistler et al. was applied to the P-wave morphologies generated by the model. The algorithm is presented as a simple decision tree, initially concerning the morphology of lead V₁. The results of applying the algorithm and the actual anatomical locations are shown in table 5.3.

5.1.3 Discussion and Conclusion of Focal Atrial Tachycardia Study

The simulation results show very good agreement with the focal tachycardia location algorithm developed by Kistler et al. The algorithm, when used on the P-wave ECGs produced by the model, correctly estimated the origin of the focal

point tachycardia in six out of the eight cases considered. In addition, one of the errors (case C), is only mistaking between the left and right pulmonary veins. This is encouraging as it acts as a validation of both the model and the algorithm.

The study also highlights some of the limitations of the model. The most significant of these is the large amplitudes of the P-waves, due to the nature of the inhomogeneities considered and the underlying cardiac model. Because of this larger amplitude, several fluctuations that perhaps should be considered minor are instead classified as full deflections due to the 0.05 mV threshold. This is especially evident in case A which is incorrectly classified by the algorithm as originating from the crista terminalis. This is due to the presence of the negative spike in lead V₁. The spike has a magnitude of approximately 0.1 mV which causes the lead to be classified as having a positive–negative morphology. The algorithm classifies all such P-waves as having a crista terminalis origin. If the spike were of a reduced amplitude, the positive V₁ and other lead morphologies leads to a classification of LAA or LPV, the correct answer.

It is also possible that the size of the stimulus zone should be decreased. The effect of the localised and very rapid potential change along the border of the stimulus zone can generate a large spike at the start of the pacing cycle. This is due to the rapid ($> 200 \text{ mVs}^{-1}$) upstroke of the Courtemanche et al myocyte model used as the basis of the anatomical atrial model. A smaller stimulus zone should reduce this artefact, which is sometimes difficult to separate from the ‘real’ P-wave.

It should be emphasised, however, that the large amplitudes of the P-wave was only an issue in case A. The location of the focal point tachycardia was correctly predicted by the algorithm in most cases. This prediction would not be affected by a reduction in amplitude of all the lead potentials. The model therefore correctly reproduces the phase information of the P-wave ECG, which is ultimately what the location algorithm depends on.

The Kistler et al. algorithm appears to be the best algorithm one is aware of in the literature that uses the standard twelve lead ECG. It would be interesting to compare the predictive accuracy of the algorithm with one devised using the model and the so called ‘Atrial ECG’ proposed by Ihara et al [62]. Such a study would require a family of similar models to be developed, based on several torso and atrial geometrical models.

No discussion of an algorithm of this nature would be complete without a

discussion of inverse techniques. Inverse techniques have developed considerably over the previous two decades. Ramanathan et al. [61] have developed a technique which they call Electrocardiographic Imaging (ECGI) and several groups have similar efforts as well. These techniques allow calculation of the epicardial potentials from external measurements. These inverse techniques require a significant amount of effort to set up, however. The ECGI technique proposed by Ramanathan et al. uses a 224 electrode vest and requires the construction of a heart-torso geometry from CT scans. By contrast, algorithms devised for twelve lead sets can still be highly accurate and are available everywhere.

The Kistler et al. model can correctly predict the location of ectopic foci in the body surface potential model in seven of eight cases. This validates both the algorithm and the model. The model could therefore be used as the basis for further refinements to the algorithm, or the development of similar ones.

5.2 Inverted P-Waves at Night

Recently an observation was made concerning patients under 24 hour ECG monitoring (Prof. Mark Boyett, Private Conversation, 2008). It was noted that some patients exhibited inverted P-waves at night. That is to say, if the patient showed a positive P-wave in leads II and aVF during the day, then at night the P-wave would be negative in leads II and aVF. These patients had no known heart disease or conduction defects. This phenomena has not been reported in the literature.

There is evidence [133,179,180] that the pacemaker is not a small and discrete area of the atrium, but is instead distributed along the length of the crista terminalis. The presence of certain drugs and hormones, most notably acetylcholine, can cause the site of the leading pacemaker to move down the pace maker complex. Acetylcholine is released by what is known as increased ‘vagal tone’. This has been observed to happen at night.

The underlying mechanisms for the inverted P-waves at night are unknown. It was hypothesised that a pacemaker shift induced by increased vagal tone might lead to the observed P-wave inversion. In this study, I attempt to verify the hypothesis using the P-wave ECG model.

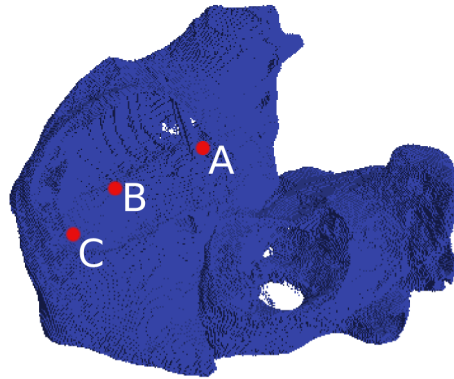


Figure 5.3: Pacing sites used for the inverted P-wave study. The view is up through the valve openings. The pacing centres are indicated by red dots.

5.2.1 Methods

In the absence of a model for the distributed pacemaker complex in the human heart, the direct effects of acetylcholine could not be investigated. Instead, using the model presented in the previous chapter, several sites were located along the crista terminalis. These sites had a radius of 10 nodes (or approximately 3.3 mm—although this varied depending on the thickness of the atrial wall at the pacing site), and therefore were approximately the same size as the sino-atrial node. These sites are shown in figure 5.3. Each of these sites was stimulated via the same protocol used to stimulate the sinus node in the original model and then the electrical excitation waves were allowed to propagate without interference.

The total activation time is calculated as the time after stimulus for all cells to become excited above -60 mV . ECGs were computed from the patterns of electrical excitation in the atrium. These were compared to the sinus rhythm ECGs computed in the previous chapter. In addition, using a so called ‘inverse Dower’ method after Edenbrandt and Pahlm [57], the orthogonal components of the ECG were computed and used to construct representations of the heart vector [55, 181] ECG (VECG). To perform the inverse dower transformation, a matrix that has been optimized for the P-wave (shown in Table 5.4) was used [182].

Table 5.4: Factors to construct the Frank VECCG from the standard 12 lead ECG set. Parameters optimised to accurately reproduce the P-wave heart vector [182]. Each of the 8 leads are multiplied by the given parameters to provide the orthogonal Frank lead.

	V ₁	V ₂	V ₃	V ₄	V ₅	V ₆	I	II
X	-0.266	0.027	0.065	0.131	0.203	0.220	0.370	-0.154
Y	0.088	-0.088	0.003	0.042	0.047	0.067	-0.131	0.717
Z	-0.319	-0.198	-0.167	-0.099	0.009	0.060	0.184	0.114

5.2.2 Results

Activation Sequence

The activation sequences of the atria after pacing from the sinus node, and the three sites along the crista terminalis are shown in figure 5.4 as isochronal colour maps. Time goes from red, at 0 ms, to blue, at 150 ms. The site of first activation obviously shifts depending on the stimulus location. In addition, as the stimulus site moves away from the sinus node, the time to total activation of the atria increases.

The sinus node activation sequence, figure 5.4(s)(i, ii), starts high on the right atrium, close to the superior vena cava. Conduction is especially rapid down the crista terminalis and along the pectinate muscles, visible as the more widely spaced isochrones along these structures. The Bachmann bundle, meanwhile, conducts the electrical excitation to the left atrium, where it then starts to spread over the left atrial endocardial surface. In the right atrium the activation finishes, approximately 80 ms after stimulation started, with the activation of the ring around the tricuspid valve and the right atrial appendage. In the left atrium, the far extremities of the left atrial appendage and the far side of the mitral valve to the Bachmann bundle are activated at approximately 120 ms, completing the activation of the atria.

The activation sequence from site A, figure 5.4(a)(i, ii), starts high on the right atrium in the region where the pectinate muscles are branching from the crista terminalis. This leads to rapid conduction down the pectinate muscles and in both directions along the crista terminalis. The Bachmann bundle conducts the excitation to the left atrium, where it starts to spread. The activation of

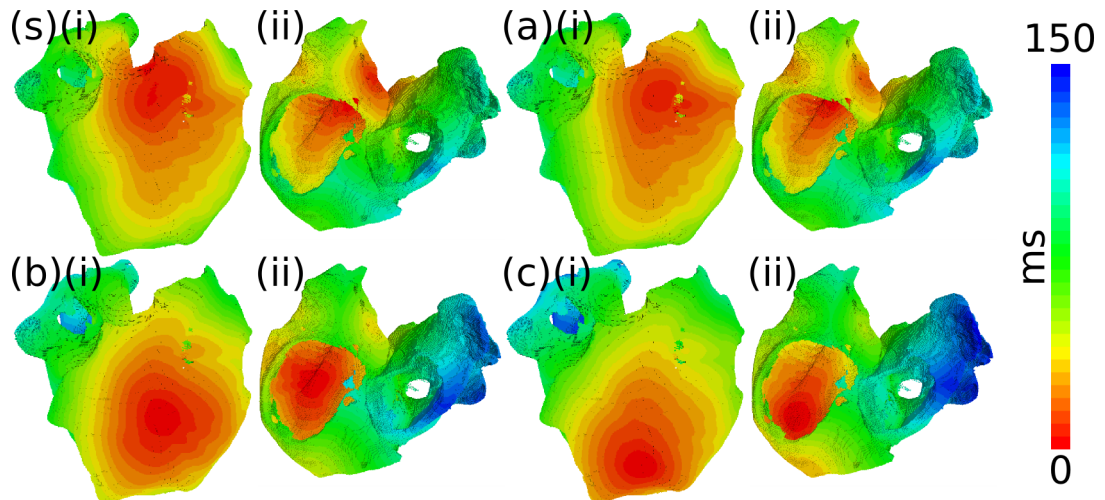


Figure 5.4: Atrial activation sequences obtained from different pacing sites. Shown are the activation sequences resulting from pacing at the sinus node, (s), and the three crista terminalis sites A–C (a–c). Activation times are represented by colours, going from red at ≤ 5 ms through green, 75 ms to deep blue at 150 ms. Contours are every 5 ms.

There are two views shown for each pacing site. (i), a view of the right atrial surface with the superior vena cava at the top of the right atrial surface and the tricuspid valve at the base. In this view, the crista terminalis runs approximately vertically. (ii), a view up into the atrial cavities through the valve openings. The ribbed structures of the pectinate muscles are visible through the tricuspid valve as they extend off the crista terminalis on the left of the panel. The right and left atrial appendages are to the top of the panels.

In panel (s) the sinus rhythm activation sequence is visible with rapid conduction along the crista terminalis and pectinate muscles. The Bachmann’s bundle meanwhile rapidly conducts the excitation to the left atrium. In both atria, the appendages are amongst the last regions to depolarise.

In panel (a), the activation sequence has shifted slightly down the crista terminalis. The pectinate muscles and crista terminalis still have a large influence on the propagation. In both atria, the appendages are the last regions to depolarise. In panel (b), the activation sequence is shifted a long way down the crista terminalis. The Bachmann’s bundle is no longer the site of first activation of the left atrium. Total time to activate is noticeably delayed.

In panel (c), the activation sequence is shifted a long way down the crista terminalis. Total time to activate is noticeably delayed in the left atrium. The Bachmann’s bundle is no longer the site of first activation, instead the area close to the coronary sinus is first activated.

the right atrium finishes with the activation of the right atrial appendage and then region between the septum and the tricuspid valve. Activation of the left atrium completes in 132 ms after the initial stimulus on the edge of the left atrial appendage and the mitral valve.

Pacing from site B leads to the activation sequence depicted in figure 5.4(b)(i, ii). The activation sequence starts lower on the crista terminalis, and is conducted in both directions along the muscle ridge. The pectinate muscles also influence the conduction, although the excitation wavefront reaches them later. Excitation still reaches the left atrium through the Bachmann bundle, although it is also conducted through the septum close to the inferior vena cava. The last region to be excited in the right atrium is still the appendage. In the left atrium, the last activation comes at 140 ms. The left atrial appendage and the sheaths of the pulmonary veins both finish activating at this time.

The activation sequence which results from pacing from site C is shown in figure 5.4(c)(i, ii). The activation sequence starts low on the right atrium and spreads in all directions, but is faster travelling up the crista terminalis. The pectinate muscles, when the excitation wave reaches them, also have a noticeable effect, speeding activation of the right atrium. Once again, the left atrium appears to be excited in two places, both by the bachmann's bundle and close to the inferior vena cava through the septum. The right atrial appendage is the last region of the right atrium to be excited. In the left atrium, the extremities of the appendage and the pulmonary vein sheaths are the last to be excited, as well as the region close to the mitral valve. The last activation comes at 144 ms.

All of the activation sequences are approximately normal, in that they travel from right to left. The further the stimulus site is removed from the sinus node, the longer excitation tends to take.

Twelve Lead ECG

The ECGs from the three pacing locations along the CT are shown in figure 5.5 with the sinus rhythm P-wave ECG for comparison. A summary of the lead deflections for the four cases and sinus rhythm are presented in table 5.5. There is a clear evolution of the P-wave morphology visible as the pacing site is moved down the crista terminalis.

The P-wave ECG for pacing from the sinus node, figure 5.5(s), is positive in leads II and aVF. Leads I, III and V₃₋₆ are also positive. Leads aVR and aVL

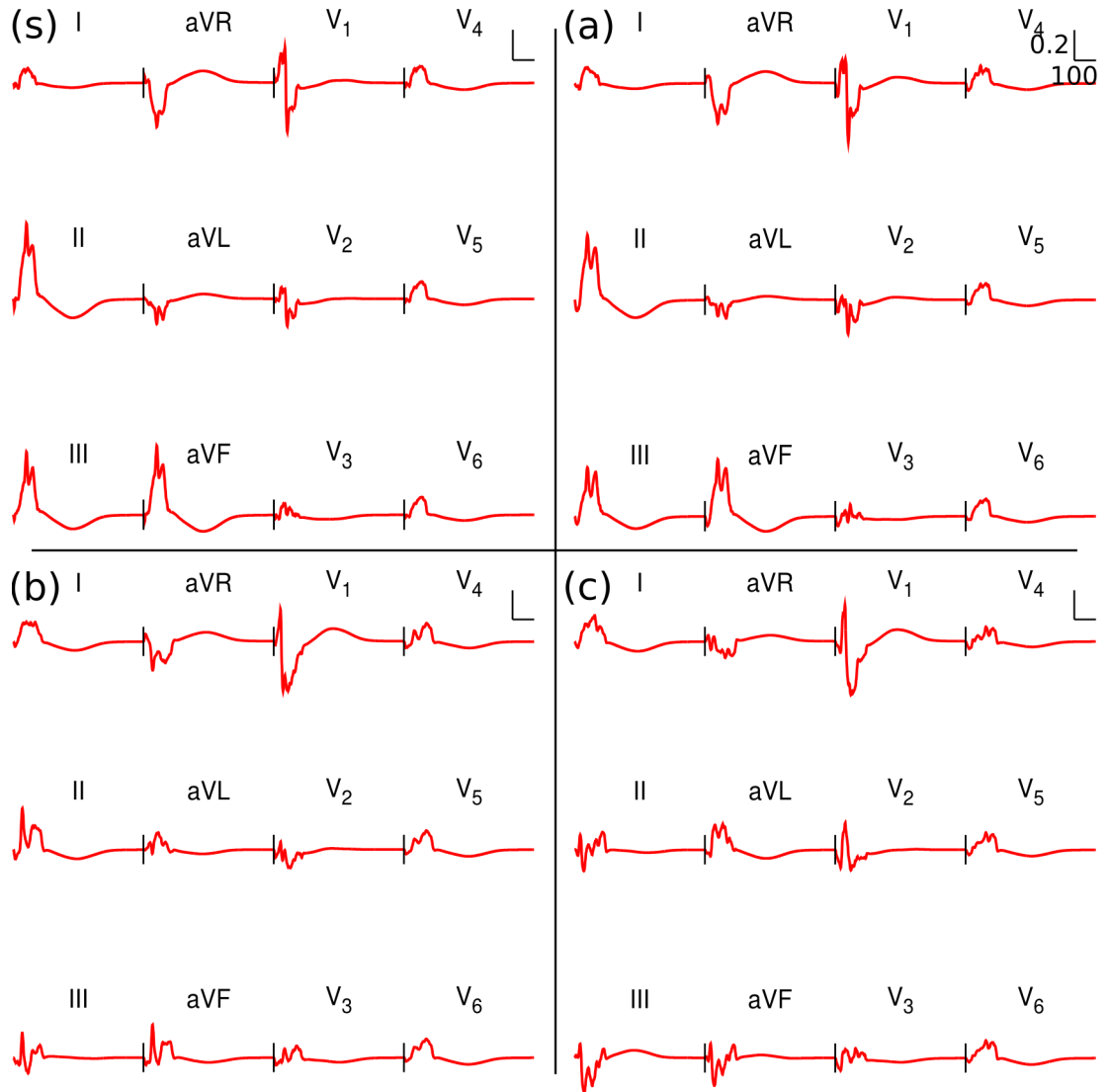


Figure 5.5: Twelve lead ECG recordings obtained from the model after pacing at the sinus node, (s) and the three pacing sites A–C (a–c). Shown is one complete P-wave and T_P wave, pacing at a rate of 60 bpm. The scale is the same for all traces, indicated in the top right of panel (a), where the horizontal scale is in ms and the vertical in mV. The P-wave is positive in leads II and aVF after pacing from the sinus node. It is positive in leads II and aVF after pacing from site A. Pacing from site B leads to a positive but highly bifid P-wave in both leads II and aVR. Site C shows negative then positive biphasic P-waves in both leads II and aVR.

Table 5.5: Lead classification of the P-wave after pacing from sites along the crista terminalis. Leads are classified based on the criteria used by Kistler et al. [165]. A positive P-wave is denoted by a + sign, a negative P-wave by a - sign. In the case of a highly bifid or biphasic wave, the signs of the two phases of the wave are indicated on either side of a slash. For example, +/+ would be a positive, bifid wave and -/+ would be a negative then positive biphasic wave. Site denotes the pacing site, where S is the sinus node and Sites A–C are as indicated in Figure 5.3.

Site	I	II	III	aVR	aVL	aVF	V ₁	V ₂	V ₃	V ₄	V ₅	V ₆
S	+	+	+	-	-	+	+/-	+/-	+	+	+	+
A	+	+	+	-	-	+	+/-	-	+	+	+	+
B	+	+/+	-/+	-/-	+	+/+	+/-	+/-	+/+	+/+	+	+
C	+	-/+	-	-	+	-/+	+/-	+/-	-/+	+	+	+

are negative. Leads V₁ and V₂ are both positive–negative biphasic. The cardiac axis is between +60° and +90° in the frontal plane. The ECG is consistent with a normal activation of the atria, spreading to the left and bottom as time evolves.

Pacing from site A (figure 5.5(a)), the P-wave ECG is positive in leads II and aVF. Leads I, III, aVF and V_{3–6} are also positive. Lead aVR, aVL and V₂ are negative. Lead V₁ is positive–negative biphasic. The cardiac axis is between +60° and +90° in the frontal plane. The ECG is consistent with a mostly normal propagation. The slightly broader negative trough on lead V₁ is due to the slightly slower depolarisation time of the left atrium. There is a prominent notch visible in several of the limb leads. This is caused by the depolarisation of the right atrial appendage and the pulmonary veins, both of which happen against the bulk direction of excitation propagation.

Pacing from site B (figure 5.5(b)), the P-wave ECG is positive in leads II and aVF, but is highly bifid. Leads I, aVL and V_{3–6} are also positive. Lead aVR is negative. Lead V₁ and V₂ are positive–negative biphasic. Lead III is negative–positive biphasic. The cardiac axis is approximately +30° in the frontal plane. The bifid morphology of the P-wave in the inferior limb leads and aVR is due to the delayed depolarisation of the left atrium, induced by the time taken to propagate up the crista terminalis. The bidirectional propagation contributes to the much lower amplitudes observed in many of the limb leads compared to the sinus rhythm.

Pacing from site C (figure 5.5(c)), the P-wave ECG is negative-positive biphasic in leads II and aVR. Leads I, aVL and V₄₋₆ are positive. Leads III and aVR are negative. Lead V₁ and V₂ are positive-negative biphasic. Lead V₃ is negative-positive biphasic. The cardiac axis is approximately 0° in the frontal plane, as the excitation wave now travels mostly across the atria. The negative-positive morphology of the P-wave in leads II and aVR are caused as the bulk direction of the excitation is first up the right atrium and then down the left atrium. The lateral precordial leads (V₄₋₆) are positive as the excitation is still travelling from right to left.

As the pacing site moves down the crista terminalis there is an evolution of the P-wave, which is visible in all leads. As a result of the shift, the cardiac axis shifts through about 90° anti-clockwise from the sinus direction of +90°. The P-wave duration increases slightly as the crista terminalis increases, highlighting the importance of the specialized conduction structures of the heart in rapidly conducting the excitation wave.

Derived Vector ECGs

The derived vector ECG plots are shown for the frontal plane in figure 5.6 and in the transverse plane in figure 5.7. Again, the sinus rhythm is included in both figures for reference. The colour of the vector loop represents the passage of time and is coloured from purple, at 0 ms, through blue, green, yellow and ending up red at 500 ms after initiation of the P-wave.

The vector loop in the frontal plane for sinus rhythm is shown in figure 5.6(s). The vector loop is inscribed in an anti-clockwise direction. The efferent, or outgoing, limb is at approximately +90°, before it loops up to its maximal extension at approximately +75°. The afferent, or incoming, limb is at approximately +70°. The T_P wave is visible as a small anti-clockwise loop, almost linear, aligned at approximately -100°. The initial deflection along almost the same line is an artefact of the stimulus protocol. The P-wave loop is open, although like the ECGs it is not entirely smooth.

The frontal plane vector loop for pacing from site A, figure 5.6(a), is inscribed in an anti-clockwise direction. The loop is generally open, although there is a noticeable direction change where the afferent limb briefly returns to the efferent limb. This corresponds to the notch visible in the inferior limb leads. The main

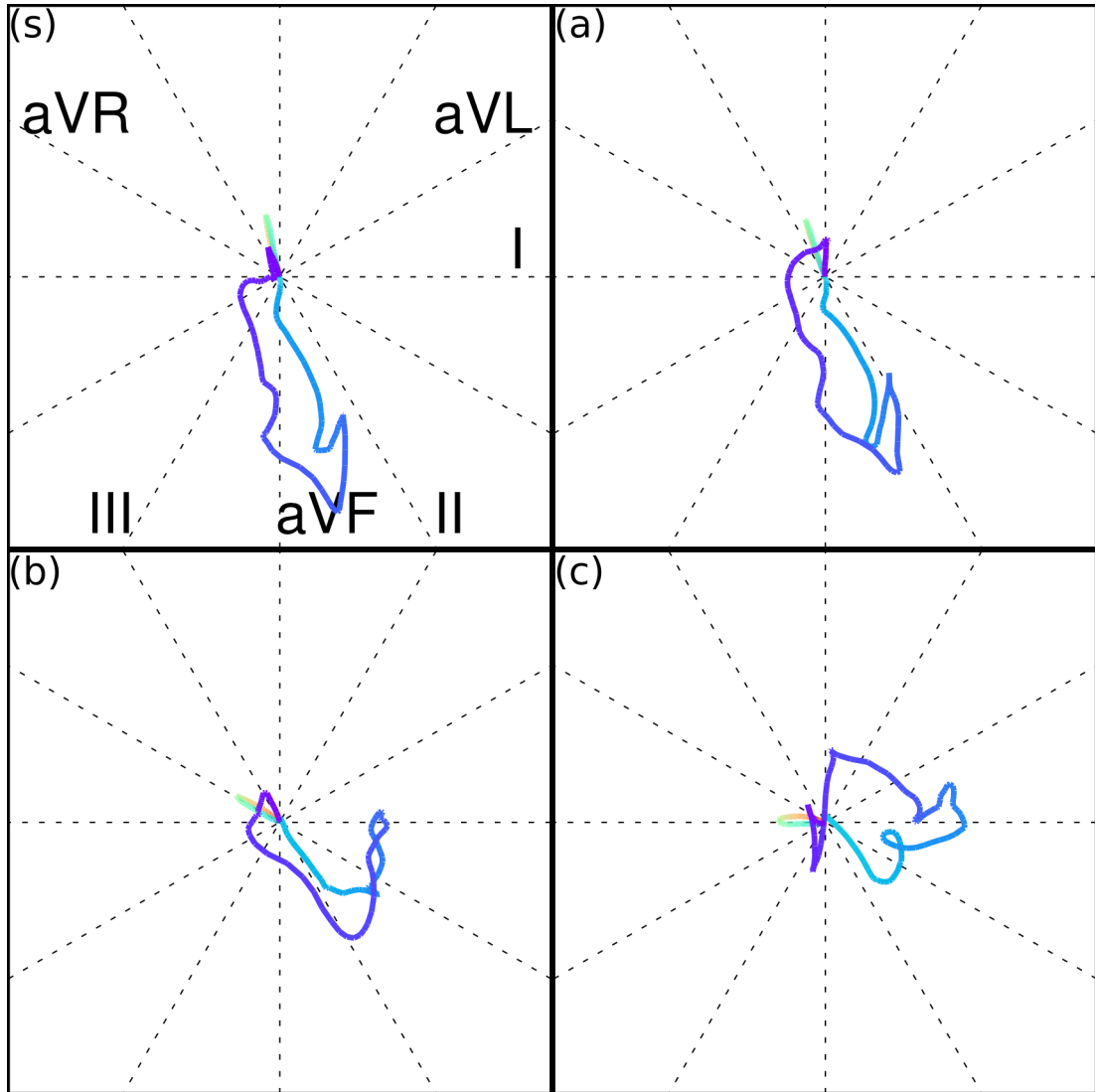


Figure 5.6: Frontal plane vector loops, constructed from the derived vECG for pacing at the sinus node, (s) and the three pacing sites A–C (a–c). Shown is one complete P-wave and T_P wave, pacing at a rate of 60 bpm. Colour represents the passage of time, going from purple (0 ms) through blue (250 ms) to red (500 ms) after the initiation of the stimulus. The horizontal and vertical scales are centred at 0 mV in the centre of the figure and extending out to ± 0.4 mV.

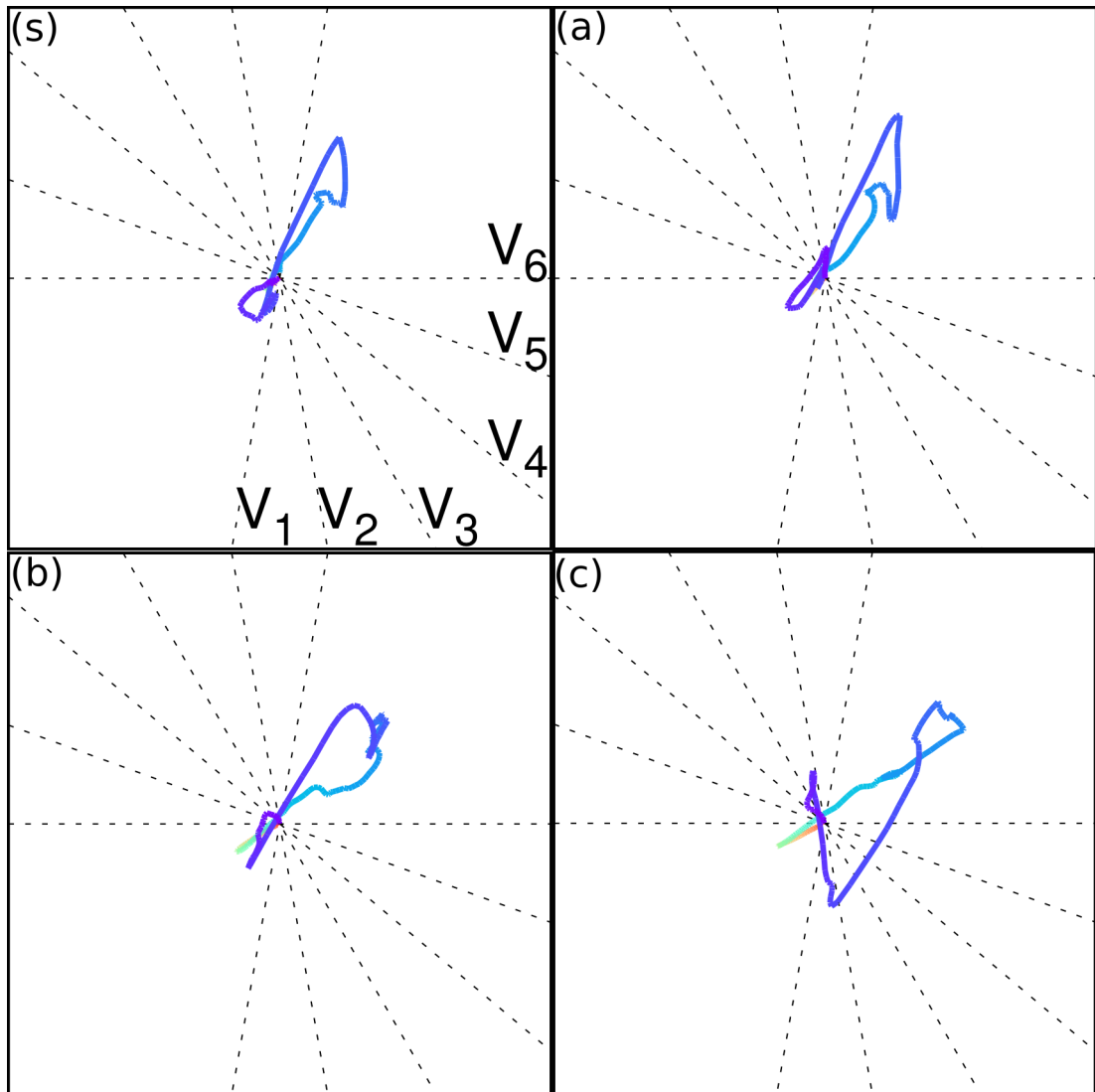


Figure 5.7: Transverse plane vector loops, constructed from the derived vECG for pacing at the sinus node, (s) and the three pacing sites A–C (a–c). Shown is one complete P-wave and T_P wave, pacing at a rate of 60 bpm. Colour represents the passage of time, going from purple (0 ms) through blue (250 ms) to red (500 ms) after the initiation of the stimulus. The horizontal and vertical scales are centred at 0 mV in the centre of the figure and extending out to ± 0.4 mV.

axis of the loop is at approximately $+70^\circ$. The efferent limb is aligned at approximately $+60^\circ$, along the line of lead II. The T_P wave is visible as a small loop, aligned at approximately -120° .

Pacing from site B produces the frontal plane vector loop in figure 5.6(b). The loop is largely inscribed in an anticlockwise direction. The main axis of the loop is aligned at approximately $+40^\circ$. The efferent limb is relatively smooth as it travels out along an approximately $+60^\circ$ vector. The loop then sweeps up to $+0^\circ$, crossing over itself several times, before it returns smoothly to 0. The T_P is a small clockwise loop at an angle of -120° . The loop from site C has the smallest area of the loops.

The frontal plane vector loop from pacing at site C is shown in figure 5.6(c). The loop is largely inscribed in as a very uneven figure-of-eight which is initially anticlockwise and is then clockwise. The main axis of the loop is aligned at approximately $+0^\circ$. The efferent limb is initially at $+90^\circ$ before it doubles back on itself to sweep up at an angle of -90° . It then sweeps down to $+0^\circ$, and the point of maximal extension. The afferent limb then sweeps back, inscribing a minor clockwise loops. The T_P is a small anticlockwise loop at an angle of -180° .

As the pacing site moves down the crista terminalis there are clear changes in the morphology and principle axis of the P-wave frontal vector loop. The axis shift which could be determined from the 12 lead ECG was clearly highlighted. The vector loops also show the reduction in amplitude of the P-wave as the pacing location is moved down the crista terminalis, possibly caused by the generally slower speed of activation. The T_P wave axis is opposite the main axis of the loop in all cases.

In contrast to the frontal plane vector plots, the transverse plane plots bear much less resemblance to the associated leads (V_{1-6}). The differences manifest in both the magnitude and the direction. This makes it hard to directly compare the transverse plane vector plots with the cardiac activity. The loops generated appear to be too flat and too negative in the Z (vertical) direction, which is especially obvious in the sinus rhythm plot (5.7(s)).

5.2.3 Discussion and Conclusions of Inverted P-wave Study

As the stimulus site moves down the crista terminalis the patterns of electrical activation in the atrium change noticeably. The focal point of excitation obviously moves down the crista terminalis to follow this. It is also interesting to note the

similarities. Despite the shifting activation site, the right atrial appendage and the region between the tricuspid valve and the atrial septum are always the last to activate in the right atrium. In the left atrium, the appendage also activates last in all cases.

As the pacing site moves away from the sinus node, the total activation time increases. However, total activation times remain within those observed clinically by Lemery et al. [131] for all three pacing locations away from the sinus node. The activation patterns are similar to those observed by Boineau et al. [133] as the pacing location moves, although the Boineau data does not include single activations away from the sinus node.

The latter two sites (B & C), which are low on the crista terminalis, appear to reach the left atrium in part through a site which emerges close to the coronary sinus [7, 131, 183, 184]. There is no specialist inferior intra-atrial conduction pathway in the model however. Conduction along this lower route is therefore at the normal bulk tissue rate. It is possible if this were treated specially in the model total activation times would be reduced.

The ECGs generated from the model also show an evolution as the stimulus site moves down the crista terminalis. This change is more visible in the limb leads than in the precordial leads. This is to be expected, as the propagation remained from right to left in all cases, but whether it is travelling up or down the atria changes as the pacing site does. The P-waves in leads II and aVF is positive in during sinus rhythm, and both gradually invert as the pacing site shifts down the crista terminalis, as hypothesised.

As the pacing site moves away from the sinus node, the P-wave duration also increases. Especially for the lower crista terminalis sites (B & C), the duration exceeds normal P-wave limits [131, 169]. It is possible that a more detailed intra-atrial conduction system, including an inferior pathway would reduce total conduction time, and therefore P-wave duration in these cases.

The P-wave vector loops are similar to those observed in clinical studies [182, 185–187], although the typical presentation of such loops as monochromatic does make comparison of the timing information and direction of inscription hard. They make it quite obvious that the cardiac axis shifts as the pacing location does. The morphology of the loops can be used to gain further clues, such as with the initial rise and then fall visible in the Site B frontal vector loops.

The limitations of the body surface potential model have been discussed previously (§4.6). Of particular importance to this study is the lack of a distributed sinus node model [180, 188] for the human atrium. However, pacemaker shift under the influence of acetylcholine [179] has been observed in rabbits and in humans [189] so it seems plausible as a mechanism for the shifts and associated P-wave inversions. The use of an inverse dower matrix to obtain the frank leads rather than directly measuring them was chosen to allow more direct comparison with clinical data, which is often only for the standard twelve leads. The selection of the correct transform matrix is important [182, 190, 191] and it is possible that the vector loop accuracy could be improved by the use of a transformation matrix optimised for the body surface potential model [192]. This is especially true for the Z-axis, which has the lowest correlation coefficient of the leads [191]. Alternatively a true frank lead system, or a hybrid model could be constructed.

The hypothesis that P-wave inversion could be caused by pacemaker shift in the human sinus node seems to be plausible. Progressive shift of the pacemaker site down the sinus node leads to progressive inversion of the observed P-waves in leads II and aVF. In addition, this shift is accompanied by other changes which do not stray too far from normality. This is important, as the shift was originally observed in those with no diagnosed cardiac disorders. Further investigation is merited, once an appropriate model of the distributed sino-atrial node complex can be integrated into the atrial model.

This study shows that the body surface potential model can be used for a study which involves conditions that begin to deviate from normality. It can therefore be used as a powerful tool for investigating the clinically observable consequences of changes to cardiac behaviour.

5.3 Discussion and Conclusion

The constructed model has been used in two separate studies. The first was a validation of an existing clinically derived algorithm for predicting the origin of focal point tachycardia. The second study concerned itself with investigation into a new clinical phenomena, that of inverted P-waves at night.

The focal tachycardia algorithm study confirms the performance of the algorithm. This validates both the algorithm and the model. The study also

highlights a potential weakness in the model, that of the high amplitudes it produces. Despite this problem, the model still performs well and was ‘well behaved’ according to the algorithm under test. In addition, there is no indication that a reduction in the amplitude due to a more complete consideration of the inhomogeneities would adversely impact this.

The inverted P-wave study confirms that a suggested mechanism for inverted P-waves at night, that of pacemaker shift under increased vagal tone, is plausible. The ECGs calculated by the model show a clear evolution as the pacing site shifts further down the crista terminalis. Additional validation is obviously required with a suitable model of a distributed pacemaker complex.

The model developed is therefore a useful tool for cardiac modelling. It can enhance the conclusions that can be drawn from 3D simulations with further clinical relevance.

Chapter 6

Discussion and Conclusions

This was an investigation into models of cardiac tissue, with a special focus on atrial tissue. It included whole atrial models, which were then extended beyond the heart to simulate the P-wave ECG. A toolkit providing access to efficient implementations of various experimental protocols was developed. A model of the atrium based on biophysically detailed myocyte models, including tissue heterogeneity and anisotropic conduction, was constructed. The atrial model was used as the basis of a model of the P-wave ECG which was solved using a boundary elemental formulation. All of the tools and models developed were used to perform physiological studies of tissues in healthy and diseased states.

6.1 Cardiac Simulation Toolkit

The cardiac toolkit which was developed provides easy access to a wide variety of experimental protocols. These protocols are used to assess the physiological impact of a gene mutation, drug action, hormonal effect or other electrophysiological modification. They include protocols which act on single cells and also on one dimensional idealisations of cardiac tissue.

The implementations of these protocols focused on efficient algorithms which take advantage of the computational nature of the models. It was important that this did not compromise the physiological accuracy and level of detail employed. This was accomplished in part through the use of lookup tables which reduced the computational effort needed to solve 1 ms of cardiac activity compared to an implementation lacking such tables without impacting measured physiological characteristics significantly. Such a saving might be considered a ‘cell level’

performance optimisation. Greater savings can be observed through the use of ‘protocol level’ performance optimisation. These protocol level optimisations are where the computational nature of the models can really be exploited. Optimisations include storing of cellular state after the pre-pacing part of the protocol and adaptive stepping when tracking response curves of varying slope. There was also the novel use of a basic computer science algorithm, the binary search, to determine the limits in a number of experimental protocols. This can be used, with a sensible choice of initial guesses, to reduce the total number of cases which must be tested by an order of magnitude.

The toolkit also offers an easy way of specifying and running 2D simulations. Simulation, even of irregular geometry, is simplified. Utilities can be used to convert quantified colour bitmaps into simulation geometries with heterogeneous electrophysiology. A variety of stimulation protocols can be specified, including both current and voltage stimuli. The simulations are accompanied by regular outputting of gif snapshots of the voltage, to allow simulations to be assessed as they run. In addition, the tissue simulation code is parallelized using a shared memory paradigm with OpenMP.

The toolkit was used to complete two computational studies. These examined the influence of a novel anion bearing current, I_{ANION} , in atrial myocyte cells and the effects of atrial fibrillation induced electrophysiological remodelling on the heterogeneity of atrial myocyte electrophysiological properties. The two studies represent different extremes. In the I_{ANION} study the influence on the action potential itself was very small, although even this had significant influence on the dynamic behaviours. In the remodelling study, the effects were obvious at all levels and this was reflected in the persistent spiral wave activity.

6.2 Whole Atrial Model

The whole atrium model which was developed is capable of modelling the electrophysiological behaviour of the atrium at the whole tissue level. It includes both conduction anisotropy and tissue heterogeneity. The use of biophysically detailed myocyte model as the basis makes the model flexible. Diffusion of voltage was altered to produce conduction velocities in the atrial tissue comparable with those measured experimentally and to reproduce clinical measurement of total activation time under sinus rhythm. The model is based on an anatomical

geometry, not an idealised one, including fluctuations in wall thickness and other anatomical deviations. All these features make the model suitable for modelling a variety of conditions. This includes those induced by fundamental changes to the electrophysiology caused by genetic defects or drug actions.

The level of detail might make the model computationally unattractive, as it involves solving many ordinary differential equations to advance the cellular state as well as calculating the diffusion between many cells. The model is parallelized, using a shared memory paradigm, allowing the effort to be split over several cores. The biophysically detailed model used as the basis uses precomputed lookup tables to calculate many of the parameters which influence the gating variables, reducing repetition of effort at minimal cost of overall accuracy. Repeated calculations are also reduced by pre-computation of the Laplacian operator used to diffuse the voltage. This is especially useful in the relatively thin walled atria, which therefore have many more boundary cells. All these refinements keep the total computational time within acceptable limits whilst maintaining the biophysical detail required for many studies.

Using the toolkit and a simplified version of the whole atrial model the effects of a novel gene mutation, the S140G mutation in the KCNQ1 gene, were assessed. This gene has been linked to the prevalence of atrial fibrillation in a Chinese family afflicted with it. The gene affects the I_{Ks} channel, adding an instantaneous component to the channel kinetics. This additional leakage component dramatically abbreviates the action potential duration. The restitution curves of the model were flattened and lowered by the influence of the mutation, reducing the rate response of the tissue. This allowed the tissue to sustain pacing at very high rates (>500 bpm) which were observed clinically. Simulations in a two-dimensional tissue model revealed that the spatial vulnerability window was reduced, suggesting that a much smaller region of ectopic activity would be needed to incite arrhythmic activity. The two dimensional models also suggested that the mutation allowed longer lived spiral waves to exist in the tissue which would form a stable mother rotor. Simulations using the atrium model suggested that whilst in normal tissue arrhythmic excitation would often decay away, in tissues afflicted with the S140G mutation sustained arrhythmic activity was observed. This activity was often a sustained mother rotor, but sometimes the anatomical features present in the atrial model could lead to breakup into complex, fibrillatory activity.

6.3 Body Surface Potential Model

A model of the P-wave body surface potential using the boundary element method was created. This used the atrial model as the basis for calculating the cardiac dipoles. The meshes representing the body and selected internal inhomogeneities were based on CT scans although they had been simplified considerably. The atrium was located within the mesh using the internal inhomogeneities as guides as well as anatomical descriptions of the location of the atria. From the computed body surface potential traces were extracted to represent the 12 lead ECG and body surface potential maps.

Again, computational tractability was an important concern. This motivated the choice to use the boundary element method. In addition, the dipole contributions of several nodes of the atrial model were aggregated together and assumed to act at the centroid of the aggregated region. This reduced the total number of dipole sources by three orders of magnitude, whilst having negligible impact on the final result. The meshes were refined for the final computations to produce high quality body surface potential maps. This had almost no influence on the computed ECGs suggesting that for ECG centric studies, such a refined mesh was not required. Even with the refined mesh the problem remained tractable, solving 1s of body surface potential calculations in an acceptable time using only one core. The implementation itself is quite flexible, allowing for easy incorporation of further meshes representing more internal detail.

Using the model the influence of internal inhomogeneities was examined. It was found that the lungs tended to amplify the magnitudes of signals seen in the leads, whilst the presence of blood masses tended to reduce them. The inhomogeneities had little influence on the phase of the signals observed in the 12 lead ECG, which showed good agreement with the clinical norms of the P-wave ECG. The amplitudes of the signal, in contrast, tended to be outside the normal physiological range. The reason for this was not entirely clear. It could be due to the lack of consideration of certain inhomogeneities, such as the skeletal bones or the skeletal muscle layer. It might also be possible that a better model of the bloodmasses would reduce this.

Despite the high amplitudes observed the model is still useful. The phase relationships are generally of more interest clinically as are the relative, rather than the absolute, amplitudes. Because of the biophysically detailed basis of the atrial model, the body surface potential model can be used in a variety of

physiological studies to provide insight into the clinically observable effects of the studied influence.

6.4 Applications of the Body Surface Potential Model

The body surface potential model was used to investigate two cases of clinical interest. It was used to assess an algorithm developed by physicians for locating the origin of focal point tachycardia. Also, a novel clinical phenomena, inverted P-waves at night, was investigated.

Focal atrial tachycardia is a supraventricular tachycardia characterised by excitation emerging from an ectopic focus site. It is readily treated by radio ablation therapy which is aided by accurate knowledge of the focal site. The algorithm presented used a decision tree approach, based on the waveform of several 12 lead ECG leads. To assess the algorithm, the model was paced from several ectopic sites around the atria. The ECG was used to make a decision based on the algorithm and this was compared to the actual origin. The origins predicted by the algorithm were in good agreement to the real pacing locations in 6 out of 8 cases and showed only minor difference (left versus right pulmonary veins) in one further case. The final case, which is quite inaccurate, would probably be resolved were the amplitudes closer to the clinically observed ranges—or if the algorithm's threshold were adjusted to account for the higher potentials. The good agreement provides validation of both the focal point origin algorithm and the model itself.

Inverted P-waves at night are a phenomena which has not been reported on in the literature. They have been observed in the inferior limb leads in certain cases in patients undergoing 24 hour cardiac monitoring. It was hypothesised that this could be due to pacemaker shift in a distributed pacemaker complex, induced by hormonal changes at night. To investigate this hypothesis, the body surface potential model was paced from several sites along the crista terminalis, to represent progressively greater degree of shift and then the twelve lead ECG was computed. It was observed that as the pacing site moved further along the crista terminalis, the P-wave ECG in the inferior leads flattened and then inverted, in accordance with the hypothesis. Pacemaker shift is therefore a viable mechanism for the observed P-wave changes at night.

6.5 Future Work

The work presented here opens up many paths for future efforts. The models and tools developed in the study can be refined. They can also be used, with and without such refinement, for new studies.

The toolkit developed can be extended in a number of ways. The library of cellular models available can be increased, either through direct addition, or by the development of a converter which can take CellML models and produce code suitable for use. More experimental protocols could be added to the toolkit, expanding its utility. The use of more sophisticated integrators for cellular equations could be incorporated into the models and their influence on the performance and results assessed. The toolkit could also be expanded into three dimensions, allowing the same ease of specifying numerical experiments to be enjoyed in whole heart simulations. As an alternative to this, implementing the protocols on top of one of the other toolkits might offer a better alternative.

The atrial model can also be refined in a number of ways. As new models of atrial tissue are developed, they can be incorporated into the model so that it always represents the best knowledge we have of the atrium and its complexities. A more complete map of the regions and directions of preferential conduction could be incorporated into the model which could be important for non-sinus rhythm cases. For some studies an accurate and auto-active pacemaker complex would be a benefit. Contraction, and the associated mechanical and electric coupling, could be incorporated into the model.

It might also be interesting to construct a limit variable formulation of the model, either with Fenton–Karma variants or through variable reduction of the CRN or other biophysically detailed models. This would enable rapid initial investigation of interesting phenomena. The full model would then be used to verify the initial findings and confirm they still existed.

Beyond the atrium, the body surface model has several avenues for further study. The influence of further inhomogeneities can be investigated. Patient specific studies, where the cardiac geometry and torso structure are based on CT and MRI scans of the patient offer exciting possibilities. First, direct comparison with clinical data allows for further validation of the underlying model. Such models can also be used to suggest and test appropriate clinical procedures.

Patient specific models also allow for the possibility of developing a family of models, representing different orientations and conformations of the atrium and

the surrounding torso. Using such a family of models would allow the results of computational studies to be stated with more confidence. An effect observed in one model might be an artefact of the geometry, but an affect observed in five or ten or more is much less likely to be so.

Without any refinement, the toolkit and models developed offer a good basis for many electrophysiological studies on a variety of scales. The biophysical detail employed makes them suitable for the investigation of complex effects. The computational efficiency makes relatively long term simulations a possibility too.

Bibliography

- [1] Allender S, Peto V, Scarborough P, Kaur A, Rayner M. Coronary heart disease statistics. BHF: London, 2008.
- [2] Oberman A, Myers AR, Karunas TM, Epstein FH. Heart size of adults in a natural population—tecumseh, michigan. variation by sex, age, height, and weight. *Circulation* Apr 1967;35(4):724–733.
- [3] Katz AM. Physiology of the Heart. 4th edition. Lippincott Williams and Wilkins, 2006.
- [4] Ho SY, Anderson RH, Snchez-Quintana D. Atrial structure and fibres: morphologic bases of atrial conduction. *Cardiovasc Res* May 2002;54(2):325–336.
- [5] Ho SY, Anderson RH, Snchez-Quintana D. Gross structure of the atriums: more than an anatomic curiosity? *Pacing Clin Electrophysiol* Mar 2002; 25(3):342–350.
- [6] Ho SY, Snchez-Quintana D. The importance of atrial structure and fibers. *Clin Anat* Jan 2009;22(1):52–63. URL <http://dx.doi.org/10.1002/ca.20634>.
- [7] Platonov PG. Interatrial conduction in the mechanisms of atrial fibrillation: from anatomy to cardiac signals and new treatment modalities. *Europace* Nov 2007;9 Suppl 6:vi10–vi16. URL <http://dx.doi.org/10.1093/europace/eum201>.
- [8] Platonov PG, Mitrofanova L, Ivanov V, Ho SY. Substrates for intra-atrial and interatrial conduction in the atrial septum: anatomical study on 84 human hearts. *Heart Rhythm* Aug 2008;5(8):1189–1195. URL <http://dx.doi.org/10.1016/j.hrthm.2008.04.025>.

- [9] Feng J, Yue L, Wang Z, Nattel S. Ionic mechanisms of regional action potential heterogeneity in the canine right atrium. *Circ Res* Sep 1998; 83(5):541–551.
- [10] Jones SA, Yamamoto M, Tellez JO, Billeter R, Boyett MR, Honjo H, Lancaster MK. Distinguishing properties of cells from the myocardial sleeves of the pulmonary veins a comparison of normal and abnormal pacemakers. *CIRCULATION ARRHYTHMIA AND ELECTROPHYSIOLOGY* April 2008;1(1):39–48. ISSN 1941-3149.
- [11] Hille B. Ion Channels Of Excitable Membranes. 3 edition. Sinauer Associates, Inc., 2001.
- [12] Noble D. A modification of the Hodgkin-Huxley equations applicable to Purkinje fibres action and pacemaker potential. *J Physiol Lond* 1962; 160:317–352.
- [13] Beeler G, Reuter H. Reconstruction of the action potential of ventricular myocardial fibres. *J Physiol Lond* 1977;268:177–210.
- [14] Luo CH, Rudy Y. A model of the ventricular cardiac action potential. depolarization, repolarization, and their interaction. *Circ Res* Jun 1991; 68(6):1501–1526.
- [15] Luo C, Rudy Y. A dynamic model of the cardiac ventricular action potential. *Circulation Research* 1994;74:1071–1096.
- [16] Courtemanche M, Ramirez RJ, Nattel S. Ionic mechanisms underlying human atrial action potential properties: insights from a mathematical model. *Am J Physiol* 1998;275(1 Pt 2):H301–21.
- [17] Nygren A, Fiset C, Firek L, Clark JW, Lindblad DS, Clark RB, Giles WR. Mathematical model of an adult human atrial cell: the role of K^+ currents in repolarization. *Circ Res* 1998;82(1):63–81.
- [18] Fenton F, Karma A. Erratum: "vortex dynamics in three-dimensional continuous myocardium with fiber rotation: Filament instability and fibrillation" [chaos 8, 20-47 (1998)]. *Chaos* Dec 1998;8(4):879. URL <http://dx.doi.org/10.1063/1.166374>.

- [19] Fall CP, Keizer JE. Computational Cell Biology. Springer Science and Business, LLC, 2002; 21–50.
- [20] Hodgkin A, Huxley A. A quantitative description of membrane current and its application to conduction and excitation in nerve. *Journal Of Physiology Lond* 1952;117:500–544.
- [21] Keener J, Sneyd J. Mathematical Physiology, volume 8 of Interdisciplinary Applied Mathematics. Springer, New York., 1998.
- [22] Balser JR, Roden DM, Bennett PB. Global parameter optimization for cardiac potassium channel gating models. *Biophys J Mar* 1990;57(3):433–444. URL [http://dx.doi.org/10.1016/S0006-3495\(90\)82560-1](http://dx.doi.org/10.1016/S0006-3495(90)82560-1).
- [23] Clancy CE, Rudy Y. Linking a genetic defect to its cellular phenotype in a cardiac arrhythmia. *Nature Aug* 1999;400(6744):566–569. URL <http://dx.doi.org/10.1038/23034>.
- [24] Silva J, Rudy Y. Subunit interaction determines iks participation in cardiac repolarization and repolarization reserve. *Circulation Sep* 2005; 112(10):1384–1391. URL <http://dx.doi.org/10.1161/CIRCULATIONAHA.105.543306>.
- [25] Lindblad DS, Murphey CR, Clark JW, Giles WR. A model of the action potential and underlying membrane currents in a rabbit atrial cell. *Am J Physiol Oct* 1996;271(4 Pt 2):H1666–H1696.
- [26] NYGREN A, LEON LJ, GILES WR. Simulations of the human atrial action potential. *Philosophical Transactions of the Royal Society of London Series A Mathematical Physical and Engineering Sciences* 2001;359(1783):1111–1125. URL <http://rsta.royalsocietypublishing.org/content/359/1783/1111.abstract>.
- [27] Syed Z, Vigmond E, Nattel S, Leon LJ. Atrial cell action potential parameter fitting using genetic algorithms. *Med Biol Eng Comput Sep* 2005; 43(5):561–571.
- [28] Cherry EM, Hastings HM, Evans SJ. Dynamics of human atrial cell models: restitution, memory, and intracellular calcium dynamics in single cells. *Prog*

- Biophys Mol Biol Sep 2008;98(1):24–37. URL <http://dx.doi.org/10.1016/j.pbiomolbio.2008.05.002>.
- [29] Bueno-Orovio A, Cherry EM, Fenton FH. Minimal model for human ventricular action potentials in tissue. J Theor Biol Aug 2008;253(3):544–560. URL <http://dx.doi.org/10.1016/j.jtbi.2008.03.029>.
 - [30] Weber F, Lurz S, Keller D, Weiss D, Seemann G, Lorenz C, Dossel O. Adaptation of a minimal four-state cell model for reproducing atrial excitation properties. In Computers in Cardiology, 2008. ISSN 0276-6547, Sept. 2008; 61–64.
 - [31] Tung L. A Bidomain Model for Describing Ischemic Myocardial dc Potentials. Ph.D. thesis, Massachusetts Institute of Technology, 1978.
 - [32] Geselowitz DB, Miller WT. A bidomain model for anisotropic cardiac muscle. Ann Biomed Eng 1983;11(3-4):191–206.
 - [33] Sundnes J, Lines GT, Cai X, Nielsen BF, Mardal KA, Tveito A. Computing the Electrical Activity in the Heart. Monographs in Computational Science and Engineering. Springer, 2006.
 - [34] Birkhoff G, Rota GC. Ordinary Differential Equations. 4th edition. John Wiley and Sons, 1989; 1–33.
 - [35] Morton KW, Mayers DF. Numerical solution of partial differential equations : an introduction. Cambridge University Press, 2005.
 - [36] Rush S, Larsen H. A practical algorithm for solving dynamic membrane equations. IEEE Trans Biomed Eng 1978;25(4):389–92.
 - [37] Kligfield P. The centennial of the einthoven electrocardiogram. J Electrocardiol 2002;35 Suppl:123–129. URL <http://dx.doi.org/10.1054/jelc.2002.37169>.
 - [38] Levick J. An Introduction to Cardiovascular Physiology. Butterworth-Heinemann Ltd, 1991.
 - [39] Jahrsdoerfer M, Giuliano K, Stephens D. Clinical usefulness of the easi 12-lead continuous electrocardiographic monitoring system. Crit Care Nurse Oct 2005;25(5):28–30, 32–7; quiz 38.

- [40] Sobieszczanska M, Jagielski J, Nowak B, Pilecki W, Kalka D. Appraisal of bspm obtained from the limited lead system. *Anadolu Kardiyol Derg* Jul 2007;7 Suppl 1:11–13.
- [41] Grube E, Bootsvelt A, Yuecel S, Shen JT, Imhoff M. Computerized two-lead resting ecg analysis for the detection of coronary artery stenosis. *Int J Med Sci* 2007;4(5):249–263.
- [42] Finlay DD, Nugent CD, Kellett JG, Donnelly MP, McCullagh PJ, Black ND. Synthesising the 12-lead electrocardiogram: Trends and challenges. *Eur J Intern Med* Dec 2007;18(8):566–570. URL <http://dx.doi.org/10.1016/j.ejim.2007.04.011>.
- [43] McFee R, Johnston FD. Electrocardiographic leads. i. introduction. *Circulation* Oct 1953;8(4):554–568.
- [44] McFee R, Johnston FD. Electrocardiographic leads. ii. analysis. *Circulation* Feb 1954;9(2):255–266.
- [45] McFee R, Johnston FD. Electrocardiographic leads. iii. synthesis. *Circulation* Jun 1954;9(6):868–880.
- [46] Burger HC, Milaan JBV. Heart-vector and leads. *Br Heart J* Jul 1946; 8(3):157–161.
- [47] Geddes LA, Baker LE. The specific resistance of biological material—a compendium of data for the biomedical engineer and physiologist. *Med Biol Eng* May 1967;5(3):271–293.
- [48] de Jong J. Basics. <http://en.ecgpedia.org/wiki/Basics>, 2008. Accessed 17/09/09. Images are released under a Creative Commons Attribution-Noncommercial-Share Alike 3.0.
- [49] Wilson F, Johnston F, MacLeod A. Electrocardiograms that represent the potential variations of a single electrode. *Am Heart J* 1934;9:447–471.
- [50] Goldberger E. A simple indifferent electrocardiographic electrode of zero potential and a technique of obtaining augmented, unipolar extremity leads. *Am Heart J* 1942;23:483–92.

- [51] Wilson F, Johnston F, Rosenbaum F, Erlanger H, Kossmann C, Hecht H, Cotrim N, Menezes de Oliveira R, Scarsi R, Barker P. The precordial electrocardiogram. *Am Heart J* 1944;27:19–85.
- [52] Hampton JR. *The ECG Made Easy*. Churchill Livingstone, 2008.
- [53] Lipman BC, Cascio T. *ECG Assessment And Interpretation*. F. A. Davis Company, 1994.
- [54] Hurst JW. Naming of the waves in the ecg, with a brief account of their genesis. *Circulation* Nov 1998;98(18):1937–1942.
- [55] Frank E. An accurate, clinically practical system for spatial vectorcardiography. *Circulation* May 1956;13(5):737–749.
- [56] Dower G, Machado H, Osborne J. On deriving the electrocardiogram from vectorradiographic leads. *Clin Cardiol* Apr 1980;3(2):87–95.
- [57] Edenbrandt L, Pahlm O. Vectorcardiogram synthesized from a 12-lead ecg: superiority of the inverse dower matrix. *J Electrocardiol* Nov 1988; 21(4):361–367.
- [58] Uijen GJH, van Oosterom A, van Dam RT. The relationship between the 12-lead standard ECG and the XYZ vector leads. In Schubert E (ed.), *Proceedings of the 14th International Congress on Electrocardiology*. 1988; 301–307.
- [59] Dubuc M, Nadeau R, Tremblay G, Kus T, Molin F, Savard P. Pace mapping using body surface potential maps to guide catheter ablation of accessory pathways in patients with wolff-parkinson-white syndrome. *Circulation* Jan 1993;87(1):135–143.
- [60] SippensGroenewegen A, Roithinger FX, Peeters HA, Linnenbank AC, van Hemel NM, Steiner PR, Lesh MD. Body surface mapping of atrial arrhythmias: atlas of paced p wave integral maps to localize the focal origin of right atrial tachycardia. *J Electrocardiol* 1998;31 Suppl:85–91.
- [61] Ramanathan C, Jia P, Ghanem R, Ryu K, Rudy Y. Activation and repolarization of the normal human heart under complete physiological conditions. *Proc Natl Acad Sci U S A* Apr 2006;103(16):6309–6314. URL <http://dx.doi.org/10.1073/pnas.0601533103>.

- [62] Ihara Z, van Oosterom A, Jacquemet V, Hoekema R. Adaptation of the standard 12-lead electrocardiogram system dedicated to the analysis of atrial fibrillation. *J Electrocardiol* Jan 2007;40(1):68.e1–68.e8. URL <http://dx.doi.org/10.1016/j.jelectrocard.2006.04.006>.
- [63] Brody DA. A theoretical analysis of intracavitary blood mass influence on the heart-lead relationship. *Circ Res* Nov 1956;4(6):731–738.
- [64] Barr RC, Pilkington TC, Boineau JP, Spach MS. Determining surface potentials from current dipoles, with application to electrocardiography. *IEEE Trans Biomed Eng* Apr 1966;13(2):88–92.
- [65] Barnard AC, Duck IM, Lynn MS, Timlake WP. The application of electromagnetic theory to electrocardiology. ii. numerical solution of the integral equations. *Biophys J* Sep 1967;7(5):463–491. URL [http://dx.doi.org/10.1016/S0006-3495\(67\)86599-8](http://dx.doi.org/10.1016/S0006-3495(67)86599-8).
- [66] Rush S. An inhomogeneous anisotropic model of the human torso for electrocardiographic studies. *Med Biol Eng* May 1971;9(3):201–211.
- [67] Gulrajani RM, Mailloux GE. A simulation study of the effects of torso inhomogeneities on electrocardiographic potentials, using realistic heart and torso models. *Circ Res* Jan 1983;52(1):45–56.
- [68] Horacek BM, Purcell C, Lamothe R, Merritt R, Kafer C, Periyalwar S, Dey S, Leon LJ, Stroink G. The effect of torso geometry on magnetocardiographic isofield maps. *Phys Med Biol* Jan 1987;32(1):121–124.
- [69] Aoki M, Okamoto Y, Musha T, Harumi K. Three-dimensional simulation of the ventricular depolarization and repolarization processes and body surface potentials: normal heart and bundle branch block. *IEEE Trans Biomed Eng* Jun 1987;34(6):454–462.
- [70] Weixue L, Xu Z, Fu Y. Microcomputer-based cardiac field simulation model. *Med Biol Eng Comput* Jul 1993;31(4):384–387.
- [71] Weixue L, Ling X. Computer simulation of epicardial potentials using a heart-torso model with realistic geometry. *IEEE Trans Biomed Eng* Feb 1996;43(2):211–217. URL <http://dx.doi.org/10.1109/10.481990>.

- [72] van Dam PM, van Oosterom A. Volume conductor effects involved in the genesis of the P wave. *Europace* 2005;7(s2):S30–38. URL <http://europace.oxfordjournals.org/cgi/content/abstract/7/s2/S30>.
- [73] Seger M, Fischer G, Modre R, Hanser F, Pfeifer B, Hintermuller C, Roithinger FX, Hintringer F, Trieb T, Schocke M, Tilg B. Simulation of atrial electrophysiology and body surface potentials for normal and abnormal rhythm. In Proc. 26th Annual International Conference of the IEEE Engineering in Medicine and Biology Society IEMBS '04, volume 1. September 1–5, 2004; 817–820.
- [74] Klepfer RN, Johnson CR, Macleod RS. The effects of inhomogeneities and anisotropies on electrocardiographic fields: a 3-d finite-element study. *IEEE Trans Biomed Eng* Aug 1997;44(8):706–719. URL <http://dx.doi.org/10.1109/10.605427>.
- [75] Keller DUJ, Seemann G, Weiss DL, Farina D, Zehlein J, Dssel O. Computer based modeling of the congenital long-qt 2 syndrome in the visible man torso: from genes to ecg. *Conf Proc IEEE Eng Med Biol Soc* 2007;2007:1410–1413. URL <http://dx.doi.org/10.1109/IEMBS.2007.4352563>.
- [76] Li ZS, Zhu SA, He B. Solving the ecg forward problem by means of a meshless finite element method. *Phys Med Biol* Jul 2007;52(13):N287–N296. URL <http://dx.doi.org/10.1088/0031-9155/52/13/N02>.
- [77] Clayton RH, Holden AV. Computational framework for simulating the mechanisms and ecg of re-entrant ventricular fibrillation. *Physiol Meas* Nov 2002;23(4):707–726.
- [78] Gulranjani RM, Roberge FA, Mailloux GE. The Forward Problem Of Electrocardiography. Pergamon Press, Oxford, 1989; 197–236.
- [79] Lloyd C, Lawson J, Hunter P, Nielsen P. The cellml model repository. *Bioinformatics* September 2008;24(18):2122–2123.
- [80] Cooper J, McKeever S, Garny A. On the application of partial evaluation to the optimisation of cardiac electrophysiological simulations. In PEPM '06: Proceedings of the 2006 ACM SIGPLAN symposium on Partial evaluation

- and semantics-based program manipulation. New York, NY, USA: ACM. ISBN 1-59593-196-1, 2006; 12–20.
- [81] Vigmond EJ, Hughes M, Plank G, Leon LJ. Computational tools for modeling electrical activity in cardiac tissue. *J Electrocardiol* 2003;36 Suppl:69–74.
 - [82] Bauer S, Rder G, Br M. Alternans and the influence of ionic channel modifications: Cardiac three-dimensional simulations and one-dimensional numerical bifurcation analysis. *Chaos* Mar 2007;17(1):015104.
 - [83] Plank G, Liebmann M, Weber dos Santos R, Vigmond E, Haase G. Algebraic multigrid preconditioner for the cardiac bidomain model. *IEEE Trans Biomed Eng* 2007;54(4):585–596.
 - [84] Vigmond E, Clements C. Construction of a computer model to investigate sawtooth effects in the purkinje system. *IEEE Trans Biomed Eng* 2007; 54(3):389–99.
 - [85] An interactive computer program for continuum mechanics, image analysis, signal processing and system identification. URL <http://www.bioeng.auckland.ac.nz/cmiss/cmiss.php>.
 - [86] Garny A, Kohl P, Noble D. Cellular open resource (cor): a public cellml based environment for modelling biological function. *Int J Bif Chaos* 2003; 13:3579–3590.
 - [87] Flanagan D, Matsumoto Y. The Ruby Programming Language. O'Reilly Media, Inc., 2008.
 - [88] Chapman B, Jost G, van der Pas R. Using OpenMP: Portable Shared Memory Parallel Programming. The MIT Press, 2007.
 - [89] Message Passing Interface Forum. MPI: A message passing interface standard 1.1. <http://www.mpi-forum.org/docs/mpi-10.ps>, 1994.
 - [90] GCC Compiler Team. GCC, the GNU compiler collection. <http://gcc.gnu.org/>, 1987–2009.
 - [91] ICC Compiler Team. ICC, intel(r) C/++ compiler. <http://developer.intel.com/software/products/compilers/>, 2002–2006.

- [92] Victorri B, Vinet A, Roberge FA, Drouhard JP. Numerical integration in the reconstruction of cardiac action potentials using hodgkin-huxley-type models. *Comput Biomed Res* Feb 1985;18(1):10–23.
- [93] Cormen TH. Introduction to algorithms. Cambridge, MA, USA: MIT Press, 2001. ISBN 0-262-03293-7.
- [94] Kim BS, Kim YH, Hwang GS, Pak HN, Lee SC, Shim WJ, Oh DJ, Ro YM. Action potential duration restitution kinetics in human atrial fibrillation. *J Am Coll Cardiol* Apr 2002;39(8):1329–1336.
- [95] Xie F, Qu Z, Garfinkel A, Weiss JN. Electrical refractory period restitution and spiral wave reentry in simulated cardiac tissue. *Am J Physiol Heart Circ Physiol* 2002;283(1):H448–60.
- [96] Qu Z, Weiss JN, Garfinkel A. Cardiac electrical restitution properties and stability of reentrant spiral waves: a simulation study. *Am J Physiol Jan* 1999;276(1 Pt 2):H269–H283.
- [97] Cherry EM, Fenton FH. Suppression of alternans and conduction blocks despite steep apd restitution: electrotonic, memory, and conduction velocity restitution effects. *Am J Physiol Heart Circ Physiol Jun* 2004;286(6):H2332–H2341. URL <http://dx.doi.org/10.1152/ajpheart.00747.2003>.
- [98] Cherry EM, Fenton FH. A tale of two dogs: analyzing two models of canine ventricular electrophysiology. *Am J Physiol Heart Circ Physiol Jan* 2007;292(1):H43–H55. URL <http://dx.doi.org/10.1152/ajpheart.00955.2006>.
- [99] Decker KF, Heijman J, Silva JR, Hund TJ, Rudy Y. Properties and ionic mechanisms of action potential adaptation, restitution, and accommodation in canine epicardium. *Am J Physiol Heart Circ Physiol Apr* 2009;296(4):H1017–H1026. URL <http://dx.doi.org/10.1152/ajpheart.01216.2008>.
- [100] Boyett MR, Jewell BR. A study of the factors responsible for rate-dependent shortening of the action potential in mammalian ventricular muscle. *J Physiol Dec* 1978;285:359–380.

- [101] Taggart P, Sutton PM, Boyett MR, Lab M, Swanton H. Human ventricular action potential duration during short and long cycles. rapid modulation by ischemia. *Circulation* Nov 1996;94(10):2526–2534.
- [102] Workman AJ, Kane KA, Rankin AC. The contribution of ionic currents to changes in refractoriness of human atrial myocytes associated with chronic atrial fibrillation. *Cardiovasc Res* 2001;52(2):226–35.
- [103] Kharche S, Garratt CJ, Boyett MR, Inada S, Holden AV, Hancox JC, Zhang H. Atrial proarrhythmia due to increased inward rectifier current ($i_{(k1)}$) arising from *kcnj2* mutation—a simulation study. *Prog Biophys Mol Biol* 2008;98(2-3):186–197. URL <http://dx.doi.org/10.1016/j.pbiomolbio.2008.10.010>.
- [104] Quan W, Rudy Y. Unidirectional block and reentry of cardiac excitation: a model study. *Circ Res* Feb 1990;66(2):367–382.
- [105] Zhang H, Garratt CJ, Holden AV. Onset and termination of reentrant excitation in homogeneous human virtual atrial tissue. I J Bifurcation and Chaos 2003;13(12):3631–3643.
- [106] Gonzlez H, Nagai Y, Bub G, Glass L, Shrier A. Reentrant waves in a ring of embryonic chick ventricular cells imaged with a Ca^{2+} sensitive dye. *Biosystems* Sep 2003;71(1-2):71–80.
- [107] Qu Z, Garfinkel A, Weiss JN. Vulnerable window for conduction block in a one-dimensional cable of cardiac cells, 1: single extrasystoles. *Biophys J* Aug 2006;91(3):793–804. URL <http://dx.doi.org/10.1529/biophysj.106.080945>.
- [108] Kumagai K, Khrestian C, Waldo AL. Simultaneous multisite mapping studies during induced atrial fibrillation in the sterile pericarditis model. Insights into the mechanism of its maintenance. *Circulation* 1997;95(2):511–21.
- [109] Qu Z, Xie F, Garfinkel A, Weiss JN. Origins of spiral wave meander and breakup in a two-dimensional cardiac tissue model. *Ann Biomed Eng* Jul 2000;28(7):755–771.

- [110] Clayton RH, Taggart P. Regional differences in apd restitution can initiate wavebreak and re-entry in cardiac tissue: a computational study. *Biomed Eng Online* 2005;4:54. URL <http://dx.doi.org/10.1186/1475-925X-4-54>.
- [111] Zou R, Kneller J, Leon LJ, Nattel S. Substrate size as a determinant of fibrillatory activity maintenance in a mathematical model of canine atrium. *Am J Physiol Heart Circ Physiol* Sep 2005;289(3):H1002–H1012. URL <http://dx.doi.org/10.1152/ajpheart.00252.2005>.
- [112] Li H, Zhang H, Hancox JC, Kozlowski RZ. An outwardly rectifying anionic background current in atrial myocytes from the human heart. *Biochem Biophys Res Commun* Aug 2007;359(3):765–770. URL <http://dx.doi.org/10.1016/j.bbrc.2007.05.177>.
- [113] Biktaševa IV, Biktašev VN, Holden AV. Wavebreaks and self-termination of spiral waves in a model of human atrial tissue. In Frangi AF, Radeva P, Santos A, Hernandez M (eds.), FIMH 2005, volume 3504 of Lecture Notes in Computer Science. Springer, 2005; 293–303.
- [114] Cherry EM, Evans SJ. Properties of two human atrial cell models in tissue: restitution, memory, propagation, and reentry. *J Theor Biol* Oct 2008;254(3):674–690. URL <http://dx.doi.org/10.1016/j.jtbi.2008.06.030>.
- [115] Nygren A, Giles WR. Mathematical simulation of slowing of cardiac conduction velocity by elevated extracellular. *Ann Biomed Eng* Aug 2000; 28(8):951–957.
- [116] Biktašev VN, Holden AV. Design principles of a low voltage cardiac defibrillator based on the effect of feedback resonant drift. *J Theor Biol* Jul 1994; 169(2):101–112. URL <http://dx.doi.org/10.1006/jtbi.1994.1132>.
- [117] Bernus O, Zemlin C, Zaritsky R, Minarov S, Pertsov A. Alternating conduction in the ischaemic border zone as a precursor of re-entrant arrhythmias: A simulation study. *Europace* 2005;7:S93–S104.
- [118] Coronel R, Wilms-Schopman F, Ophof T, Fiolet J, Janse M. Reperfusion arrhythmias in isolated perfused pig hearts. inhomogeneities in extracellular

- potassium, st and tq potentials, and transmembrane action potentials. *Circ Res* 1992;71(5):1131–1142.
- [119] Bosch RF, Zeng X, Grammer JB, Popovic K, Mewis C, Kuhlkamp V. Ionic mechanisms of electrical remodeling in human atrial fibrillation. *Cardiovasc Res* 1999;44(1):121–31.
- [120] Seemann G, Höper C, Sachse FB, Dössel O, Holden AV, Zhang H. Heterogeneous three-dimensional anatomical and electrophysiological model of human atria. *Philos Transact A Math Phys Eng Sci* 2006;364(1843):1465–81.
- [121] Kharche S, Seemann G, Leng J, Holden AV, Garratt CJ, Zhang H. Scroll waves in 3d virtual human atria: A computational study. In Sachse FB, Seemann G (eds.), FIMH 2007, volume 4466 of Lecture Notes in Computer Science. Springer, 2007; 129–138.
- [122] Kim BS, Kim YH, Hwang GS, Pak HN, Lee SC, Shim WJ, Oh DJ, Ro YM. Action potential duration restitution kinetics in human atrial fibrillation. *J Am Coll Cardiol* 2002;39(8):1329–1336. URL <http://content.onlinejacc.org/cgi/content/abstract/39/8/1329>.
- [123] Karma A. Electrical alternans and spiral wave breakup in cardiac tissue. *Chaos* Sep 1994;4(3):461–472. URL <http://dx.doi.org/10.1063/1.166024>.
- [124] ten Tusscher KHWJ, Panfilov AV. Alternans and spiral breakup in a human ventricular tissue model. *Am J Physiol Heart Circ Physiol* Sep 2006;291(3):H1088–H1100. URL <http://dx.doi.org/10.1152/ajpheart.00109.2006>.
- [125] Xie F, Qu Z, Garfinkel A, Weiss JN. Electrophysiological heterogeneity and stability of reentry in simulated cardiac tissue. *Am J Physiol Heart Circ Physiol* Feb 2001;280(2):H535–H545.
- [126] Seemann G, Höper C, Sachse FB, Zhang H, Dössel O. A detailed model of human atrium towards simulation of electromechanics in the heart. In MEDICON. 2004; .

- [127] Stott J, Kharche S, Law P, Zhang H. Simulating the effects of atrial fibrillation in electrically heterogeneous human atria: A computer modelling study. In Computers in Cardiology, 2008. ISSN 0276-6547, Sept. 2008; 65–68.
- [128] Panfilov A, Keener J. Re-entry in an anatomical model of the heart. Chaos Solitons Fractals 1995;5(3-4):681 – 689. ISSN 0960-0779. URL <http://www.sciencedirect.com/science/article/B6TJ4-3YXBRH2-5M/2/97e5b628fa57c8e59f59757d1b833df0>. Nonlinear Phenomena in Excitable Physiological Systems.
- [129] Fenton FH, Cherry EM, Karma A, Rappel WJ. Modeling wave propagation in realistic heart geometries using the phase-field method. Chaos Mar 2005; 15(1):13502. URL <http://dx.doi.org/10.1063/1.1840311>.
- [130] Misner CW, Thorne KS, Wheeler JA. Gravitation. San Francisco, CA: W. H. Freeman, 1973.
- [131] Lemery R, Soucie L, Martin B, Tang ASL, Green M, Healey J. Human study of biatrial electrical coupling: determinants of endocardial septal activation and conduction over interatrial connections. Circulation Oct 2004;110(15):2083–2089. URL <http://dx.doi.org/10.1161/01.CIR.0000144461.83835.A1>.
- [132] Hansson A, Holm M, Blomström P, Johansson R, Lhrs C, Brandt J, Olsson SB. Right atrial free wall conduction velocity and degree of anisotropy in patients with stable sinus rhythm studied during open heart surgery. Eur Heart J Feb 1998;19(2):293–300.
- [133] Boineau JP, Canavan TE, Schuessler RB, Cain ME, Corr PB, Cox JL. Demonstration of a widely distributed atrial pacemaker complex in the human heart. Circulation Jun 1988;77(6):1221–1237.
- [134] Harrild D, Henriquez C. A computer model of normal conduction in the human atria. Circ Res Sep 2000;87(7):E25–E36.
- [135] Zemlin CW, Herzog H, Ho S, Panfilov A. Computer Simulation and Experimental Assessment of Cardiac Electrophysiology. Futura Publishing, 2000; 29–34.

- [136] Vigmond EJ, Ruckdeschel R, Trayanova N. Reentry in a morphologically realistic atrial model. *J Cardiovasc Electrophysiol* Sep 2001;12(9):1046–1054.
- [137] Reumann M, Bohnert J, Osswald B, Hagl S, Doessel O. Multiple wavelets, rotors, and snakes in atrial fibrillation—a computer simulation study. *J Electrocardiol* Oct 2007;40(4):328–334. URL <http://dx.doi.org/10.1016/j.jelectrocard.2006.12.016>.
- [138] Chen YH, Xu SJ, Bendahhou S, Wang XL, Wang Y, Xu WY, Jin HW, Sun H, Su XY, Zhuang QN, Yang YQ, Li YB, Liu Y, Xu HJ, Li XF, Ma N, Mou CP, Chen Z, Barhanin J, Huang W. Kcnq1 gain-of-function mutation in familial atrial fibrillation. *Science* Jan 2003;299(5604):251–254. URL <http://dx.doi.org/10.1126/science.1077771>.
- [139] Brugada R, Hong K, Dumaine R, Cordeiro J, Gaita F, Borggrefe M, Menendez TM, Brugada J, Pollevick GD, Wolpert C, Burashnikov E, Matsuo K, Wu YS, Guerchicoff A, Bianchi F, Giustetto C, Schimpf R, Brugada P, Antzelevitch C. Sudden death associated with short-qt syndrome linked to mutations in herg. *Circulation* Jan 2004;109(1):30–35. URL <http://dx.doi.org/10.1161/01.CIR.0000109482.92774.3A>.
- [140] Hong K, Piper DR, Diaz-Valdecantos A, Brugada J, Oliva A, Burashnikov E, de Soto JS, Grueso-Montero J, Diaz-Enfante E, Brugada P, Sachse F, Sanguinetti MC, Brugada R. De novo kcnq1 mutation responsible for atrial fibrillation and short qt syndrome in utero. *Cardiovasc Res* Dec 2005; 68(3):433–440. URL <http://dx.doi.org/10.1016/j.cardiores.2005.06.023>.
- [141] Goette A, Lendeckel U, Klein HU. Signal transduction systems and atrial fibrillation. *Cardiovasc Res* May 2002;54(2):247–258.
- [142] Avitall B, Bi J, Mykytsey A, Chicos A. Atrial and ventricular fibrosis induced by atrial fibrillation: evidence to support early rhythm control. *Heart Rhythm* Jun 2008;5(6):839–845. URL <http://dx.doi.org/10.1016/j.hrthm.2008.02.042>.
- [143] van der Velden HM, van Kempen MJ, Wijffels MC, van Zijverden M, Groenewegen WA, Allessie MA, Jongsma HJ. Altered pattern of connexin40

- distribution in persistent atrial fibrillation in the goat. *J Cardiovasc Electrophysiol* Jun 1998;9(6):596–607.
- [144] Otway R, Vandenberg JI, Guo G, Varghese A, Castro ML, Liu J, Zhao J, Bursill JA, Wyse KR, Crotty H, Baddeley O, Walker B, Kuchar D, Thorburn C, Fatkin D. Stretch-sensitive *kcnq1* mutation a link between genetic and environmental factors in the pathogenesis of atrial fibrillation? *J Am Coll Cardiol* Feb 2007;49(5):578–586. URL <http://dx.doi.org/10.1016/j.jacc.2006.09.044>.
- [145] Xia M, Jin Q, Bendahhou S, He Y, Larroque MM, Chen Y, Zhou Q, Yang Y, Liu Y, Liu B, Zhu Q, Zhou Y, Lin J, Liang B, Li L, Dong X, Pan Z, Wang R, Wan H, Qiu W, Xu W, Eurlings P, Barhanin J, Chen Y. A *kir2.1* gain-of-function mutation underlies familial atrial fibrillation. *Biochem Biophys Res Commun* Jul 2005;332(4):1012–1019. URL <http://dx.doi.org/10.1016/j.bbrc.2005.05.054>.
- [146] Yang Y, Xia M, Jin Q, Bendahhou S, Shi J, Chen Y, Liang B, Lin J, Liu Y, Liu B, Zhou Q, Zhang D, Wang R, Ma N, Su X, Niu K, Pei Y, Xu W, Chen Z, Wan H, Cui J, Barhanin J, Chen Y. Identification of a *kcne2* gain-of-function mutation in patients with familial atrial fibrillation. *Am J Hum Genet* Nov 2004;75(5):899–905. URL <http://dx.doi.org/10.1086/425342>.
- [147] Restier L, Cheng L, Sanguinetti MC. Mechanisms by which atrial fibrillation-associated mutations in the s1 domain of *kcnq1* slow deactivation of iks channels. *J Physiol* Sep 2008;586(Pt 17):4179–4191. URL <http://dx.doi.org/10.1113/jphysiol.2008.157511>.
- [148] Ravens U, Cerbai E. Role of potassium currents in cardiac arrhythmias. *Europace* Oct 2008;10(10):1133–1137. URL <http://dx.doi.org/10.1093/europace/eun193>.
- [149] Yang T, Snyders DJ, Roden DM. Rapid inactivation determines the rectification and $[K^+]$ dependence of the rapid component of the delayed rectifier K^+ current in cardiac cells. *Circ Res* Jun 1997;80(6):782–789.
- [150] Olson TM, Michels VV, Ballew JD, Reyna SP, Karst ML, Herron KJ, Horton SC, Rodeheffer RJ, Anderson JL. Sodium channel mutations and

- susceptibility to heart failure and atrial fibrillation. JAMA Jan 2005; 293(4):447–454. URL <http://dx.doi.org/10.1001/jama.293.4.447>.
- [151] Zhang H, Garratt CJ, Zhu J, Holden AV. Role of up-regulation of ik_1 in action potential shortening associated with atrial fibrillation in humans. Cardiovasc Res Jun 2005;66(3):493–502. URL <http://dx.doi.org/10.1016/j.cardiores.2005.01.020>.
- [152] Bosch RF, Scherer CR, Rb N, Whrl S, Steinmeyer K, Haase H, Busch AE, Seipel L, Khalkamp V. Molecular mechanisms of early electrical remodeling: transcriptional downregulation of ion channel subunits reduces ica_1 and ito in rapid atrial pacing in rabbits. Journal of the American College of Cardiology 2003;41(5):858 – 869. ISSN 0735-1097.
- [153] Pandit SV, Berenfeld O, Anumonwo JMB, Zaritski RM, Kneller J, Nattel S, Jalife J. Ionic determinants of functional reentry in a 2-d model of human atrial cells during simulated chronic atrial fibrillation. Biophys J Jun 2005;88(6):3806–3821. URL <http://dx.doi.org/10.1529/biophysj.105.060459>.
- [154] Plonsey R. Introductory Physics And Mathematics. Pergamon Press, Oxford, 1989; 41–76.
- [155] Salu Y. Implementing a consistency criterion in numerical solution of the bioelectric forward problem. IEEE Trans Biomed Eng Jun 1980;27(6):338–341. URL <http://dx.doi.org/10.1109/TBME.1980.326742>.
- [156] Geselowitz DB. Theory And Simulation Of The Electrocardiogram. Pergamon Press, Oxford, 1989; 181–195.
- [157] Blender. <http://www.blender.org/>.
- [158] Ferguson AS, Stroink G. Factors affecting the accuracy of the boundary element method in the forward problem–i: Calculating surface potentials. IEEE Trans Biomed Eng Nov 1997;44(11):1139–1155. URL <http://dx.doi.org/10.1109/10.641342>.
- [159] Goldstein H. Classical Mechanics. 2 edition. Reading, MA: Addison-Wesley, 1980; 143–148.

- [160] van Oosterom A, Strackee J. The solid angle of a plane triangle. *IEEE Trans Biomed Eng* Feb 1983;30(2):125–126.
- [161] Anderson E, Bai Z, Bischof C, Blackford S, Demmel J, Dongarra J, Du Croz J, Greenbaum A, Hammarling S, McKenney A, Sorensen D. LAPACK Users' Guide. Third edition. Philadelphia, PA: Society for Industrial and Applied Mathematics, 1999. ISBN 0-89871-447-8 (paperback).
- [162] Crockford D. The application/json Media Type for JavaScript Object Notation (JSON). RFC 4627 (Informational), July 2006. URL <http://www.ietf.org/rfc/rfc4627.txt>.
- [163] Taccardi B. Body surface distribution of equipotential lines during atrial depolarization and ventricular repolarization. *Circ Res* Nov 1966;19(5):865–878.
- [164] Mirvis DM. Body surface distribution of electrical potential during atrial depolarization and repolarization. *Circulation* Jul 1980;62(1):167–173.
- [165] Kistler PM, Roberts-Thomson KC, Haqqani HM, Fynn SP, Singarayar S, Vohra JK, Morton JB, Sparks PB, Kalman JM. P-wave morphology in focal atrial tachycardia: development of an algorithm to predict the anatomic site of origin. *J Am Coll Cardiol* Sep 2006;48(5):1010–1017. URL <http://dx.doi.org/10.1016/j.jacc.2006.03.058>.
- [166] Ramanathan C, Rudy Y. Electrocardiographic imaging: I. effect of torso inhomogeneities on body surface electrocardiographic potentials. *J Cardiovasc Electrophysiol* Feb 2001;12(2):229–240.
- [167] Conover MB. Understanding Electrocardiography. 7 edition. Mosby-Year Book, Inc., 1996.
- [168] Hampton JR. The ECG In Practice. Churchill Livingstone, 1997.
- [169] MacFarlane PW, Lawrie TDV. The Normal Electrocardiogram and Vectorcardiogram. Pergamon Press, Oxford, 1989; 407–457.
- [170] Lian J, Li G, Cheng J, Avitall B, He B. Body surface laplacian mapping of atrial depolarization in healthy human subjects. *Med Biol Eng Comput* Nov 2002;40(6):650–659.

- [171] van Oosterom A, Jacquemet V. Genesis of the P wave: Atrial signals as generated by the equivalent double layer source model. *Europace* 2005;7(s2):S21–29. URL <http://europace.oxfordjournals.org/cgi/content/abstract/7/s2/S21>.
- [172] Huiskamp G, Oosterom AV. The depolarization sequence of the human heart surface computed from measured body surface potentials. *IEEE Trans Biomed Eng* Dec 1988;35(12):1047–1058. URL <http://dx.doi.org/10.1109/10.8689>.
- [173] Geselowitz D. On the theory of the electrocardiogram. *Proceedings of the IEEE* June 1989;77:857–876.
- [174] Geselowitz DB. Description of cardiac sources in anisotropic cardiac muscle. application of bidomain model. *J Electrocardiol* 1992;25 Suppl:65–67.
- [175] Scher AM. Validity of the uniform double layer in the solution of the ecg forward problem. *J Electrocardiol* 1994;27 Suppl:163–169.
- [176] Rankin AC, Rae AP. Sinus And Atrial Arrhythmias. Pergamon Press, Oxford, 1989; 881–913.
- [177] Kahn AM, Krummen DE, Feld GK, Narayan SM. Localizing circuits of atrial macroreentry using electrocardiographic planes of coherent atrial activation. *Heart Rhythm* Apr 2007;4(4):445–451. URL <http://dx.doi.org/10.1016/j.hrthm.2006.12.042>.
- [178] Yamane T, Shah DC, Peng JT, Jas P, Hocini M, Deisenhofer I, Choi KJ, Macle L, Clmenty J, Hassaguerre M. Morphological characteristics of p waves during selective pulmonary vein pacing. *J Am Coll Cardiol* Nov 2001;38(5):1505–1510.
- [179] Shibata N, Inada S, Mitsui K, Honjo H, Yamamoto M, Niwa R, Boyett MR, Kodama I. Pacemaker shift in the rabbit sinoatrial node in response to vagal nerve stimulation. *Exp Physiol* Mar 2001;86(2):177–184.
- [180] Dobrzynski H, Li J, Tellez J, Greener ID, Nikolski VP, Wright SE, Parson SH, Jones SA, Lancaster MK, Yamamoto M, Honjo H, Takagishi Y, Kodama I, Efimov IR, Billeter R, Boyett MR. Computer three-dimensional

- reconstruction of the sinoatrial node. *Circulation* Feb 2005;111(7):846–854. URL <http://dx.doi.org/10.1161/01.CIR.0000152100.04087.DB>.
- [181] MacFarlane PW. Lead Systems. Pergamon Press, Oxford, 1989; 315–352.
 - [182] Guillem MS, Sahakian AV, Swiryn S. Derivation of orthogonal leads from the 12-lead electrocardiogram. performance of an atrial-based transform for the derivation of p loops. *J Electrocardiol* 2008;41(1):19–25. URL <http://dx.doi.org/10.1016/j.jelectrocard.2007.07.003>.
 - [183] Platonov PG. Atrial conduction and atrial fibrillation: what can we learn from surface ecg? *Cardiol J* 2008;15(5):402–407.
 - [184] Markides V, Schilling RJ, Ho SY, Chow AWC, Davies DW, Peters NS. Characterization of left atrial activation in the intact human heart. *Circulation* Feb 2003;107(5):733–739.
 - [185] Carlson J, Havmller R, Herreros A, Platonov P, Johansson R, Olsson B. Can orthogonal lead indicators of propensity to atrial fibrillation be accurately assessed from the 12-lead ecg? *Europace* Sep 2005;7 Suppl 2:39–48. URL <http://dx.doi.org/10.1016/j.eupc.2005.04.012>.
 - [186] Holmqvist F, Platonov PG, Havmller R, Carlson J. Signal-averaged p wave analysis for delineation of interatrial conduction - further validation of the method. *BMC Cardiovasc Disord* 2007;7:29. URL <http://dx.doi.org/10.1186/1471-2261-7-29>.
 - [187] Havmoller R, Carlson J, Holmqvist F, Herreros A, Meurling CJ, Olsson B, Platonov P. Age-related changes in p wave morphology in healthy subjects. *BMC Cardiovasc Disord* 2007;7:22. URL <http://dx.doi.org/10.1186/1471-2261-7-22>.
 - [188] Yamamoto M, Dobrzynski H, Tellez J, Niwa R, Billeter R, Honjo H, Kodama I, Boyett MR. Extended atrial conduction system characterised by the expression of the hcn4 channel and connexin45. *Cardiovasc Res* Nov 2006; 72(2):271–281. URL <http://dx.doi.org/10.1016/j.cardiores.2006.07.026>.
 - [189] Ophof T. The mammalian sinoatrial node. *Cardiovasc Drugs Ther* Mar 1988;1(6):573–597.

- [190] Luo S, Wang B, Richmond P, Tompkins W. Studies of ecg to vcg transformations. In Engineering in Medicine and Biology Society, 1991. Vol.13: 1991., Proceedings of the Annual International Conference of the IEEE. Oct-3 Nov 1991; 696–697.
- [191] Hyttinen J, Viik J, Eskola H, Malmivuo J. Optimization and comparison of derived frank vecg lead systems employing an accurate thorax model. In Computers in Cardiology 1995. Sep 1995; 385–388.
- [192] van Oosterom A, Ihara Z, Jacquemet V, Hoekema R. Vectorcardiographic lead systems for the characterization of atrial fibrillation. *J Electrocardiol* Oct 2007;40(4):343.e1–343.11. URL <http://dx.doi.org/10.1016/j.jelectrocard.2006.08.002>.